University of Padua
Department of Industrial Engineering
Master Degree in

Aerospace Engineering

Master Thesis

IPT magnetic field optimization and development of electromagnetic acceleration stage

Supervisors:
Priv. Doz. Dr.-Ing. Georg Herdrich, University of Stuttgart
Dr. Daniele Pavarin, University of Padua
Francesco Romano, M.Sc., University of Stuttgart

Graduand: Riccardo Tosarello
Student number: 1178953

Academic Year 2018/2019

Contents

List of Figures viii

List of Tables ix

Nomenclature xiv

Abstract xv

Riassunto xvii

1 Introduction 1

2 Electric Propulsion 5

2.1 Main Parameters 5
2.2 EP Technologies 7
2.2.1 Electrothermal 8
2.2.2 Electrostatic 9
2.2.3 Electromagnetic 12
2.3 Inductive Plasma Thruster 15
2.4 Atmosphere-Breathing Electric Propulsion 17

3 Plasma Physics 19

3.1 Particle Motion 20
3.1.1 Magnetic Mirror 22
3.2 Plasma Waves 25
3.2.1 Plasma Oscillations 25
3.2.2 Electron Plasma Waves 26

3.2.3 Electromagnetic Waves 26
3.2.4 Electromagnetic Waves $\parallel$ to B_0 27
3.3 Theory of Helicon Waves 28

4 Radio Frequency Power Transmission 33
4.1 RF Circuit 33
4.2 Maximum Power Transfer 36
4.3 Transmission Line 39
4.4 Matching Network 41

5 Antenna 43
5.1 Coil Antenna 44
5.2 Birdcage Antenna 45
5.3 Conclusion 50

6 Acceleration Stage 53
6.1 Review 53
6.2 Electromagnetic Nozzle 58
6.2.1 Plasma Detachment 60
6.2.2 Thrust Model 61
6.2.3 Performance 64
6.3 Rotating Magnetic Field 67
6.3.1 RMF Penetration 71
6.3.2 Current Verification and Performance 72
6.4 Rotating Electric Field 74

7 Design and Simulations 79
7.1 Antenna Simulation 79
7.2 Acceleration Stage Design 84
7.2.1 Electromagnet Design 84
7.2.2 Magnetic Field Topology and Strength 88
7.3 Thermal Analysis 95
7.4 Acceleration Stage Improvement 99
7.5 Acceleration Stage Conclusions 106

8 Conclusion and Outlook **107**

List of Figures

2.1 Schematic model of a resistojet . . . 9
2.2 Schematic model of an arcjet . . . 9
2.3 Schematic model of an ion thruster . . . 10
2.4 Schematic model of an Hall effect thruster . . . 11
2.5 Schematic model of a FEEP device . . . 12
2.6 Schematic model of a MPD thruster . . . 13
2.7 Schematic model of a PPT . . . 15
2.8 Schematic model of an inductive plasma thruster . . . 16
2.9 Schematic model of an ABEP system . . . 18
2.10 Artistic representation of the GOCE mission in orbit . . . 18

3.1 Charged particles motion in a static magnetic field . . . 21
3.2 Charged particles motion in a static EM field . . . 22
3.3 Magnetic mirror scheme . . . 23
3.4 Dispersion relation of electron plasma waves . . . 27
3.5 Geometry of right-hand and left-hand circularly polarized waves 28
3.6 Right-hand and left-hand circular polarized waves dispersion relations . . . 28
3.7 Wavenumber of helicon and TG waves in a discharge chamber 31
3.8 k-β curves with different magnetic field magnitudes . . . 31

4.1 Capacitor current and voltage amplitudes with respect to time 35
4.2 Capacitor current and voltage phasors . . . 35
4.3 Impedance as frequency function . . . 36
4.4 General scheme of a RF circuit . . . 37

4.5 Scheme of a RF circuit where the generator and the load are connected through a transmission line 38
4.6 Incident and reflected power graph 39
4.7 Geometrical parameters of balanced and unbalanced transmission lines 40
4.8 Scheme of the complete RF circuit 42
4.9 L-type matching network 42

5.1 RLC circuit 44
5.2 Coil antenna in a previous IPT design at IRS 44
5.3 Birdcage antenna designs 46
5.4 Electric circuit representation of an high-pass birdcage antenna 46
5.5 Resonance spectrum of a 16-legs high-pass birdcage 47
5.6 Current distribution of an high-pass birdcage antenna 48
5.7 Time change current distribution in the legs 49
5.8 Axial view of the legs current and linear polarized magnetic field 49
5.9 Circularly polarized magnetic field in a birdcage antenna . . . 50

6.1 Theta-pinch thruster representation 55
6.2 Ponderomotive force in a magnetized plasma due to the gradient of E_z 57
6.3 Electromagnetic nozzle geometry 58
6.4 Magnetic thrust through diamagnetic and paramagnetic currents 60
6.5 Electromagnetic nozzle thrust components 64
6.6 Magnetic field topologies tested 65
6.7 Electron temperature and plasma density over the measured RF power absorbed 66
6.8 Axial profile of the normalized electron pressure 66
6.9 Results from Takahashi *et Al.* experiments 67
6.10 RMF representation 68
6.11 Radial view of RMF acceleration stage 69
6.12 Experimental data of $\frac{\gamma}{\lambda}$ versus λ for difference frequencies and radial positions 73
6.13 Motion of a particle due to REF 75

6.14 Azimuthal current in REF 76
6.15 Geometrical description of electrons trajectories in a REF . . . 77

7.1 CAD image of the birdcage antenna studied 80
7.2 Real and imaginary impedance of a shielded birdcage antenna 82
7.3 Birdcage magnetic field at a fixed time instance t_0 83
7.4 Birdcage electric field at a fixed time instance t_0 83
7.5 Preliminary IPT design image without electromagnets 85
7.6 Exploded view of the first electromagnet with its relative dimensions 87
7.7 Section view of the IPT preliminary design with acceleration stage created by two electromagnets 89
7.8 Simulation with external electromagnet in the middle position 91
7.9 Axial and radial magnetic field strength with external EM in the middle position 91
7.10 Simulation with external electromagnet in the low position . . 92
7.11 Axial and radial magnetic field strength with external EM in the low position 92
7.12 Simulation with two electromagnets with 10.5 A and 19 A . . . 93
7.13 Axial and radial magnetic field strength with internal EM and external EM in the middle position 93
7.14 Simulation with two electromagnets with 10.5 A and 19 A . . . 94
7.15 Axial and radial magnetic field strength with internal EM and external EM in the low position driven with different currents 94
7.16 Comparison between "approximated" and "real" winding cross section 96
7.17 Temperature of a test electromagnet 96
7.18 Thermal transient of the external electromagnet simulated for different values of natural convection 97
7.19 Thermal transient of the internal electromagnet simulated for different values of emissivity 97
7.20 Temperature distribution for the external electromagnet . . . 98
7.21 Temperature distribution for the internal electromagnet 98

7.22 Ohm's law main components produced by an high-pass birdcage used as RMF acceleration stage 100
7.23 Section view of the IPT with RMF acceleration stage 101
7.24 FEMM simulation with a RMF acceleration stage inside the vacuum chamber 102
7.25 Axial and radial magnetic field strength 103
7.26 Section view of the IPT with external RMF and only one electromagnet 103
7.27 Simulation with an external RMF and EM driven 19 A 104
7.28 Axial and radial magnetic field strength with an external RMF and EM driven with 19 A 104
7.29 Simulation with the external RMF and two external electromagnets driven with 19 A 105
7.30 Axial and radial magnetic field strength with the external RMF and two external EMs driven with 19 A each 105

List of Tables

2.1 Performance parameters of the main electric propulsion technologies . . . 14

3.1 Guiding center drifts . . . 24

4.1 Impedance values for ideal resistor, capacitor and inductor . . . 35

7.1 Birdcage and shield dimensions . . . 80
7.2 I/O values of the first electromagnet design . . . 87
7.3 I/O values of the second electromagnet design . . . 88

Nomenclature

Acronyms

ABEP Atmosphere-breathing electric propulsion

CCP Capacitive coupled plasma

CFD Computational Fluid Dynamics

EM Electromagnet

EN Electromagnetic nozzle

EP Electric propulsion

ESA European space agency

FEEP Field emission electric propulsion

GEO Geostationary Earth orbit

HET Hall effect thruster

IPG Inductive plasma generator

IPT Inductive plasma thruster

IRS Institut für raumfahrtsysteme

LEO Low Earth orbit

LHS Left hand side

MEO Medium Earth orbit

MHD	Magnetohydrodynamics	
MPD	Magnetoplasmadynamic	
PPT	Pulsed plasma thruster	
REF	Rotating electric field	
RF	Radio frequency	
RHS	Right hand side	
RMF	Rotating magnetic field	
RMS	Root mean square	
SEW	Single electrostatic wave	
TG	Trivelpiece-Gould	
VLEO	Very low Earth orbit	

Greek Symbols

α	Propellant utilization efficiency	-
β	Total wavenumber	rad/m
η_T	Thrust efficiency	-
λ_D	Debye length	m
μ	Magnetic momentum	$\mathrm{A \cdot m^2}$
ν	Collision frequency	1/s
ω_c	Cyclotron angular frequency	rad/s
ω_h	upper hybrid frequency	rad/s
ω_p	Plasma frequency	rad/s
$\omega_{ce(ci)}$	Electron (ion) cyclotron angular frequency	rad/s

ε_0	Permittivity of free space	$8.854\,187 \times 10^{-12}$ F/m

Roman Symbols

$\dot{m}_i$	Ion mass flow rate	kg/s
$\dot{m}_p$	Propellant mass flow rate	kg/s
$\vec{B}_{RMF}$	Magnetic field vector of RMF acceleration strategy	T
c	Speed of light	3×10^8 m/s
I_{sp}	Spacific impulse	s
$k_\perp$	Radial wavenumber	1/m
k_B	Boltzmann constant	$1.380\,649 \times 10^{-23}$ J/K
k_z	Axial wavenumber	1/m
m_0	Initial propellant mass	kg
m_f	Final propellant mass	kg
m_p	Propellant mass	kg
$m_{e(i)}$	Electron (ion) mass	kg
n_0	Plasma density	1/m^3
$n_{e(i)}$	Electrons (ions) density	1/m^3
$P_{electric}$	Power produced by the electric power supply	W
P_{thrust}	Power produced by the thrust	W
q_e	Electrical charge	$1.602\,176\,634 \times 10^{-19}$ C
r_L	Larmor radius	m
T	Thrust	N
$T_{e(i)}$	Electron (ion) temperature	eV

$v_\parallel$	Parallel velocity with respect to the magnetic field lines	m/s
$v_\perp$	Perpendicular velocity with respect to the magnetic field lines	m/s
$v_{e\theta}$	Electron radial velocity	m/s
v_{ex}	Exhaust velocity	m/s
v_E	Guiding center drift of a particle immersed in an EM field	m/s
v_{gc}	Guiding center drift	m/s
v_{th}	Termal velocity	m/s

Abstract

Within the European project DISCOVERER, the institute of space systems (IRS) of the university of Stuttgart is developing an atmosphere-breathing electric propulsion thruster for drag compensation in orbits with altitude below 400 km, called very low-Earth orbits (VLEO). The thruster should be electrode-less and able to use the residual atmosphere as propellant in order to have a potentially infinite lifetime. VLEO are attractive because their low altitude allows the increase of instrument performance and the reduction of launch cost.

In order to eliminate every contact with the plasma, the energy is transferred from the power supply to the gas through induction. A new antenna design called birdcage has been applied for the first time in a thruster. This antenna employs capacitors to create a circuit with a resonance equal to the frequency of the power supply in use that is $f = 40.68\,\mathrm{MHz}$. This characteristic is desired to match the antenna reactance to the generator one decreasing the reflected power into the circuit. This antenna creates an electromagnetic field that rotates perpendicularly with respect to the quartz tube axis and ionizes the neutral gas creating the plasma.

To accelerate the plasma it has been proposed an acceleration stage which uses two electromagnets to define the electromagnetic nozzle topology. These two devices have been designed to work separately with a power supply each that generates a maximum of 19 A at 40 V. An electromagnet is positioned around the birdcage antenna while the other is inside the vacuum chamber, right after the discharge tube. The first electromagnet task is the antenna tuning as the neutral gas is ionized and the creation of an axial magnetic field to allow the helicon way generation. Instead, the second electromagnet is focused on the magnetic field divergence outside the quartz tube. The magnetic field produced has been simulated with FEMM and thermal analyses have been conducted to verify if the electromagnets temperature exceeds the maximum one that the wire insulation can sustain.

Riassunto

Nell'ambito del progetto europeo DISCOVERER, l'istituto di sistemi spaziali (IRS) dell'università di Stoccarda sta sviluppando un propulsore del tipo "athmosphere-breathing electric propulsion" per compensare l'attrito atmosferico che è predominante in orbite con altitudine inferiore a 400 km, chiamate "very-low-Earth orbits" (VLEO). Il propulsore non deve avere elettrodi e deve usare l'atmosfera residua come propellente in modo da avere idealmente una vita infinita. Le VLEO sono interessanti perché la loro bassa altitudine permette di aumentare le prestazioni degli strumenti e di diminuire il costo di lancio del satellite.

Per eliminare ogni contatto con il plasma, l'energia è trasferita dall'alimentatore al gas attraverso una tecnologia induttiva. Per questo è stata progettata una nuova antenna, usata per la prima volta in un propulsore. Questa antenna impiega dei condensatori per creare un circuito in cui la risonanza è uguale alla frequenza dell'alimentatore, ossia 40.68 MHz. Questa caratteristica è richiesta per far equivalere la reattanza dell'antenna a quella dell'alimentatore andando dunque a diminuire la potenza riflessa all'interno del circuito. L'antenna produce così un campo elettromagnetico che ruota perpendicolarmente rispetto all'asse del tubo di quarzo e ionizza il gas neutro.

Lo stadio di accelerazione proposto utilizza due elettromagneti per definire la topologia dell'ugello elettromagnetico. Questi due dispositivi sono stati progettati per funzionare separatamente, ognuno alimentato con un alimentatore che può fornire fino a 19 A a 40 V. Un elettromagnete è posizionato in corrispondenza dell'antenna mentre l'altro è all'interno della camera a vuoto, posto subito dopo la fine del tubo di quarzo. Il compito del primo elettromagnete è sia di mantenere la sintonizzazione dell'antenna sulla frquenza dell'alimentatore mentre il plasma si forma al suo interno e sia di creare la componente assiale del campo magnetico utile per la generazione delle onde helicon. Invece, il compito del secondo elettromagnete è di far divergere le

linee del campo magnetico solo dopo la fine del tubo di quarzo. Il campo magnetico prodotto dai due elettromagneti è stato simulato con FEMM e sono state condotte delle analisi termiche per verificare se i due dispositivi superassero la temperatura massima concessa dall'isolante del filo magnetico durante il funzionamento.

Chapter 1

Introduction

The satellite orbits around Earth can be divided into three main categories:

- LEO are orbits with altitude below 2000 km;
- MEO identifies orbits in the zone between LEO and the geostationary orbit;
- GEO is an orbit with altitude 35 786 km.

LEO does not require excessive amount of propellant to be reached and the low altitude allows high bandwidth and low latency for telecommunications and an high resolution but limited field of view for Earth observations. This region is the most used so far and the amount of space debris in it is relevant: of the 10000 cataloged object only 7% are operative spacecrafts.[50] The amount of debris is constantly increasing with time and the risks of a spacecraft crash and loss is inevitably rising.

Satellites in LEO usually orbit above 500 km because otherwise aerodynamic drag from the residual atmosphere would become predominant leading to the orbit decay in some years.[66]

During the last few years, orbits below 400 km, called very low Earth orbit (VLEO), gained interest from researchers. These orbits are interesting because the low altitude has the following benefits:

- Performances: electromagnetic waves power decreases with the square of the distance. Having a spacecraft orbiting at lower altitude improves the signal to noise ratio allowing less sensitive instrument to achieve better results. In the same way, telecommunications have lower latency and optical systems improves their angular resolution determined by the Rayleigh criterion.

- Costs: the low altitude allows the same payload mass to be launched with less propellant and thus the use of smaller rockets decreases the mission cost.

- De-orbit & debris: the aerodynamic drag is a natural de-orbit system that can make a spacecraft decay in less than 3 years.[66] For this reason, there would not be a significant amount of debris left in the VLEO region leading to a lower impact risk with respect to a traditional LEO.

Having a spacecraft in VLEO requires an efficient propulsion system able to constantly compensate the drag during the entire mission period. For example, GOCE used an ion thruster to compensate the atmospheric drag at 250 km for nearly 5 years before de-orbiting. The maximum amount of propellant that can be loaded on board is a constraint for the mission lifetime and, as consequence, the thruster efficiency should be increased to use better the propellant and achieve longer missions.

With the purpose of overcoming the limiting factor of the propellant mass, the atmosphere-breathing electric propulsion concept has been developed by IRS in the past years within the European project DISCOVERER.[49] The aim is the development of an inductive plasma thruster (IPT) able to collect the residual atmosphere through an intake and use it as propellant granting the satellite to orbit for a potentially unlimited time. In the development process of an IPT based on a new birdcage antenna, this thesis is focused on design and optimization of an acceleration stage that can grant enough thrust to compensate the aerodynamic drag.

This master thesis is divided into 9 chapters; after the introduction presented in Chapter 1, Chapter 2 gives an overview of the more common electric thrusters used nowadays, with focus on IPT and atmosphere-breathing electric propulsion.

Chapter 3 is an introduction to plasma physics, from particles motion to plasma waves, with particular attention given to helicon waves.

Chapter 4 describes how the power can be transported efficiently in a RF circuit that connect the power supply to the antenna.

Chapter 5 is focused on the antenna theory for plasma generation and describes how the new antenna design, called birdcage, can improve the performance with respect to the previously used coil antenna.

Chapter 6 introduces the most used acceleration stages and deepens into electromagnetic nozzle, rotating magnetic field and rotating electric field.

Chapter 7 explains the preliminary design of the birdcage antenna through XFdtd and the final design of the electromagnetic nozzle acceleration stage created with two electromagnets. The magnetic field produced is simulated with FEMM and the electromagnets thermal analysis is conduced with SolidWorks. Then, it is presented an improvement of the electromagnetic nozzle performance through a rotating magnetic field acceleration stage.

Finally, Chapter 8 presents the conclusions of this master thesis and some ideas for further works on this topic.

Chapter 2

Electric Propulsion

Electric propulsion (EP) concept dates back to the first years of the 20$^{\text{th}}$ century but it took until the 1960s for the first successful sub-orbital demonstration of an ion engine (SERT I) by the United States. Electric propulsion is a branch of the more wide field of spacecraft propulsion which includes chemical propulsion (solid, liquid and hybrid), nuclear propulsion, tether propulsion, solar sail propulsion and many more concepts that have not been validated yet.

Electric propulsion uses an electric power supply to ionize a neutral gas through the use of electrodes or antennae. EP systems have very low thrust (20–50 mN/kW), long burning time and an highly efficient utilization of the propellant. However, with respect to other propulsion technologies, the power supply mass must be taken into account and it becomes a limiting factor for the applicability of electric propulsion systems.

2.1 Main Parameters

It is useful to introduce some of the most important parameters utilized to compare spacecraft propulsion technologies.

The thrust is a dynamic reaction generated as consequence of particles or fluid flow acceleration outside the thruster. Thus, the thrust (T) is the time rate of change of the exit flow momentum described by Equation (2.1) where $\dot{m}_p$ is the propellant mass flow rate and v_{ex} is the exhaust velocity of the propellant, assumed constant.

$$T = \frac{d(m_p v_{ex})}{dt} = \dot{m}_p v_{ex} \tag{2.1}$$

The thrust is expressed in N, the mass flow rate in kg/s and the exhaust velocity in m/s. However, in laboratory experiments the mass flow rate is usually expressed as sccm (standard cubic centimeters per minute). Chemical rockets reach values of MN while electric propulsion systems achieve not more than a few N.

Tsiolkovsky equation, shown in (2.2), gives an expression for the velocity change Δv where m_p is the propellant mass, m_0 is the initial mass and m_f is the final mass.

$$\Delta v = v_{ex} \ln\left(\frac{m_0}{m_f}\right) = v_{ex} \ln\left(1 + \frac{m_p}{m_f}\right) \tag{2.2}$$

An high velocity increment can be achieved burning more propellant mass ($m_p \approx m_0$) or rising the exhaust velocity. Chemical propulsion can reach no more than $v_{ex} = 5500\,\mathrm{m/s}$ because the energy, stored into the propellant, imposes a limit on the maximum exhaust velocity reachable.[41] Instead, in the EP the propellant is energized from an external source producing an higher exhaust velocity and thus higher Δv without changing the ratio m_p/m_0. Typical Δv values required are: 2–6 m/s per year for attitude control, 30 m/s per year for drag compensation at 500 km, 9.7 km/s in an Earth-LEO transfer and 10–15 km/s to reach the far-off planets.[41]

The specific impulse (I_{sp}) is the ratio between the thrust produced and the rate of fuel consumption. In order to have a value that can be easily compared with the one of different thrusters, the specific impulse is divided by the Earth's surface gravitational acceleration to have the I_{sp} expressed in seconds. If the thrust is considered constant, the specific impulse is proportional only to the exhaust velocity.

$$I_{sp} = \frac{T}{\dot{m}_p g_0} = \frac{v_{ex}}{g_0} \tag{2.3}$$

The specific impulse is an indicator of the engine efficiency. For example, if the I_{sp} is high, the system is able to produce more thrust with the same amount of propellant. Solid state rockets have specific impulse around 250 s, liquid rockets around 320 s while electric propulsion systems are in the range of 150–10 000 s.

The thrust efficiency (η_T) is the ratio between the power produced by the thrust and the electrical power generated by the power supply. It indicates how well the electric power is converted into thrust.

$$\eta_T = \frac{P_{thrust}}{P_{electric}} = \frac{\dot{m}_p v_{ex}^2}{2P_{electric}} = \frac{T^2}{2\dot{m}_p P_{electric}} \tag{2.4}$$

The thrust-to-power ratio is obtained from Equation (2.4) and it is

$$\frac{T}{P_{electric}} = \frac{2\eta_T}{\alpha v_{ex}} = \frac{2\eta_T}{I_{sp} g_0} \tag{2.5}$$

where the thrust is defined as $T = \alpha \dot{m}_i v_{ex}$ with $\dot{m}_i$ the ion mass flow rate and $\alpha = \dot{m}_i/\dot{m}_p$ the propellant utilization efficiency. Equation (2.5) shows that, for a fixed thrust efficiency and input power, an increase in the I_{sp} reduces the thrust. Since EP systems have an high specific impulse, the thrust is low and these devices need to operate over a long period of time to imprint a substantial acceleration to the spacecraft.

Finally, the thruster lifetime is a limiting factor since the majority of electric propulsion systems use electrodes in direct contact with hot gas or plasma. This interaction erodes electrodes and degrades the thruster performance over time. The development efforts to design an efficient electrode-less thruster aim to eliminate this limiting factor.

2.2 EP Technologies

Electric propulsion systems can be divided into three main categories based on how the gas is accelerated.[31] These categories are the following:

- Electrothermal: a discharge is used to heat the propellant which is then expanded through a nozzle.

- Electrostatic: the charged particles are accelerated through the application of electrostatic forces.

- Electromagnetic: the charged particles, interacting with the electromagnetic fields, create currents in the plasma and a body force equal to $\vec{j} \times \vec{B}$ is achieved.

The performance of the most important electric propulsion devices are compared in Table 2.1.

2.2.1 Electrothermal

Electrothermal devices use different techniques to heat up the gas and then expand it through a nozzle where the thermal energy is converted into directed kinetic energy to produce the thrust.[31] The electrothermal propulsion systems are divided into two subcategories: resistojets and arcjets.

Resistojets

The resistojets are the simplest electric propulsion devices. The heating system is based on the Joule effect. It can be composed by coils that heat the propellant, as shown in Figure 2.1, tungsten spheres with current flowing through their contact zones or resistive heated discharge chamber walls. This technology is the only one that does not require the ionization of the gas and it is able to reach an efficiency of more than 50%. The advantages are the easy integration in the satellite system, the use of low operational voltage, the reliability, the low cost and safety. Unfortunately, the specific impulse is low ($I_{sp} = 300\,\mathrm{s}$) because it is limited by the maximum temperature reachable by discharge camber and nozzle that is around $3000\,\mathrm{K}$.[41]

Arcjets

The arcjet, which scheme is shown in Figure 2.2, is composed by a cathode in the center of the thruster and an anode that serves even as nozzle. Applying a voltage between the electrodes, it is possible to create an high-current arc ($\approx 100\,\mathrm{A}$) between the cathode tip and the anode. The propellant is ionized by this discharge and the temperature at the plasma core reaches 1–2 eV. The presence of a strong temperature gradient leads to a plasma temperature

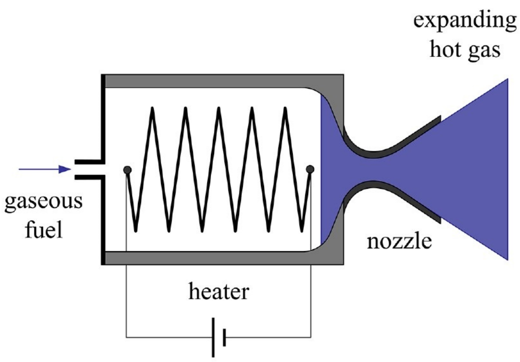

Figure 2.1: Schematic model of a resistojet. [41]

of 2000 K near the wall preventing them to melt. The higher temperature reached with respect to resistojets allows arcjets to achieve specific impulse around 500 s with ammonia or hydrazine as propellant.[41] However, surfaces exposed to plasma wear out easily and therefore this technology has a limited lifetime.

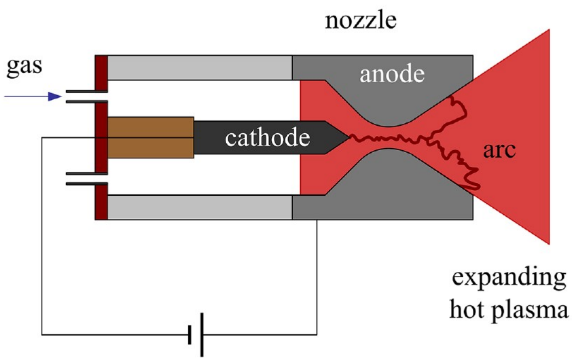

Figure 2.2: Schematic model of an arcjet. [41]

2.2.2 Electrostatic

Electrostatic devices aim to overcome the thermal limitations of electrothermal one with the use of electric body force to accelerate the ionized gas. Within electrostatic systems there are: ion thrusters, Hall effect thrusters and field emission electric propulsion thrusters.

Ion Thrusters

An ion thruster, which scheme is shown in Figure 2.3, can be divided into two zones: ionization and acceleration. In the first, the gas is ionized through the use of different techniques such as dc discharges or radio frequencies while the latter is generally composed by two grids which have the task to accelerate ions. The grid in contact with the plasma, called screen grid, is set to an high potential to screen the electrons. The second, called acceleration grid, has a low potential to accelerate ions. Outside the grids, the ion beam is neutralized through the addition of electrons from a cathode. The electron density is typically $10^{17}\,\mathrm{m}^{-3}$ and electron temperature is 2–5 eV. Ion thrusters have efficiency above 70% and a specific impulse of 3000 s.[41] This high value of I_{sp} means that the thrust produced is low as described by Equation (2.5). This technology is mature and largely applied. For its low propellant consumption it is even used in mission where a large Δv is needed without the requirement to supply it in a short amount of time. However, the erosion of the grid due to ion impacts is still an important limiting factor of this thruster.

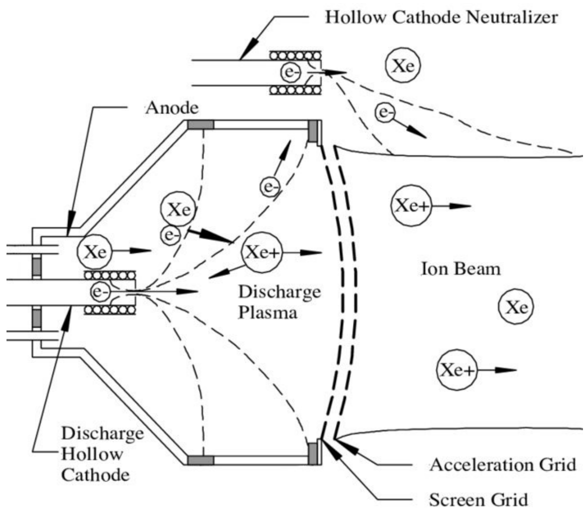

Figure 2.3: Schematic model of an ion thruster. [16]

Hall Effect Thrusters

An Hall effect thruster (HET) has a ring-shaped discharge chamber which section is shown in Figure 2.4. In this chamber there is a radial magnetic field created by electromagnets or permanent magnets. The anode and the propellant supply are on the back part of the discharge chamber while the cathode is external. Then, there is an axial electric field when a voltage is applied between the two electrodes. The cathode emits electrons that are attracted by the anode. When they reach the electromagnetic field in the discharge chamber, they slow their motion toward the anode and start to drift in the $\vec{E} \times \vec{B}$ direction creating and azimuthal current also known as Hall current. The propellant is ionized as soon as it gets in contact with this current. The ions are not affected by the magnetic field because it is not strong enough to magnetize them. Instead, the electric field accelerates the ions and an axial thrust is generated. In a xenon HET electron density reaches value of $5 \times 10^{17}\,\mathrm{m}^{-3}$ with $T_e = 10$–$15\,\mathrm{eV}$, specific impulse lower than 2000 s and thrust-to-power ratio of 60 mN/kW.[41] Hall effect thrusters are typically used in orbit raising and station keeping maneuvers.

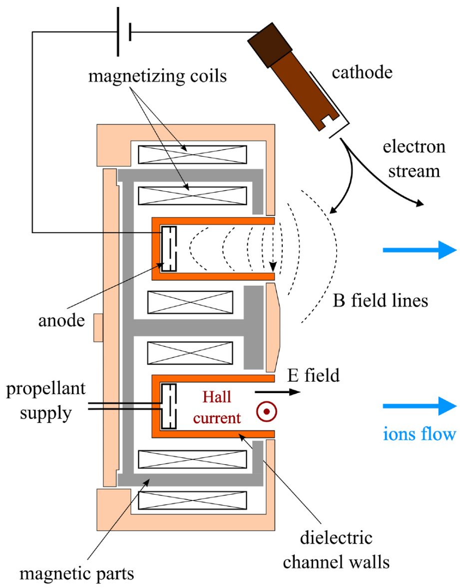

Figure 2.4: Schematic model of an Hall effect thruster. [41]

Field Emission Electric Propulsion Thrusters

A field emission electric propulsion (FEEP) thruster uses liquid propellant like Cesium. The liquid is moved into a channel of 1 µm diameter through capillarity effect. At the end of the channel there is a strong electric field that rips off electrons from the liquid and accelerates ions. The ion beam is then neutralized with a cathode. A scheme of this technology is shown in Figure 2.5. The thrust produced is very low (in the order of µN), the specific impulse is about 8000 s and the efficiency can reach 98%.

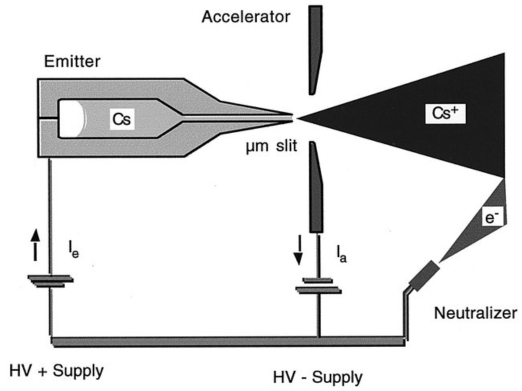

Figure 2.5: Schematic model of a FEEP device. [32]

2.2.3 Electromagnetic

Electromagnetic propulsion systems work through the interaction between currents induced in the ionized gas and the magnetic field externally applied or produced by the same currents. In this class of electric propulsion systems there are magnetoplasmadynamic thrusters and pulsed plasma thrusters.

Magnetoplasmadynamic Thrusters

A magnetoplasmadynamic (MPD) thruster is composed by two concentric electrodes between which an high-ampere current flows. The neutral gas is ionized through impacts with electrons. The current between the electrodes creates a magnetic field $\vec{B}$ that, with the radial current density $\vec{j}$, gives a

Lorentz force to ions described by $\vec{F_L} = \vec{j} \times \vec{B}$. This type of MPD thruster, shown in Figure 2.6, is called self-field because it utilizes the magnetic field produced by the current density. Instead, the applied-field MPD thruster uses coils or permanent magnets around the discharge chamber in order to create a magnetic field that has an axial and a radial component. As the previous type, the axial component of the Lorentz force accelerates the ions. The specific impulse is the range of 1000–10 000 s, the efficiency can reach 40% and the thrust is between 0.5 and 50 N.[41]

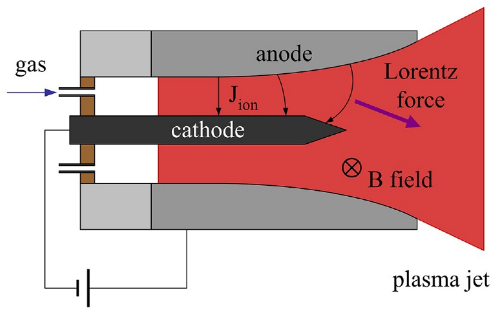

Figure 2.6: Schematic model of a MPD thruster. [41]

Pulsed Plasma Thrusters

A pulsed plasma thruster (PPT), shown in Figure 2.7, is composed by a solid propellant pushed by a spring into an electric arc. This arc is created between two electrodes using capacitors that can store an high amount of energy and release it in a fraction of a second. The discharge time is usually about 10 µs and it can carry a power of 10 MW.[32] The electric arc ablates and ionizes the propellant. The presence of the plasma allows a current density to flow, a magnetic field is created by this current and the plasma is accelerated through the Lorentz force $\vec{j} \times \vec{B}$. The I_{sp} range is 500–1500 s and the thrust is below 0.01 N. This device is simple, compact and its throttling capability makes it useful for station-keeping and attitude control.[41]

Table 2.1: Performance parameters of the main electric propulsion technologies. [41], [59]

Thruster type	I_{sp} (s)	Thrust (N)	Power (kW)	Efficiency	Fuel
Electrothermal					
Resistojet	100–300	0.2	0.1–1	80%	N_2, hydrazine, ammonia
Arcjet	500	0.1–2	1–100	35%	hydrazine, ammonia
Electrostatic					
Ion thruster	3000	10^{-3}–0.1	0.1–5	60–80 %	Xe
HET	1500	10^{-2}–1	0.2–20	50%	Xe
FEEP	8000	10^{-4}	0.01–0.15	up to 98%	Cesium
Electromagnetic					
MPD thruster	1000–10 000	0.5–50	100–10^3	25%	Ar, H_2, Li
PPT	500–1500	10^{-5}–10^{-2}	0.01	5%	PFTE

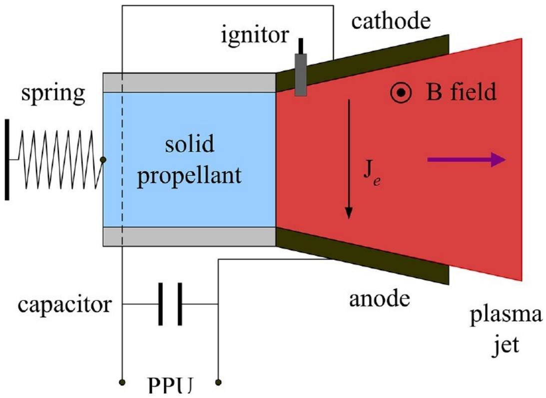

Figure 2.7: Schematic model of a PPT. [41]

2.3 Inductive Plasma Thruster

EP technologies introduced before, except for resistojets, employ electrodes to ionize the gas. Cathode and anode are in direct contact with the plasma and the discharge produced between them increases their wear velocity, especially at high power level. Over the past two decades electrod-less electric propulsion thrusters have been developed under the name of inductive plasma thruster (IPT). These devices are composed by:

- gas feeder that diffuses the neutral particle into the discharge chamber;
- antenna (or coil) driven with RF voltage that ionizes the gas;
- electromagnets or permanent magnets which task is to create an axial magnetic field in the discharge tube (also known as quartz tube) to promote the wave propagation into the plasma, to reduce the plasma transport in the direction perpendicular to the magnetic field and to create a divergent magnetic field outside the discharge chamber acting like an electromagnetic nozzle.

Sometimes the quartz tube has even a solid divergent nozzle to use the expansion of the remain neutral particles to enhance the thrust.

An inductive plasma thruster scheme is shown in Figure 2.8. The device can be divided into two parts: the inductive plasma generator (IPG) where the gas is ionized by the electric field produced by antenna and acceleration stage where the magnetic field lines diverge. A quasi-neutral plasma is expelled out of the thruster and therefore a neutralizer is not required.

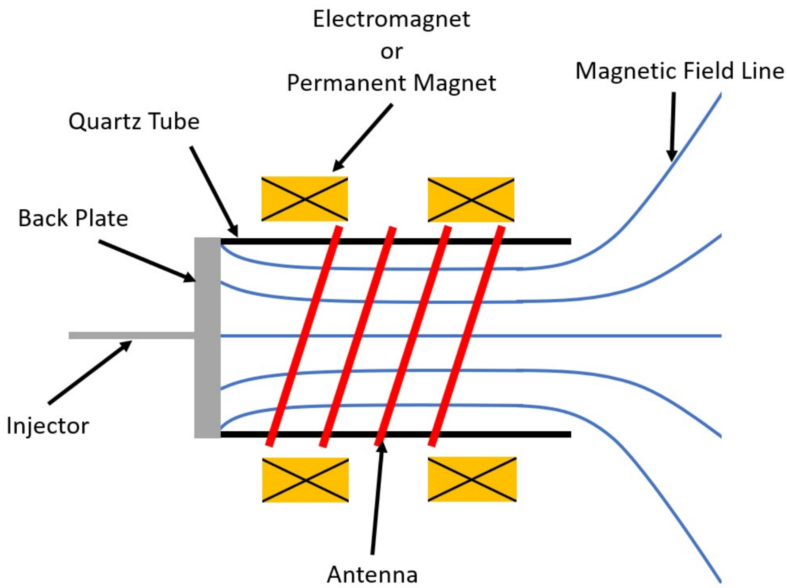

Figure 2.8: Schematic model of an inductive plasma thruster.

IPTs can be divided into three categories depending on the type of coupling that the antenna EM field has with the neutral gas electrons. The capacitive coupled plasma (CCP), that works in electrostatic mode (E-mode), can be obtained with two parallel electrodes driven with a RF voltage. The plasma density that can be reached is usually 10^{15}–$10^{16}\,\mathrm{m}^{-3}$. The inductive coupled plasma (ICP), which works in electromagnetic mode (H-mode), is achieved with the flow of a RF current into a coil that surrounds the discharge channel. The coil produces an alternating EM field into the plasma that transfer energy to electrons. The density that can be reached is in the range of 10^{16}–$10^{18}\,\mathrm{m}^{-3}$. However, an ICP device starts in E-mode to develop a low-density plasma and the H-mode takes over only when the plasma conductivity reaches a value sufficient for the electromagnetic mechanism to prevail. The third class of energy coupling is called wave mode (W-mode). This mode exists only when there is a static magnetic field in the discharge chamber that sustains a low-frequency wave which electric field rotates during its propagation along the z-direction.[9] The rotation of this wave carries electrons in a helical motion and for this reason a thruster that works in W-mode is expected to use helicon waves as coupling mechanism. For this reason, it is usually called helicon thruster.

While a plasma produced by E-mode and H-mode stores the energy in RF sheaths and skin depth respectively, the W-mode produces a wave that can penetrate deeper into the plasma transferring the energy from the discharge tube boundaries to the plasma core further enhancing the ionization.[9]

In the presence of a static magnetic field, the H-mode can eventually lead to the W-mode through an increase of the antenna power when the plasma is dense enough to support helicon wave propagation.[9]

2.4 Atmosphere-Breathing Electric Propulsion

The Earth atmosphere has not well defined boundaries but a gradual transition into space as the density decreases with the rising of the altitude. Furthermore, as solar activity intensify, the particle density at a fixed altitude increases caused by the atmosphere thermal expansion. The atmospheric density at 600 km is in the range of 10^{-12}–10^{-14} kg/m^3 depending on solar activity magnitude while at 300 km it is 10^{-10}–10^{-11} kg/m^3.[17] For orbits around 200 km the drag is so strong that satellites without propulsion system last for a few days before decay.[52] The ones with a propulsion systems need high Δv to compensate drag and the propellant mass becomes the majority of the satellite mass in order to reach the lifetime target.

An atmosphere-breathing electric propulsion (ABEP) system, shown in Figure 2.9, employs an intake to collect the residual atmosphere and uses it as propellant for an IPT in order to create the necessary thrust to compensate the atmospheric drag. The advantages of this technology are first, the lack of on-board propellant which allow lighter and cheaper satellites or higher payload masses and second, the spacecraft lifetime increase.

In VLEO altitude the presence of the atomic oxygen is relevant. The atomic oxygen is an heavy and corrosive particle that is one of the main reasons for surface degradation in LEO orbits.[51] For this reason an ABEP requires to develop stronger and more durable structures to achieve the expected lifetime.

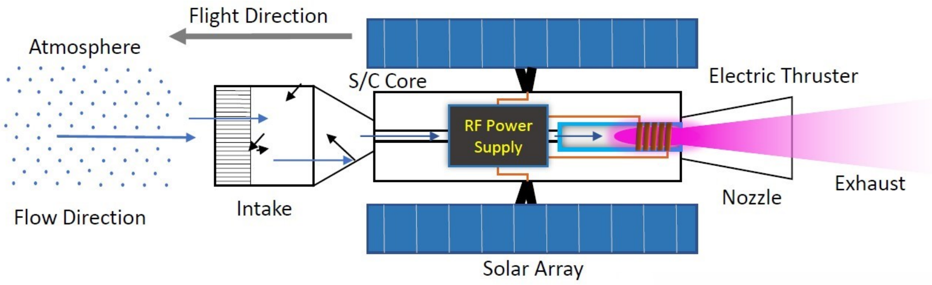

Figure 2.9: Schematic model of an ABEP system. [49]

The GOCE mission[58] of the European space agency (ESA), shown in Figure 2.10, would have been suitable for an ABEP application due to its low altitude. The GOCE task was the measurement of the Earth gravitational field with an accuracy of 10^{-6} g allowing the knowledge of the Earth geoid within 2 cm. To reach these accuracy levels, the mission had an altitude of $\approx$250 km and used ion thrusters for drag compensation. This mission, initially designed to last twenty months, lasted more than four years since the Sun activity was lower than expected.

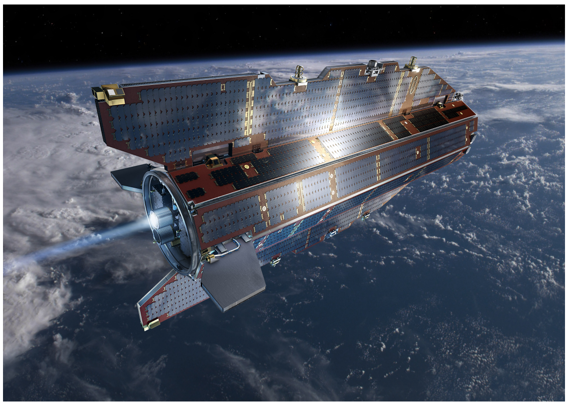

Figure 2.10: Artistic representation of the GOCE mission in orbit. Credits: ESA /AOES Medialab

Chapter 3

Plasma Physics

"A plasma is a quasi-neutral gas of charged and neutral particles which exhibits collective behavior".[11] The plasma charged particles motion creates currents and magnetic fields. This movement can generate charge concentrations and so electric fields. This electromagnetic field inside the plasma interacts with the charged particles in a long scale with respect to the particle dimension. This is the so called plasma collective behavior.

If there are two electrodes immersed in a plasma, when they are connected to a battery, electrons drift toward the anode while ions, heavier than electrons, do not move. In this way electrons leave back a positive charge and they create a negative one near the anode. This charge imbalance gives rise to an electrostatic field opposite to the one applied by the electrodes and with about the same magnitude. Therefore, the plasma has shielded out the external electric field. The charge concentration around the electrodes has a characteristic dimension called Debye length λ_D (or sheath) which is calculated through Equation (3.1).

$$\lambda_D = \sqrt{\frac{\varepsilon_0 k_B T_e}{n_e q_e^2}} \tag{3.1}$$

The Debye length is the dimension in which charge imbalances can exist; outside λ_D externally applied electric fields are shielded out. If the dimension L of the system is much larger than λ_D, external electric fields or electric fields produced by a charge imbalance are shield out in a dimension shorter than

L. In this case the plasma can be defined as quasi-neutral meaning that there are not so strong electric potential that can create high charge imbalance. In this case, electron and ion density are about the same, so $n_e \approx n_i \approx n_0$, where n_0 is called plasma density.

3.1 Particle Motion

Plasma can have a wide range of densities. When the density is high the collision behavior is dominant and the plasma can be treated as a fluid. Instead, if the density is low, collisions are unimportant and it is necessary to study the single particle motion.[11]

The electromagnetic field applied on a charged particle creates a Lorentz force as in Equation (3.2).

$$m\frac{d\vec{v}}{dt} = q(\vec{E} + \vec{v} \times \vec{B}) \tag{3.2}$$

If a particle is immersed in a magnetic field pointing in the z-direction ($\vec{E} = 0$ and $\vec{B} = B\hat{z}$), the Lorentz force components are the following.

$$\begin{cases} \dot{v}_x = \left(\frac{qB_z}{m}\right) v_y \\ \dot{v}_y = -\left(\frac{qB_z}{m}\right) v_x \\ \dot{v}_z = 0 \end{cases} \tag{3.3}$$

Taking the derivate with respect to time of these equations and substituting the values of $\dot{v}_x$ and $\dot{v}_y$ from Equation (3.3), the following differential equations are obtained.

$$\begin{cases} \ddot{v}_x = -\left(\frac{qB_z}{m}\right)^2 v_x \\ \ddot{v}_y = -\left(\frac{qB_z}{m}\right)^2 v_y \\ \ddot{v}_z = 0 \end{cases} \tag{3.4}$$

These equations indicate that the motion of a particle in a magnetic field is a circumference around the magnetic field lines with cyclotron angular frequency, ω_{cj}, shown in Equation (3.5), where j indicates the species, electrons or ions.

$$\omega_{cj} = \frac{|q|B}{m_j} \tag{3.5}$$

The radius of this motion around the field lines is called Larmor radius, r_L, and it can be found with $v_\perp = \omega_c r_L$ where $v_\perp$ is the particle velocity component perpendicular to the magnetic field.

$$r_{Lj} = \frac{v_\perp}{\omega_{cj}} = \frac{m_j v_\perp}{|q|B} \tag{3.6}$$

As shown in Figure 3.1, a charged particle in a magnetic field has a circular orbit around the guiding center (x_{Gc}, y_{Gc}) called Larmor gyration. Electron circular motion is smaller than ion one but it has higher frequency due to the lower electron mass. Moreover, the direction of rotation is opposite since the electron charge is the contrary of ion one.

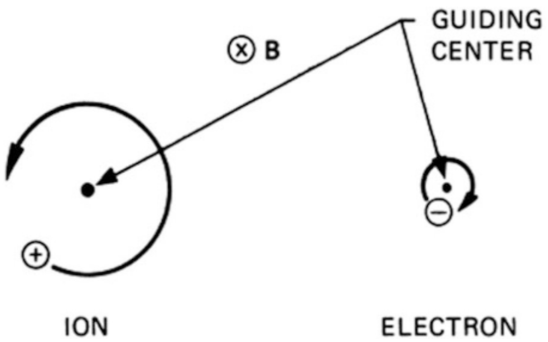

Figure 3.1: Charged particle motion in a static magnetic field. [11]

If $\vec{E} \neq 0$, the trajectory is sum of the previous Larmor gyration and a drift of the guiding center as shown in Figure 3.2. This phenomenon can be explained starting, for example, from a stationary ion. When the electric field is applied, the particle gains velocity along the field lines. This velocity, being perpendicular to the magnetic field, creates a Lorentz force that bends the trajectory with radius r_L. When the particle reaches the bottom part of the circumference, its motion is against the electric field, the velocity decreases until the particle stops and the process restarts. So, the particle motion creates a spiral and the guiding center drift, v_{gc}, is described by Equation (3.7) where the drift velocity has been indicated with v_E meaning that the electric field is accountable for this drift.

$$v_E = \frac{\vec{E} \times \vec{B}}{B^2} \tag{3.7}$$

This equation shows that the drift is always perpendicular to both electric and magnetic field. The main guiding center drifts are summarized in Table 3.1.

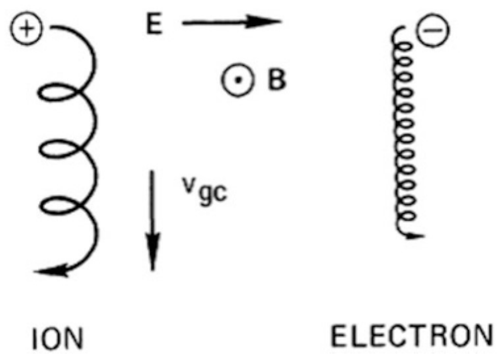

Figure 3.2: Charged particles motion in a static EM field. [11]

3.1.1 Magnetic Mirror

A magnetic mirror is a specific arrangement of the magnetic field lines in which there is a transition from more to less dense field lines or opposite. An example is shown in Figure 3.3. The magnetic mirror has not a magnetic field component in the azimuthal direction, so $\vec{B} = (B_r, 0, B_z)$. The Lorentz force can be simplified as follow.

$$\begin{cases} F_r = q(\underbrace{v_\theta B_z}_{1} - v_z \cancelto{0}{B_\theta}) \\ F_\theta = q(-\underbrace{v_r B_z}_{2} + \underbrace{v_z B_r}_{3}) \\ F_z = q(v_r \cancelto{0}{B_\theta} - \underbrace{v_\theta B_r}_{4}) \end{cases} \tag{3.8}$$

Terms 1 and 2 give rise to a Larmor gyration when the particle has a velocity perpendicular to the magnetic field lines. This motion is indicated by the solid line in Figure 3.3. Term 3 gives an azimuthal drift of the guiding center and it vanishes on the axis since $B_r|_{r=0} = 0$. Term 4 can be written using $\vec{\nabla} \cdot \vec{B} = 0$

in Equation (3.9).

$$\frac{1}{r}\frac{\partial(rB_r)}{\partial r}+\frac{1}{r}\cancelto{0}{\frac{\partial B_\theta}{\partial\theta}}+\frac{\partial B_z}{\partial z}=0 \tag{3.9}$$

If B_z is not function of r, then:

$$B_r=-\frac{1}{2}r\frac{\partial B_z}{\partial z} \tag{3.10}$$

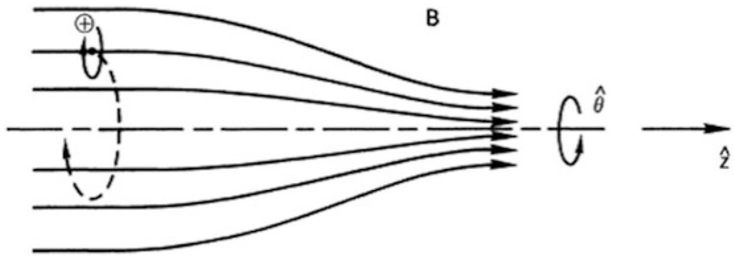

Figure 3.3: Magnetic mirror scheme. [11]

Substituting Equation (3.10) into the third row of (3.8), the axial force becomes:

$$F_z=\frac{1}{2}qv_\theta r\frac{\partial B_z}{\partial z} \tag{3.11}$$

Considering a particle which guiding center lies on the axis, the drift of the guiding center is null and the particle has only a gyration motion. In this case, the azimuthal velocity is equal to $v_\perp$ and $r=r_L$. So, the average force over one gyration has only a z-component that is:

$$\bar{F_z}=\mp\frac{1}{2}qv_\perp r_L\frac{\partial B_z}{\partial z}=\mp\frac{1}{2}q\frac{v_\perp^2}{\omega_c}\frac{\partial B_z}{\partial z}=-\mu\frac{\partial B_z}{\partial z} \tag{3.12}$$

where μ is the magnetic momentum described by

$$\mu=\frac{1}{2}\frac{mv_\perp^2}{B}=const. \tag{3.13}$$

Chen[11] shows that μ is constant over time. If the particle moves in a zone where the magnetic field is stronger, then its $v_\perp$ increases to maintain μ constant. Since the total energy is constant, if the perpendicular velocity increases then the parallel velocity decreases. Therefore, going near a zone of stronger magnetic field, the particle velocity is transformed from parallel to perpendicular. This mechanism is the base of the electromagnetic nozzle operation.

Table 3.1: Guiding center drifts.[11]

Drift Name	Drift Equation	Notes
General force F	$v_f = \frac{1}{q}\frac{\vec{F}\times\vec{B}}{B^2}$	-
Electric field	$v_E = \frac{\vec{E}\times\vec{B}}{B^2}$	-
Gravitational field	$v_g = \frac{m}{q}\frac{\vec{g}\times\vec{B}}{B^2}$	-
Non-uniform E field	$v_E = \left(1 + \frac{1}{4}r_L^2\nabla^2\right)\frac{\vec{E}\times\vec{B}}{B^2}$	-
Gradient B field	$v_{\nabla B} = \pm\frac{1}{2}v_\perp r_L \frac{\vec{B}\times\nabla\vec{B}}{B^2}$	-
Curvature drift	$v_R = \frac{mv_\parallel^2}{q}\frac{\vec{R}_c\times\vec{B}}{R_c^2B^2}$	B-field with curvature $\vec{R}_c$ but constant intensity with the radius
Curved vacuum field	$v_c = \frac{m}{q}\left(v_\parallel^2 + \frac{1}{2}v_\perp^2\right)\frac{\vec{R}_c\times\vec{B}}{R_c^2B^2}$	Magnetic field intensity decreasing with the radius
Polarization drift	$v_p = \pm\frac{1}{\omega_c B}\frac{d\vec{E}}{dt}$	-

3.2 Plasma Waves

Every wave, propagating along x, must satisfy the following differential equation

$$\frac{\partial^2 u}{\partial x^2} = \frac{1}{v^2}\frac{\partial^2 u}{\partial t^2} \tag{3.14}$$

where u is the wave propagation velocity. A solution of Equation (3.14) has to be dependent on time and position and it can be written as $u(x,t) = e^{i\omega t} f(x)$. Substituting this solution into Equation (3.14), the following relation is obtained.

$$\frac{\partial^2 f(x)}{\partial x^2} = -\left(\frac{\omega}{v}\right)^2 f(x) \tag{3.15}$$

The solution of Equation (3.15) is $f(x) = Ae^{\pm ikx}$ where $k = \omega/v$ is the wavenumber. Therefore, the wave function in its general form is

$$u(x,t) = Ae^{\vec{k}\cdot\vec{r}-\omega t} \tag{3.16}$$

Two velocities can be distinguished in a wave. The phase velocity is the velocity of a point of constant phase in the wave while the group velocity is the velocity of the envelope of a modulated wave.[11]

$$v_\varphi = \frac{\omega}{k} \qquad \text{(Phase velocity)}$$

$$v_g = \frac{d\omega}{dk} \qquad \text{(Group velocity)}$$

The phase velocity can exceed the speed of light, c, without violating the theory of relativity since the information is carried by the envelope of the modulated wave which travels with the group velocity that never exceed c.

3.2.1 Plasma Oscillations

Considering now an uniform plasma in equilibrium without an externally applied electromagnetic field. If electrons are displaced from their stable position, a charge concentration arises as well as an electric field that tends to restore the quasi-neutrality. This field pulls back electrons to their original position but they overshoot thanks to their inertia and the precess restarts. This movement creates an electrons oscillation so fast that ions are not able to move due to their high inertia. The plasma frequency, ω_p, is described by Equation (3.17).

$$\omega_p = \sqrt{\frac{n_0 q_e^2}{\varepsilon_0 m}} \tag{3.17}$$

If $n_0 = 10^{18}\,\mathrm{m}^{-3}$, the plasma electron frequency is $f_p = 9\,\mathrm{GHz}$.[11]

Equation (3.17) does not depend on k so the group velocity $d\omega/dk$ is zero and the wave does not propagate. For this reason, it has been named oscillation instead of wave.

3.2.2 Electron Plasma Waves

If the thermal motion of electron is taken into account, the plasma oscillation becomes a wave that propagates through the plasma. The dispersion relation, $\omega(k)$, is then:

$$\omega^2 = \omega_p^2 + \frac{3}{2}k^2 v_{th}^2 \tag{3.18}$$

where $v_{th}^2 = 2k_B T_e/m$. Here the angular frequency depends on the wavenumber and the wave propagates with the following group velocity.

$$v_g = \frac{d\omega}{dt} = \frac{3v_{th}^2}{2v_\varphi} \tag{3.19}$$

The plot of the dispersion relation in Equation (3.18) is shown in Figure 3.4. If the thermal velocity increases, the parabola gets closer to the vertical axis. The point P represents a wave which has an angular frequency ω_p plus a contribution due to the thermal velocity. When k is large (λ small) the information moves with a group velocity close to the thermal one. Below ω_p there is no wave propagation.

3.2.3 Electromagnetic Waves

If a wave has both electric and magnetic field, it is called electromagnetic. The only possibility for an EM wave is to have $\vec{k}$ perpendicular to the EM field. For this reason the wave is called transverse. Light and radio waves correspond to this description. The dispersion relation is:

$$\omega^2 = \omega_p^2 + c^2 k^2 \tag{3.20}$$

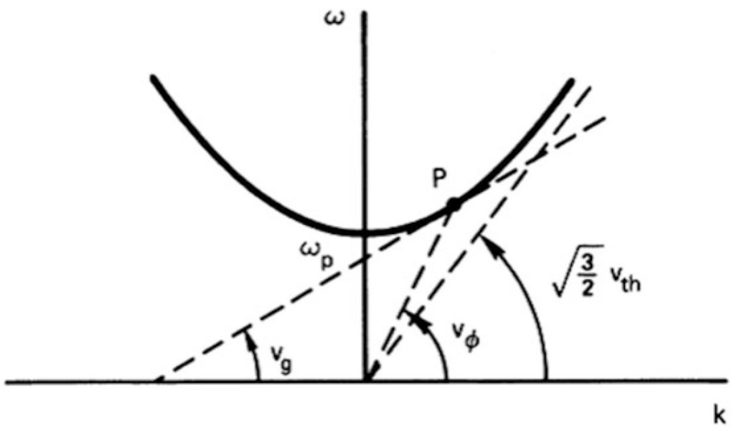

Figure 3.4: Dispersion relation of electron plasma waves. [11]

When a wave of frequency ω is sent to the plasma, the wavenumber gets the value prescribed by equation (3.20). If the plasma density increases, ω_p rises and k^2 lowers. If n_0 reaches a certain threshold, k^2 becomes negative and k imaginary. In this case, the wave cannot propagate into the plasma and it is reflected back. This phenomenon is called cutoff.

3.2.4 Electromagnetic Waves $\parallel$ to B_0

More types of waves can be produced with the addition of an external magnetic field, B_0. If the wavenumber of an electromagnetic wave is along the static magnetic field B_0 and its magnitude is able to magnetize only electrons ($\omega_{ci} = 0$), the dispersion relations of the EM waves are

$$\frac{c^2k^2}{\omega^2} = 1 - \frac{\omega_p^2/\omega^2}{1-(\omega_c/\omega)} \qquad \text{(R wave)}$$

$$\frac{c^2k^2}{\omega^2} = 1 - \frac{\omega_p^2/\omega^2}{1+(\omega_c/\omega)} \qquad \text{(L wave)}$$

These two waves are right-hand (R) and left-hand (L) circularly polarized. Figure 3.5 shows the geometry of these two waves.

The dispersion relations are plotted in Figure 3.6. There are two cutoffs frequencies, ω_R and ω_L, where $k = 0$ and the wave is reflected. The L wave cannot propagate if $\omega < \omega_L$ because k becomes imaginary. Instead, the R

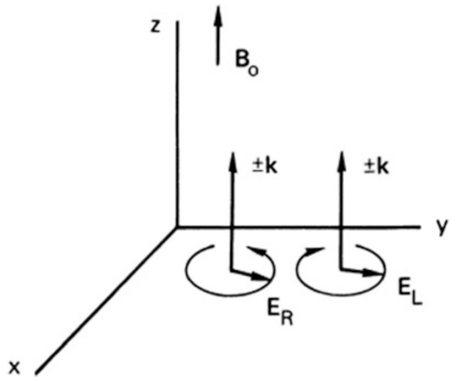

Figure 3.5: Geometry of right-hand and left-hand circularly polarized waves. [11]

wave has a band of propagation in the range $0 < \omega < \omega_c$. A wave in this frequency range is called whistler wave or helicon wave.

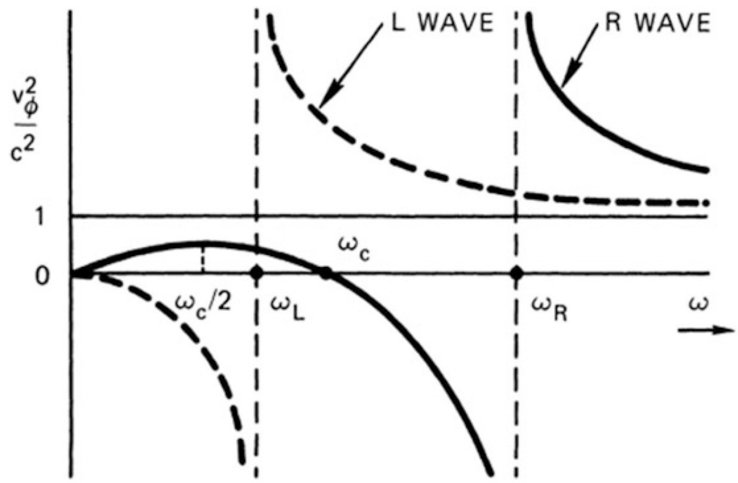

Figure 3.6: R and L waves dispersion relations. On the y-axis there is the inverse of the reflective index. [11]

3.3 Theory of Helicon Waves

The theory described in this section has been derived by Chen and Arnush in [13]. Equilibrium quantity are indicated by the subscript 0 while perturbation quantities are without it. The perturbation is assumed to be proportional to $e^{i(m\theta+k_z z-\omega t)}$ where m is the azimuthal mode, k_z is the z-component of the total wavenumber k and ω is the wave angular frequency. The external magnetic field is assumed along z: $\vec{B}_0 = B_0\hat{z}$. Maxwell's equations are:

$$\nabla \cdot \vec{B} = 0 \tag{3.21}$$

$$\nabla \times \vec{E} = -i\omega\vec{B} \tag{3.22}$$

$$\nabla \times \vec{B} = \mu_0\vec{j} \tag{3.23}$$

The displacement current in Equation (3.23) is neglected because, during experiments, electrons are usually dense enough that the current carried by the electron motion is predominant.[5]

The electron equation of motion is described by:

$$-i\omega m_e\vec{v} = -e\left(\vec{E} + \vec{v} \times \vec{B}_0\right) - m_e\nu\vec{v} \tag{3.24}$$

with ν a generic collision frequency. Since the helicon wave is a low-frequency whistle wave in the range $\omega_{ci} \ll \omega \ll \omega_{ce}$, the ion motion can be neglected and the current density, shown in Equation (3.25), is given by the motion of only electrons.

$$\vec{j} = -en_0\vec{v} \tag{3.25}$$

Equation (3.24) can be written as:

$$\vec{E} = -\frac{B_0}{en_0}\left(i\delta\vec{j} + \hat{z} \times \vec{j}\right) \tag{3.26}$$

with $\omega_c = eB_0/m_e$ and $\delta = (\omega + i\nu)/\omega_c$. Substituting Equation (3.26) into the Maxwell's equations, the relation (3.27) is obtained where $\omega_p = ne^2/\epsilon_0 m_e$ and $k_w = \omega n_0\mu_0 e/B_0$.

$$\delta\nabla \times \nabla \times \vec{B} - k_z\nabla \times \vec{B} + k_w^2\vec{B} = 0 \tag{3.27}$$

Equation (3.27) can be seen as:

$$(\delta\beta^2 - k_z\beta + k_w^2)\vec{B} = 0 \tag{3.28}$$

which can be factorized as:

$$(\beta_1 - \beta)(\beta_2 - \beta)\vec{B} = 0 \tag{3.29}$$

with $\beta = \nabla\times$.

In the case of $m_e \to 0$, the solution of Equation (3.28) is only one and the helicon dispersion relation is obtained as follow:

$$\beta = \frac{k_w^2}{k_z} = \frac{\omega n_0 e \mu_0}{k_z B_0} \tag{3.30}$$

Instead, if $\delta k_w^2 \ll k_z^2$, there are two solutions that are:

$$\begin{aligned}\beta_{1,2} =& \frac{k_z}{2\delta}\left[1 \mp \left(1 - \frac{4\delta k_w^2}{k_z^2}\right)^{\frac{1}{2}}\right] \approx \frac{k_z}{2\delta}\left[1 \mp \left(1 - \frac{2\delta k_w^2}{k_z^2}\right)\right] = \\ =& \begin{cases} \frac{k_z}{2\delta}\frac{2\delta k_w^2}{k_z^2} \\ \frac{k_z}{2\delta}\left(2 - \frac{2\delta k_w^2}{k_z^2}\right) \end{cases} \approx \begin{cases} k_w^2/k_z \\ k_z/\delta \end{cases}\end{aligned} \tag{3.31}$$

The first solution is the helicon wave dispersion relation previously obtained in Equation (3.30). The second is called Trivelpiece-Gould (TG) wave which is a damped wave due to the imaginary part inside δ. The solutions of Equation (3.29), $\beta_{1,2}$, can be written as:

$$\nabla \times \vec{B}_1 = \beta_1 \vec{B}_1, \qquad \nabla \times \vec{B}_2 = \beta_2 \vec{B}_2 \tag{3.32}$$

Taking the curl of Equation (3.32) and remembering that $\nabla \cdot \vec{B} = 0$, the two vector Helmholtz equations in (3.33) are obtained. From the definition of the Helmholtz equation, $\beta_{1,2}$ represents the total wavenumber of helicon and TG waves.

$$\nabla^2 \vec{B}_1 + \beta_1^2 \vec{B}_1 = 0, \qquad \nabla^2 \vec{B}_2 + \beta_2^2 \vec{B}_2 = 0 \tag{3.33}$$

In Figure 3.7 is shown a scheme of the axial and radial wavenumber of helicon and TG wave in a discharge camber of radius r_0.

Equation (3.28) can also be written as:

$$k_z = \frac{\delta}{\beta}\left(\beta^2 + \frac{k_w^2}{\delta}\right) \tag{3.34}$$

which diagram is displayed in Figure 3.8. This graph shows that for each k_z there are two β, the one on the left is an helicon wave while the one of the right is a TG wave. For this reason, since $\beta^2 = k_z^2 + k_\perp^2$, TG waves have a radial wavenumber (wavelength) larger (shorter) than helicon waves.

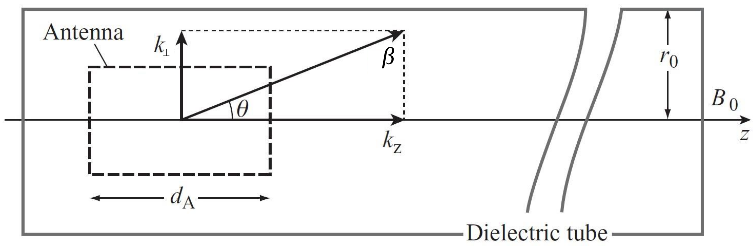

Figure 3.7: Wavenumber of helicon and TG waves in a discharge chamber. Adapted from [9].

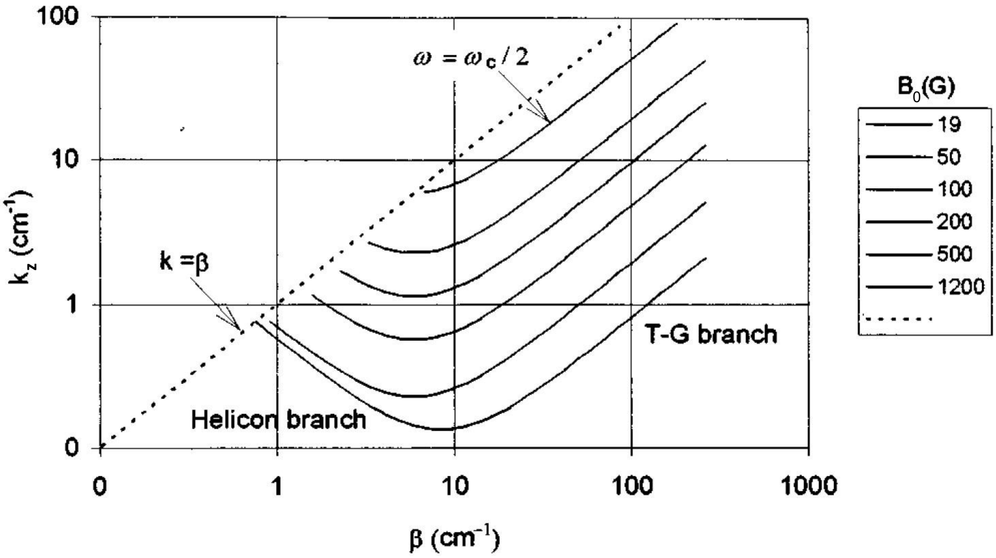

Figure 3.8: k-β curves with different magnetic field strength, organized in the legend as they appear in the diagram. The plasma density is $n_0 = 2 \times 10^{13}\,\mathrm{cm}^{-3}$, $\omega = 27.12\,\mathrm{MHz}$, m=1 and the tube radius is 2.5 cm. [13]

Generally, helicon wave moves more axially while TG waves travels mostly along the radial direction. Furthermore, for low level of external magnetic field, the only wave that propagates into the plasma is the TG wave.

Since TG waves are damped and they start from the discharge chamber walls, they are not usually able to reach the core of the plasma and therefore they stay localized near the boundary. Chen reports in Reference [10] that the power from the antenna is often absorbed by the TG waves rather than the helicon waves.

Chapter 4

Radio Frequency Power Transmission

An antenna, driven with radio frequency voltage, is used to ignite a plasma discharge inside the quartz tube.

The power transmission system should be able to transfer efficiently the energy from the generator to the antenna with the lower amount of power loss possible. Therefore, the antenna can be driven with more power allowing an higher plasma density to be reached.[9]

This chapter deals with the design of transmission lines and the impedance matching concept.

4.1 RF Circuit

An electrical circuit is a path in which an electric current flows. It can be composed by different parts but the most commons are generators, resistors, capacitors and inductors. A radio frequency circuit is an electrical circuit where the generator is driven with an alternating current or voltage.

In a RF circuit the input current and voltage change sinusoidally over time and they can be described by the following equations:

$$\begin{aligned} v(t) &= V_M sin(\omega t + \alpha) \\ i(t) &= I_M sin(\omega t + \beta) \end{aligned} \tag{4.1}$$

where ω is the angular frequency, t is the time, α and β are the phases while V_M and I_M are the amplitude of the two waves. Using phasor theory, these two equations can be written as shown in Equation (4.2) where dots indicate the phasor form.

$$\begin{aligned} \dot{V} &= V_M e^{j\alpha} e^{j\omega t} \\ \dot{I} &= I_M e^{j\beta} e^{j\omega t} \end{aligned} \tag{4.2}$$

The impedance Z is a complex number that represents the obstruction to the flow of an alternating current. Its phasor and complex forms are expressed in Equation (4.3) where R is the resistance and X the reactance, both measured in Ω.

$$\begin{aligned} \dot{Z} &= \frac{\dot{V}}{\dot{I}} \\ Z &= R + jX \end{aligned} \tag{4.3}$$

Analyzing the behavior of a capacitor, the alternating current flowing in it can be found substituting Equation (4.1) in the capacitor current-voltage relation shown in Equation (4.4).

$$\begin{gathered} i(t) = C\frac{dv(t)}{dt} = \omega C V_M cos(\omega t + \alpha) = \omega C V_M sin(\omega t + \alpha + \frac{\pi}{2}) \\ \omega C V_M = I_M \end{gathered} \tag{4.4}$$

Using phasor algebra, Equation (4.4) can be written as:

$$\dot{I} = \omega C \dot{V} e^{j\frac{\pi}{2}} e^{j\alpha} e^{j\omega t} = j\omega C \dot{V} e^{j\alpha} e^{j\omega t} \tag{4.5}$$

Inserting Equation (4.5) into the definition of $\dot{Z}$, it follows that:

$$\dot{Z} = \frac{\dot{V}}{\dot{I}} = -\frac{j}{\omega C} = jX_C \tag{4.6}$$

with X_C the capacitive reactance. The part $e^{j\alpha}e^{j\omega t}$ has not been considered because it only indicates that the phasor has an initial phase of α and it rotates with the angular frequency ω.[18]

Diagrams of Equations 4.4 and 4.5 can be seen in Figure 4.1 and 4.2, respectively. In a capacitor the current flows earlier than the voltage because, being the voltage proportional to the charges on the plates, the current must flow in advance to create charge separation in the plates and rise the voltage. The opposite behavior can be found for inductors where the voltage rises before the current.

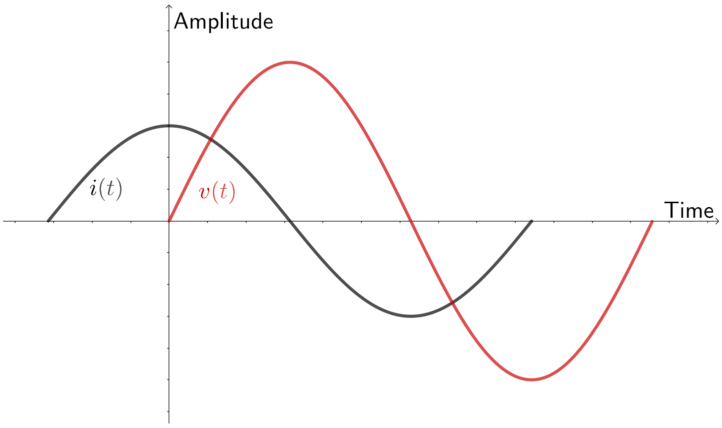

Figure 4.1: Capacitor current and voltage amplitudes with respect to time.

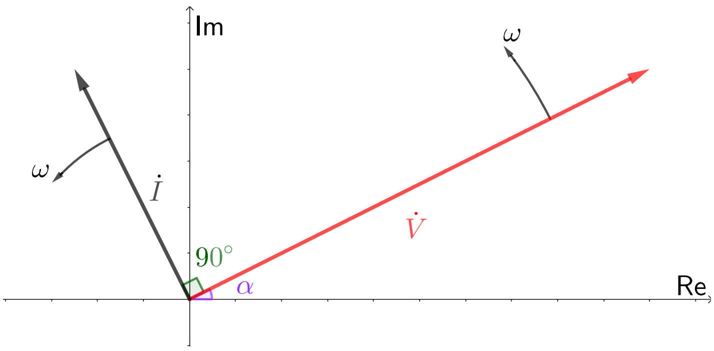

Figure 4.2: Capacitor current and voltage phasors.

Table 4.1: Impedance values for ideal resistor, capacitor and inductor.

Dipole Type	Resistance	Reactance	Impedance
Resistor (R)	R	0	$Z_R = R$
Capacitor (C)	0	$X_C = -\frac{1}{\omega C}$	$Z_C = -j\frac{1}{\omega C}$
Inductor (L)	0	$X_L = \omega L$	$Z_L = j\omega L$

The impedance values of ideal resistors, capacitors and inductors in a RF circuit are summarized in Table 4.1. In an ideal dipole, the impedance is purely real for resistors, while it is imaginary for capacitors and inductors. Moreover, since the angular frequency can be written as $2\pi f$ with f the input wave frequency, capacitors and inductors have different behaviors when driven with high or low frequency waves. For example, an ideal inductor has an opposition to the current flow that linearly decreases as the frequency reduces. If frequency reaches zero and so the dipole is driven with direct current, the current flows freely in it. On the other way, the capacitor has a completely opposite behavior while the frequency have no influence on a resistor as shown in Figure 4.3.[18]

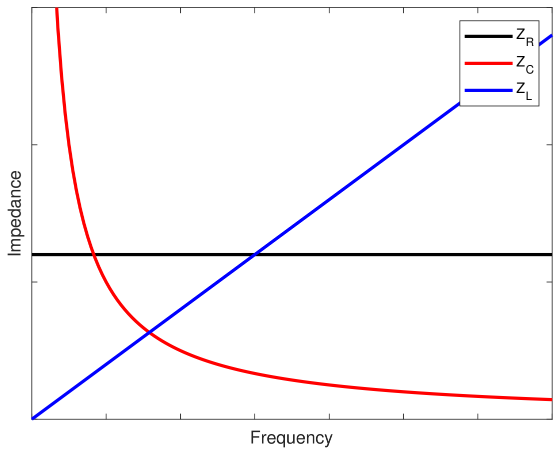

Figure 4.3: Impedance as frequency function.

4.2 Maximum Power Transfer

A schematic representation of a RF circuit is given in Figure 4.4. On the left there is a real RF generator composed by an ideal voltage input, V_{RF}, and an impedance $Z_{gen} = R_{gen} + jX_{gen}$. On the other side, there is the load impedance, $Z_{load} = R_{load} + jX_{load}$, that represents everything outside the generator like transmission lines, matching network, antenna and plasma.

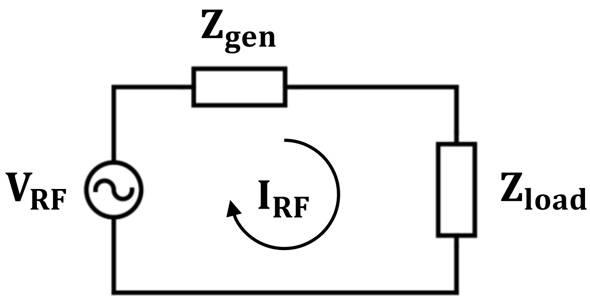

Figure 4.4: General scheme of a RF circuit.

It is required to transfer the maximum power possible from the generator to the load in order to have a stronger antenna electromagnetic field which can achieve an higher density plasma. The power absorbed by the load, P_L, is a function of resistances and reactances of the circuit as shown in Equation (4.7).

$$P_L = R_{load}|\dot{I}_{RF}|^2 = V_{RF}^2 \frac{R_{load}}{(R_{gen} + R_{load})^2 + (X_{gen} + X_{load})^2} \tag{4.7}$$

The maximum power transfer is obtained when $Z_{gen} = \bar{Z}_{load}$ where $\bar{Z}$ is the complex conjugate of Z. This condition is called impedance matching.[8] Thus, the maximum power transfer is obtained when:

$$\begin{cases} R_{load} = R_{gen} \\ X_{load} = -X_{gen} \end{cases} \tag{4.8}$$

The RF generator at IRS facility has a purely real impedance of $50\,\Omega$ which is a common value for industrial applications. The load must show to the RF generator an impedance of $(50 + j0)\Omega$ in order to have impedance matching and achieve the maximum power transfer. If conditions in Equation (4.8) are not met, a mismatching is created into the circuit between the RF generator and the load. In this case, a fraction of the power produced by the RF generator, called input power (IP), reaches the load while the rest is reflected back into the transmission line as reflected power (RP).

This concept can also be applied to multiple circuits connected together. For example, a RF circuit can be composed by RF generator and load connected together by a transmission line with a characteristic impedance Z_0 as shown in Figure 4.5. If $Z_{gen} = \bar{Z}_0$ and $Z_0 = \bar{Z}_{load}$, all the power produced is delivered to the load and there are not mismatches in the circuit. Instead, if $Z_0 \neq \bar{Z}_{load}$, a fraction of the produced power, transported by the transmission line, is not able to reach the load due to the mismatch between Z_0 and Z_{load} and it is reflected back into the transmission line.

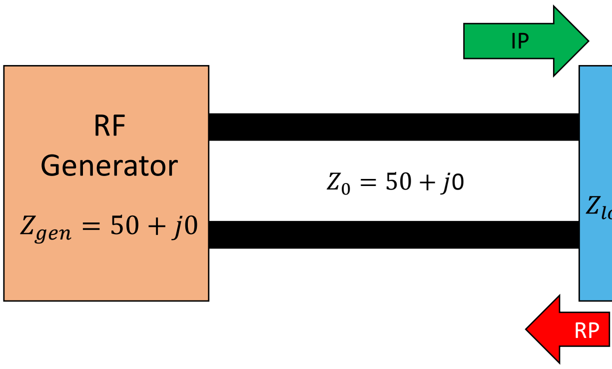

Figure 4.5: Schematic representation of a RF circuit where a transmission line (classically indicated with two parallel cables) connects the RF generator to the load. Between the transmission line and the load there is an impedance mismatch and therefore a fraction on the incident power (IP) is reflected back and it is called reflected power (RP).

Incident and reflected power can also be seen in the definition of instantaneous power:

$$\begin{aligned} p(t) =& v(t)i(t) = V_M sin(\omega t) I_M sin(\omega t - \varphi) \\ =& \frac{V_M I_M}{2} \left[cos\varphi + sin\left(2\omega t - \varphi - \frac{\pi}{2}\right)\right] \end{aligned} \tag{4.9}$$

where φ is the phase angle between current and voltage. The instantaneous power is sum of a constant and an oscillating term. Taking the mean over one period, the incident power, P_{inc}, is obtained and it coincides with the constant part of the previous equation:

$$P_{inc} = \frac{V_M I_M}{2} cos\varphi = VIcos\varphi \tag{4.10}$$

where the RMS values of current and voltage have been used instead of their maximum values. Equation (4.9) is plotted in Figure 4.6.

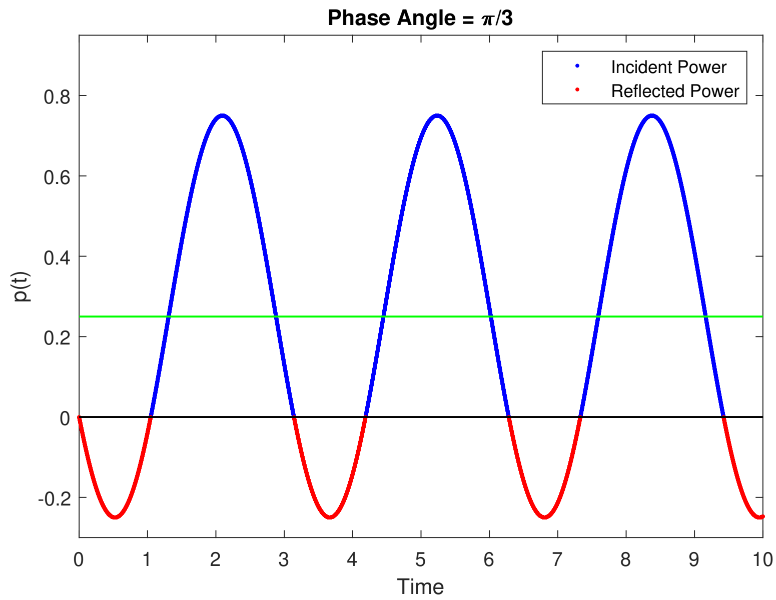

Figure 4.6: Incident and reflected power graph for $\varphi = \frac{\pi}{3}$. The green line is the value of Equation (4.10).

The power is reflected when $p(t)$ becomes negative. If the phase angle φ is zero, the current is in phase with the voltage and the reactances are zero or at least balanced. Then, the instantaneous power never gets negative and the incident power is maximum. Otherwise, if there is a net reactance in the circuit, the current is not in phase with the voltage anymore, $p(t)$ becomes negative for a certain amount of the period and then some of the power is reflected. In conclusion, there is reflected power into the circuit when the sum of its reactances is different from zero and it is higher as the phase angle approaches 180°.

4.3 Transmission Line

A cable in a RF circuit is called "transmission line" when it is longer than 10% of the input wavelength. When this characteristic length is reached, the cable impedance must be taken into account because the voltage has significant variations over the cable length.[36]

The RF generator of the IRS facility produces a wave with frequency

40.68 MHz and therefore every cable longer than 0.74 m should be considered as a transmission line.

As shown in Figure 4.7, there are two types of transmission lines:

- Balanced transmission lines composed by two separate conductors in which equal and opposite currents flow.
- Unbalanced transmission lines (coaxial cable) in which there is a central powered conductor inside an hallow one used as current return path.

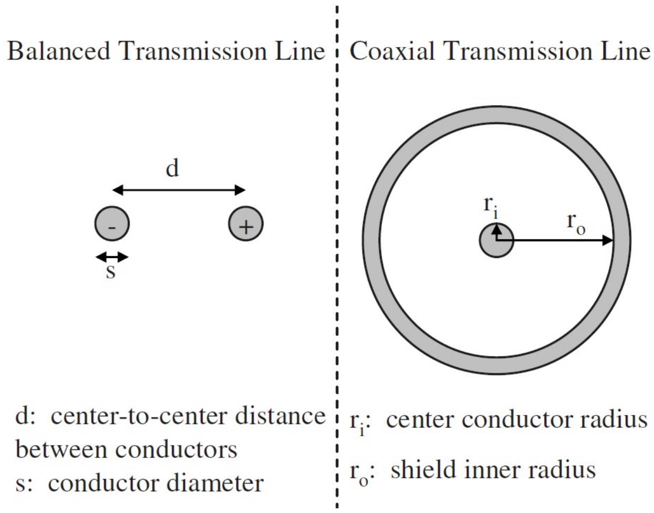

Figure 4.7: Geometrical parameters of balanced and unbalanced transmission line. [36]

The characteristic impedances of these two types of lines are:

$$\begin{aligned} Z_0|_{balanc.} &= \frac{\sqrt{\mu/\varepsilon}}{\pi} cosh^{-1}\left(\frac{s}{d}\right) \\ Z_0|_{unbalanc.} &= \frac{\sqrt{\mu/\varepsilon}}{\pi} ln\left(\frac{r_0}{r_i}\right) \end{aligned} \tag{4.11}$$

where μ and ε are the cable dielectric permeability and permittivity, respectively. The major problem with balanced lines is that, if the distance between cables changes along their length, the transmission line impedance varies changing the amount of reflected power. There is no such problem with a coaxial cable because the outer conductor radius can not change along the cable length due to the presence of the dielectric material. Moreover, in a coaxial cable the external conductor acts as a shield for the internal powered cable preventing electric and magnetic field to propagate outside. This effect allows a lower power dissipation and increases the power transmission efficiency.

Considering a transmission line of length l connected to a load with impedance Z_L, the impedance seen at the transmission line input is:

$$Z_{in} = Z_0 \frac{Z_L + jZ_0 tan\left(\frac{2\pi l}{\lambda}\right)}{Z_0 + jZ_L tan\left(\frac{2\pi l}{\lambda}\right)} \tag{4.12}$$

If the line length is one-half of the wavelength then, whatever is the value of characteristic impedance of the cable, the input impedance is always equal to the one of the load. Therefore, it is possible to consider a transmission line as a simple cable without impedance by choosing the right value for its length.[36]

4.4 Matching Network

The matching network (MN) is a device positioned between the RF generator and the load. Its task is to hide the load impedance and show at its input terminals an impedance equal to the generator one.

A scheme of the complete RF circuit can be seen in Figure 4.8. The different parts are connected together trough cable without impedance because they have been chosen to be long as half wavelength. The load part is representative of the antenna and plasma which has a complex impedance that is constantly changing with time.[65]

Without a matching network, the reflected power produced by the load would reach the RF generator that is not design to dissipate it. In order to protect this device, a matching network that dissipates the reflected power coming from the load has been added. Moreover, the matching network shows constantly a purely real impedance of $50\,\Omega$ that matches the generator one in a way to not create reflected power between MN and RF generator.[65]

At the IRS facility a L-type matching network (Figure 4.9) is used. It consists on two variable capacitors that can be adjusted through mechanical

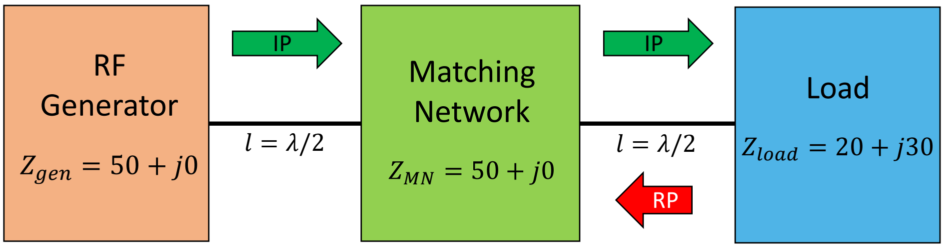

Figure 4.8: Complete scheme of the power transfer system at the IRS facility. The connections are considered as simple cables without characteristic impedance because their length is half wavelength. The only power reflected is produced between load and matching network.

motion of one of their plates. This device is able first, to dissipate the reflected power coming from the load diverting it to an internal resistance and second, to show a purely real impedance of 50 Ω to the generator.

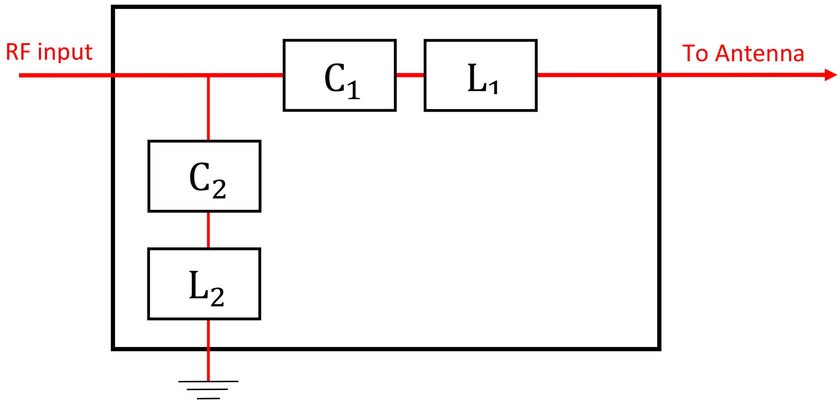

Figure 4.9: L-type matching network.

Chapter 5

Antenna

The antenna is a device used to deposit energy mostly into electrons. When a neutral gas is fed into the discharge tube, the antenna energies free electrons in it. These electrons, colliding with neutral particles, ionize the propellant creating plasma.

An antenna for plasma creation can be seen as a RLC circuit. A conductive wire exhibits a resistance, R, depending on its composition. If this wire is folded to create a loop and a current flows in it, a magnetic field is created and it acts like an inductor with inductance L. Adding a capacitor with capacitance C, a circuit RLC is created as shown in Figure 5.1. This circuit, driven with an RF generator, has an impedance described by Equation (5.1).

$$Z = \sqrt{R^2 + (X_L - X_C)^2} \tag{5.1}$$

This impedance is minimum and purely real when the RF generator wave has a frequency, f, equal to the circuit resonance frequency, f_r, which value is shown in Equation (5.2).

$$f_r = \frac{1}{2\pi\sqrt{LC}} \tag{5.2}$$

In this case, the circuit is said in resonance and its reactance value is zero. This phenomenon can be used to design an antenna that exhibits a purely real impedance which does not reflect power back into the circuit.

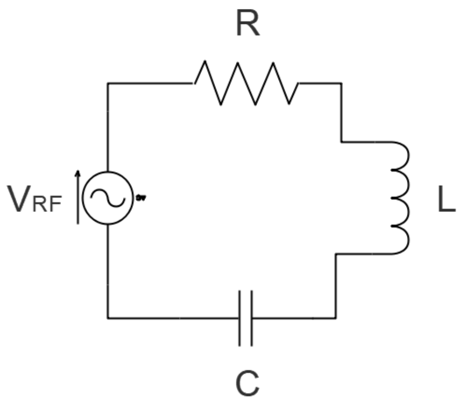

Figure 5.1: RLC circuit.

5.1 Coil Antenna

The previous IPT design at the IRS used a coil antenna as plasma generation device. This antenna is composed by a copper wire twisted as shown in Figure 5.2. The current flowing in it produces an axial magnetic field which variations induce an azimuthal electric field. This field energies electrons which ionize the neutral gas.[48]

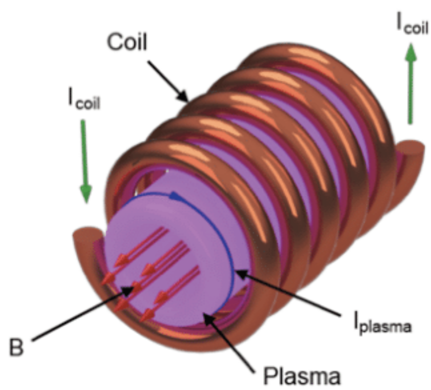

Figure 5.2: Coil antenna in a previous IPT design at IRS. [48]

The antenna has an inductance described by Equation (5.3) where N is the number of turns, Φ the flux inside a single coil, I the current flowing in the device and l the antenna length.

$$L = \frac{N\Phi}{I} = \mu_0 \frac{N^2 A}{l} \tag{5.3}$$

When this antenna is working, a capacitance is created in the circuit even if there is not a physical capacitor in it. Therefore, the antenna exhibits one or more resonance frequencies.[37] However, since the antenna capacitance cannot be chosen as desired, it is difficult to work in the antenna resonance especially if the RF generation frequency is fixed. As result, this antenna design creates reflected power that cannot be controlled unless it is used a RF generator with variable frequency.

5.2 Birdcage Antenna

The birdcage antenna is widely use in Magnetic Resonance Imagining (MRI) as excitation and detection device thanks to its ability to create an homogeneous and circularly polarized magnetic field inside the antenna volume.[38]

The antenna is composed by two end-rings connected together through N legs (or rungs) equally spaced as shown in Figure 5.3. The antenna structure gives the resistance and the inductance of the circuit while the capacitance is given by capacitors that can be placed on legs or end-rings. If the capacitors are positioned in the end-rings, the antenna is named high-pass, if they are positioned in the legs, the antenna is low-pass.[3] Therefore, the birdcage antenna can be seen as a sequence of RLC circuits. For this reason, the antenna exhibits more than one resonance frequencies in which its reactance is zero. Ideally, if the antenna is driven in resonance, the creation of reflected power into the circuit can be avoided. This is a desired characteristic because in this way more power can be deposited into electrons creating a denser plasma.[53]

An high-pass birdcage antenna can be schematically represented as in Figure 5.4 where L and M are the inductances of end-rigs and legs, respectively. Applying Kirchhoff's voltage law in this circuit driven with a RF current, it can be found that the resonant frequencies of a N-legs high-pass birdcage

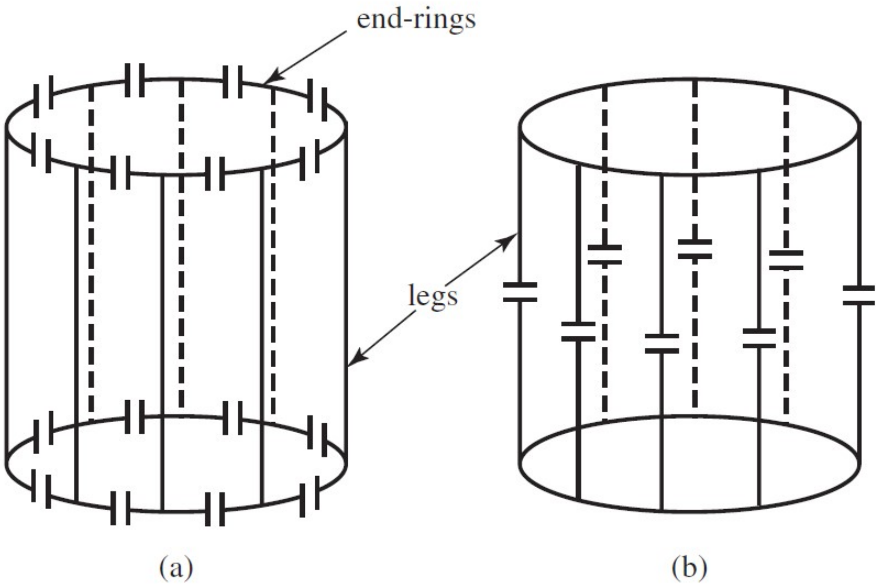

Figure 5.3: Two types of birdcage antenna: (a) high-pass and (b) low-pass. [3]

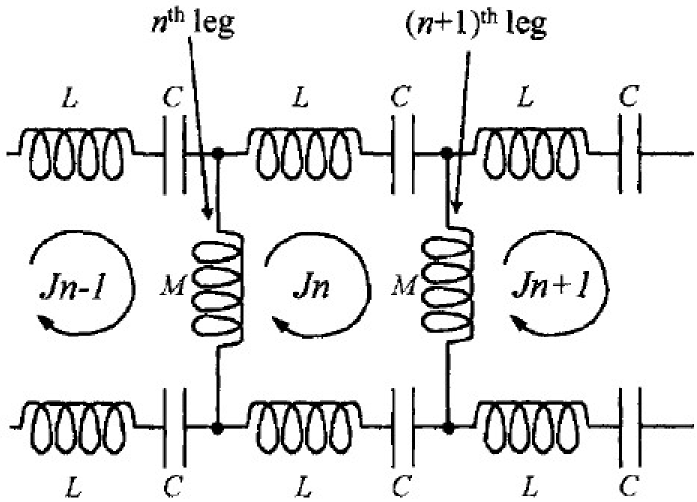

Figure 5.4: Electric circuit representation of an high-pass birdcage antenna. [26]

antenna are:

$$f_k = \frac{1}{2\pi\sqrt{C\left[L + 2Msin^2\left(\frac{\pi k}{N}\right)\right]}}, \qquad k = 0, 1, ..., N/2 \tag{5.4}$$

where k is the resonance mode. The resonance spectrum of an high-pass birdcage antenna is shown in Figure 5.5. In co-rotating (CR) mode the antenna exhibits a current flowing only through the end-rings with the same direction while in anti-rotating (AR) mode, that corresponds to $k = 0$, this two currents flow in opposite directions with respect to each other.[1]

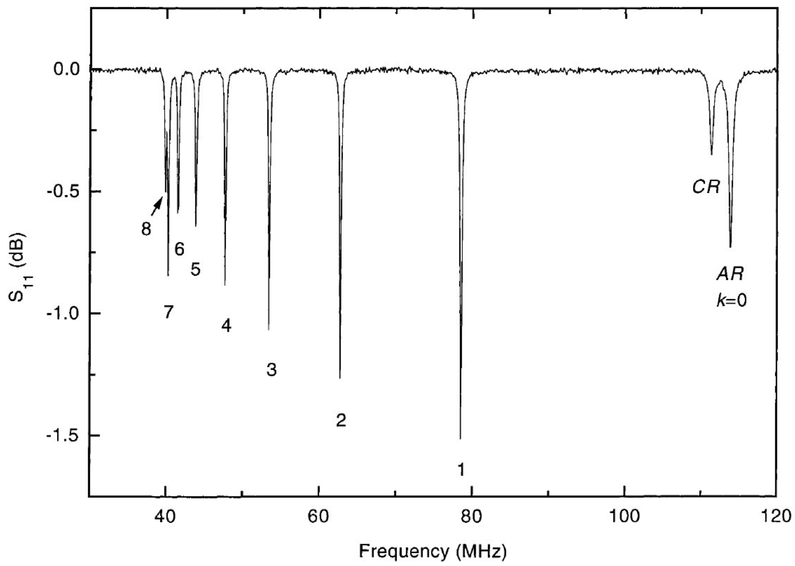

Figure 5.5: Resonance spectrum of a 16-legs high-pass birdcage. [39]

When the antenna is in resonance and it has one feed point, the current in the n^{th} leg is:[26]

$$(I_n)_k = I_0 sin\left(\frac{\pi k}{N}\right) sin\left[\frac{2\pi k(n - 0.5)}{N}\right] sin(\omega_k t) \qquad k = 0, 1, ..., N/2 \tag{5.5}$$

According to Equation (5.5), the current flow in the legs is sinusoidal and it has been represented in Figure 5.6 for the first three modes of a 16-legs high-pass antenna.

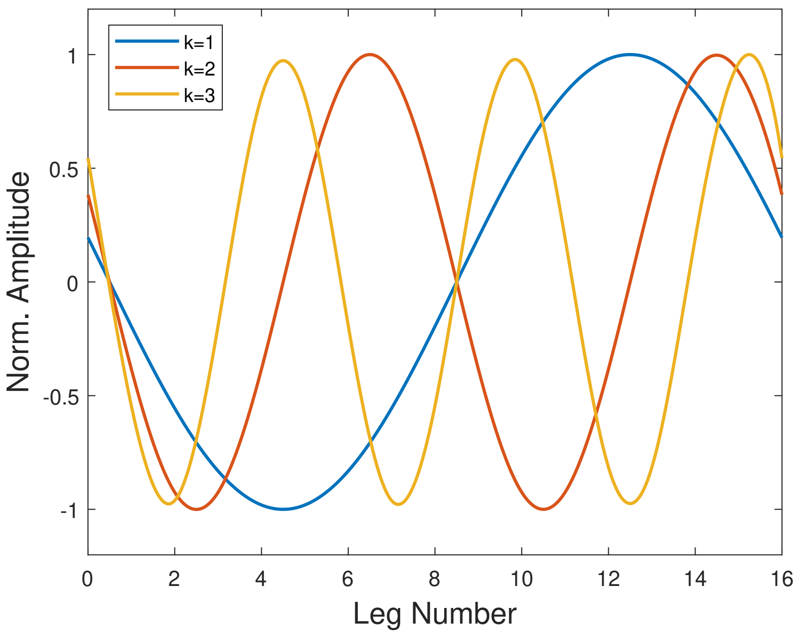

Figure 5.6: Interpolated current distribution of a 16-legs high-pass birdcage for three different resonance frequencies.

If the antenna is driven with a RF generator with frequency $f = f_1$, then, for a fixed time instance, the legs current is similar to the blue curve in Figure 5.6. When the device is excited with higher modes, the number of wavelengths in the antenna span increases coherently with the resonance mode k.

Instead, Figure 5.7 shows the variation in the legs current distribution for $k = 1$ when time changes. It can be seen that the current distribution behaves like a standing wave thus having always no current flow in leg 1 and 9.[33]

Using Biot-Savart law and the superposition principle, it can be found that a current distribution in the legs like the one in Figure 5.8a creates a magnetic field along the x-axis as shown in Figure 5.8b. As this legs current changes with a standing wave behavior, the magnetic field vector remains along the x-axis but its strength varies. So, when the antenna is driven through a single feed point, the magnetic field produced is linearly polarized and it points in the direction where the leg distribution current is zero.

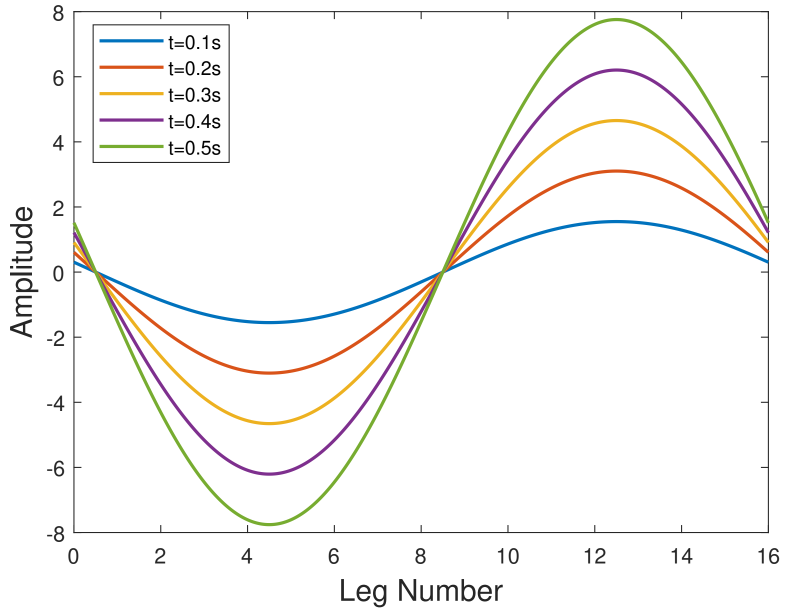

Figure 5.7: Interpolated current distribution of a 16-legs high-pass birdcage ($k = 1$) at different time instants.

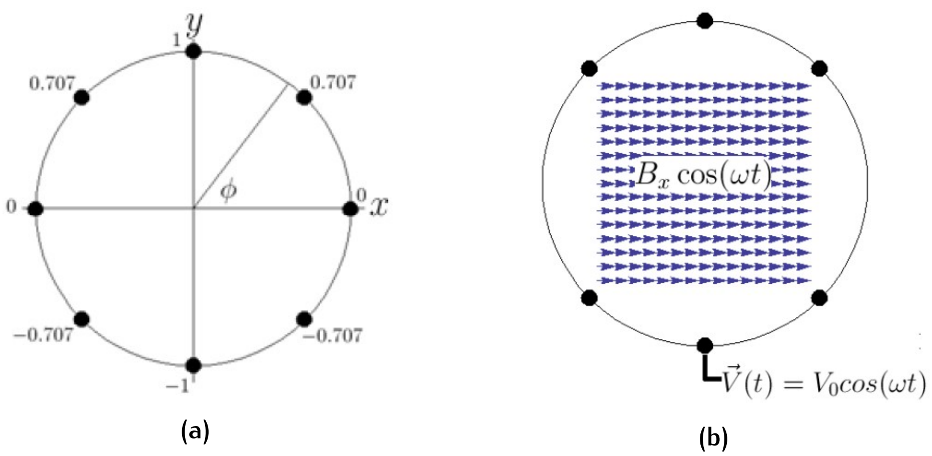

Figure 5.8: Top view of a birdcage antenna scheme. (a) Normalized legs current distribution of a 8-legs birdcage. (b) Linear polarized magnetic field created by a current standing wave in the antenna legs. [33]

The antenna can also be driven in quadrature mode when it is fed through two points 90° apart with two waves 90° out of phase. When the antenna is fed in this mode, there are two standing waves out of phase which create two linearly polarized magnetic fields 90° out of phase. Therefore, the antenna magnetic field is sum of these two linearly polarized magnetic fields along x-axis and y-axis. This creates a circularly polarized magnetic field that rotates with the same frequency of the RF generator (Figure 5.9) and it is described by the following equation:

$$\vec{B}_1(t) = B_1(cos(\omega t)\hat{x} + sin(\omega t)\hat{y}) \tag{5.6}$$

The magnitude of this vector is constant as shown in Equation (5.7).[38]

$$\begin{aligned} |\vec{B}_1(t)| &= |B_1(cos(\omega t)\hat{x} + sin(\omega t)\hat{y})| \\ &= |B_1|(cos^2(\omega t) + sin^2(\omega t)) = B_1 \end{aligned} \tag{5.7}$$

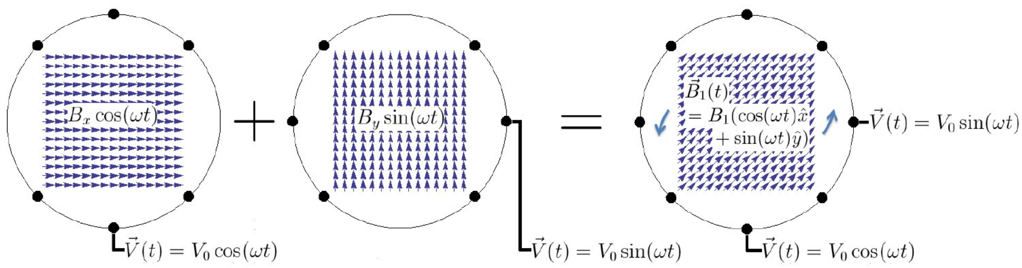

Figure 5.9: The circularly polarized magnetic field in a birdcage antenna driven in quadrature can be obtain by superposition of two single-driven birdcage antennae 90° apart and 90° out of phase. [38]

5.3 Conclusion

The birdcage antenna has not been used for space propulsion applications yet but, outside of the medical field, this device has already been tested for fusion applications.[30]

The advantage of this type of antenna is that, when it is driven in resonance, the antenna shows an impedance that is purely real, ideally reducing to zero the reflected power. In this way more power reaches the antenna and an high plasma density can be achieved.

Moreover, the birdcage antenna can be designed to have one of its resonance frequencies equal to the RF generator frequency in use through the choice of an adequate capacitance value.

Finally, a birdcage antenna has a sinusoidal current distribution in the azimuthal direction which creates an electromagnetic field that is reported to match the one of helicon wave.[12,26,30,43] When this wave is produced into the plasma, it has been reported that the plasma density increase.[53] For this reason, the birdcage is expected to produce a more dense plasma with the same input power of a coil antenna.

Chapter 6

Acceleration Stage

Electric propulsion systems used nowadays usually employ electrode grids to give a potential bias to charged particles. As result, particle are accelerated outside the thruster creating the desired thrust. The downsides of this technology are first, the grids finite lifetime due to plasma erosion and second, the plasma contamination with the electrodes remains. In order to achieve a reasonable lifetime, it is necessary to use an electrode-less type of acceleration stage.

6.1 Review

In an electric propulsion system the thrust is produced by accelerating plasma outside the thruster.

There are four main ways to achieve this effect:

- Lorentz force;

- electrothermal acceleration through electromagnetic nozzle or de Laval nozzle;

- acceleration by beating electrostatic waves;

- ponderomotive force.

In the first type, the thrust is produced through the Lorentz force shown in Equation (6.1) where $\vec{v}$ is the charged particles velocity.

$$\vec{F} = q\vec{E} + q\left(\vec{v} \times \vec{B}\right) \tag{6.1}$$

If the electrostatic part can be neglected, the Lorentz equation becomes:

$$\vec{F} = \vec{j} \times \vec{B} \tag{6.2}$$

HET and ion thruster, as described in Section 2.2, use the electrostatic part of the Lorentz force in Equation (6.1) to accelerate ions. Instead, acceleration strategies that use only the magnetic part of the Lorentz formula, shown in Equation (6.2), are: electromagnetic nozzle, rotating magnetic field (RMF), rotating electric field (REF) and theta-pinch thruster.

The electromagnetic nozzle is composed by divergent magnetic field lines in which, through the magnetic momentum conservation, the azimuthal particle motion is converted into axial net momentum gain. Instead, in the RMF coil antennae produce a rotating magnetic field into the plasma column. This motion creates an azimuthal electron movement that is converted into thrust by an electromagnetic nozzle. The REF is based on the same principle but instead of a magnetic field there is a rotating electric field created by two pairs of parallel plates placed outside the discharge tube. However, electromagnetic nozzle, rotating magnetic and electric field acceleration stages are examined in depth in Section 6.2, 6.3 and 6.4.

The theta-pinch thruster can be explained substituting the Ampere's law, $\nabla \times \vec{B} = \mu_0 \vec{j}$, into Equation (6.2). The following equation is obtained.

$$\vec{F} = -\vec{B} \times \vec{j} = \frac{\vec{B}}{\mu_0} \times \left(\nabla \times \vec{B}\right) \tag{6.3}$$

The vector identity in Equation (6.4) is used in the Lorentz force obtaining Equation (6.5).

$$\vec{B} \times \left(\nabla \times \vec{B}\right) = -\left(\vec{B} \cdot \nabla\right)\vec{B} + \frac{1}{2}\nabla|\vec{B}|^2 \tag{6.4}$$

$$\vec{F} = \frac{1}{\mu_0}\left(\vec{B}\cdot\nabla\right)\vec{B} - \nabla\left(\frac{|\vec{B}|^2}{2\mu_0}\right) \tag{6.5}$$

The first term on the right hand side is the magnetic tension parallel to $\vec{B}$ while the second term is the magnetic pressure parallel to $\nabla\vec{B}$. In a theta-pinch thruster, shown in Figure 6.1, an axial magnetic field, B_z, is created by a rapid current increase flowing into a coil driven by a capacitor discharge. As result, a force perpendicular to B_z pointing toward the center is created. This force compresses the plasma and it pushes charged particle outside creating the thrust.

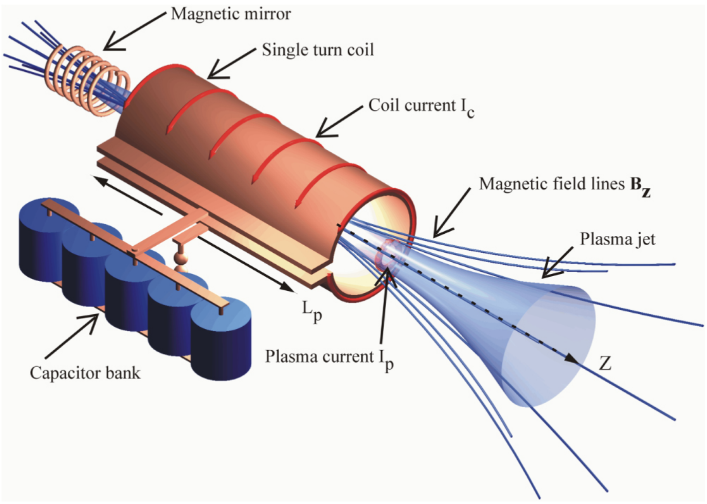

Figure 6.1: Theta-pinch thruster representation. The magnetic mirror, placed in the thruster back, is used to create a net thrust repulsing most of the particle coming out from that side. [4]

The second type is the electrothermal acceleration stage which is based on a heated plasma thermal expansion. This expansion can be converted into thrust by two nozzle types: electromagnetic or solid (also called de Laval). A solid nozzle is used, for example, in arcjets where the gas pressure acting on the nozzle surface establishes the thrust. However, a physical nozzle limits the exhaust velocity[32] as shown by Equation (6.6) where c_p is the specific heat of the propellant and T_c is the maximum temperature that can be reached by the thruster materials.

$$v_{ex} \leq \sqrt{2c_pT_c} \tag{6.6}$$

Electromagnetic nozzle does not have this limit because the particles expansion interacts with the nozzle magnetic field creating the thrust. Therefore, an electromagnetic nozzle is preferred when high-performance and long-lasting thruster are required.

The third category is the particles acceleration through electrostatic waves which are only composed by an oscillating electric field. Considering an ion spinning around the magnetic field lines with cyclotron frequency ω_{ci}; if a single electrostatic wave passes through the region where the ion is moving, then this particle can be accelerated by the wave only if its velocity is near the wave phase velocity. This phenomenon is called resonance. It has been shown that ions are in resonance with the electrostatic wave when their velocity is higher than the threshold velocity described by Equation (6.7). In this condition, particles gain energy from the wave and they stochastically increase their velocity.[57] This acceleration method is called single electrostatic wave (SEW).

$$v_{limit} = \frac{\omega}{k} - \sqrt{\frac{qE}{km}} \tag{6.7}$$

This threshold velocity can be eliminated if there are two electrostatic waves that respect the following beating criterion:

$$\omega_2 - \omega_1 = n\omega_{ci} \tag{6.8}$$

where $\omega_{1,2}$ are the angular frequencies of the two waves and n is an integer. When this criterion is respected, the acceleration strategy is called beating electrostatic waves (BEW). In this way, even ions that are not in resonance with the wave can be accelerated creating a more efficient acceleration than SEW.[14,35]

The last acceleration strategy is the ponderomotive force that is exerted on charged particles when they are immersed in an inhomogeneous electric field.[6] This electric field can be expressed by the following equation:

$$\vec{E} = \vec{E}_0(\vec{r})\cos(\omega_f t) \tag{6.9}$$

which is function of space and time. The particle undergoes an oscillation with the wave frequency, ω_f, and a ponderomotive force described by Equation

(6.10).

$$\vec{F} = -\frac{q^2}{4m_e\omega_f^2}\nabla E_0^2 \tag{6.10}$$

The force points in the opposite direction of the electric field gradient and pushes equally ions and electrons. If the plasma is magnetized the ponderomotive force assumes the following expression:

$$\vec{F}_{magn} = -\frac{q^2}{4m_e}\frac{1}{\omega_f^2 - \omega_{ce}^2}\frac{\partial {E_0}_z^2}{\partial z} \tag{6.11}$$

Within a magnetized plasma, the wave frequency and the magnetic field strength can be used to control the thrust direction and magnitude. When ω_f approaches ω_{ce} the wave is in resonance with the particle motion and the ponderomotive force is enhanced.

A practical explanation of the ponderomotive force can be given with the help of Figure 6.2. The magnetic field along x creates a cyclotron motion of the particle in the (y, z) plane. During the first half-cycle, the particle pass trough a zone where ∇E_0 is in the negative direction of y-axis and the particle undergoes a positive force along y. In the rest of the cycle, the particle crosses a zone where ∇E_0 has a lower magnitude and it is in the positive direction of y-axis. Therefore, the ponderomotive force is in the negative y direction. The net force exerted on a particle is then along y. This is possible only in a inhomogeneous electric field, otherwise the net force would be zero.

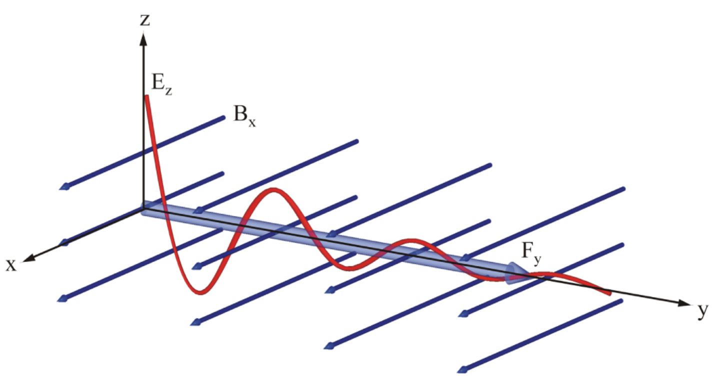

Figure 6.2: Ponderomotive force in a magnetized plasma due to the gradient of E_z. [4]

6.2 Electromagnetic Nozzle

An electromagnetic nozzle (EN) is composed by divergent magnetic field lines that resemble a solid de Laval nozzle. This device is created by permanent magnets or electromagnets that can be positioned in different way in order to create the desired magnetic field topology. A scheme of the electromagnetic nozzle is shown in Figure 6.3.

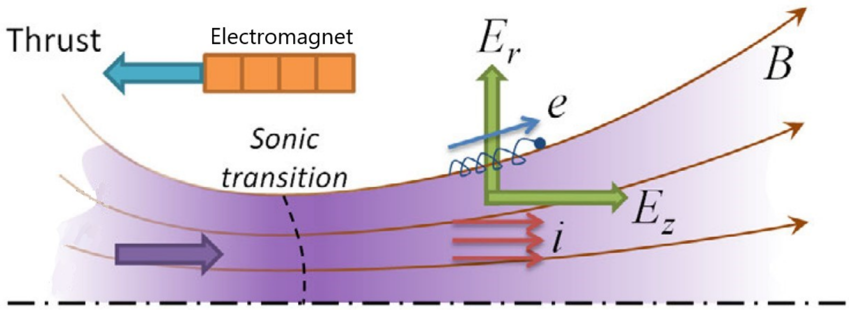

Figure 6.3: Electromagnetic nozzle geometry created by a single electromagnet. Electrons are the only species magnetized and thus they have a cyclotron motion around the magnetic field lines. Figure adapted from [40].

In the EN electrons are usually the only species magnetized since this is sufficient to achieve the electromagnetic nozzle effect desired.[40] For this reason, the electron motion is tied up to the magnetic field lines while ion motion is not affected. Electrons move faster than any other species because they are the lightest and therefore they moves ahead following the magnetic field lines. This creates a charge separation between ions and electrons that gives rise to an ambipolar electric field in both axial, E_z, and radial direction, E_r, in order to maintain the plasma quasi-neutrality. The radial ambipolar electric field forces ions to expand in the nozzle while the axial component accelerates ions and slows down electrons. The ambipolar electric field transfers electrons internal energy into directed ions kinetic energy but it is an internal force and does not produce axial momentum gain.

There is another effect in the electromagnetic nozzle which is responsible of the thrust production: the magnetic momentum conservation shown in

Equation (6.12).

$$\mu = \frac{1}{2}\frac{mv_\perp^2}{B} = const. \tag{6.12}$$

Electrons are usually the only species that has a cyclotron motion around the field line and therefore their velocity is mostly perpendicular to $\vec{B}$.[42] When particles move away from the EN throat, the magnetic field magnitude decreases and so the particle perpendicular velocity in order to maintain μ constant. Since the kinetic energy must remain constant, the electrons perpendicular velocity is converted into parallel one. So, the magnetic momentum conservation in the EN transforms the particles azimuthal velocity into axial one as they move along the electromagnetic nozzle. Thanks to this increased axial velocity, electrons accelerate ions along the nozzle through the ambipolar electric field that is created to maintain the plasma quasi-neutrality. Therefore, the electromagnetic nozzle accelerates outside both of the plasma species maintaining the plume neutrality.[40,42]

The electromagnetic nozzle thrust can be divided into two components: T_S, produced by the particles pressure on the discharge tube back wall and T_B, called magnetic thrust, that is the axial momentum gain as the plasma flows downstream the nozzle.

The electromagnetic nozzle production device can be sketched with an azimuthal current I_θ as show in Figure 6.4. This current creates a magnetic field that is the electromagnetic nozzle. Therefore, electrons start their gyration around the field lines and this motion gives rise to an electron azimuthal current density, $j_{\theta e} = -qn_0v_\theta$. Even if ions are not magnetized, they may start to rotate too[42] creating an azimuthal ion current $j_{\theta i} = qn_0u_\theta$. If $|j_{\theta e}| > |j_{\theta i}|$, the net azimuthal current in the plasma is opposite to the one that creates the EN (diamagnetic current), the magnetic force between the two loops is repulsive and the thrust is transmitted to the the device that creates the EN and therefore to the thruster structure. This case is shown in Figure 6.4a. Otherwise, if $|j_{\theta e}| < |j_{\theta i}|$, the two currents have the same direction (paramagnetic current) and a negative magnetic thrust or drag is produced as shown in Figure 6.4b.[42]

The thrust produced by an electromagnetic nozzle can be enhanced if a device, after the neutral gas ionization, is able to increase the azimuthal

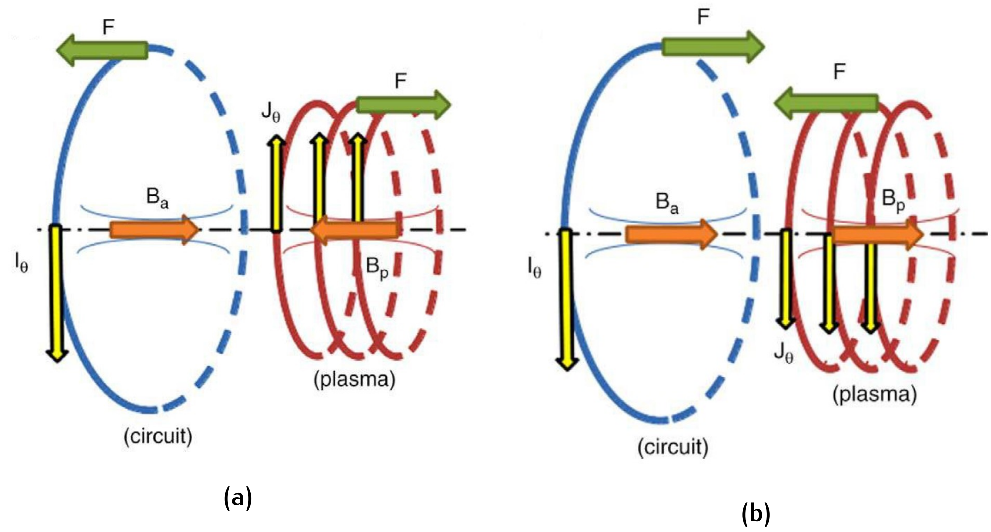

Figure 6.4: Magnetic thrust through (a) diamagnetic and (b) paramagnetic current. In (a) the thrust is produced in the spacecraft motion direction while in (b) no effective thrust is produced. [42]

motion of the charged particles.[40]

6.2.1 Plasma Detachment

The magnetic field lines close upon themselves since $\nabla \cdot \vec{B} = 0$ and the charged particles that are tied up to the field lines could eventually return to the thruster. If detachment is not achieved, the plasma could reach the spacecraft surfaces damaging them, canceling the thrust and charging the satellite.[40]

There are five mechanism for plasma detachment that has been proposed so far:

- **Recombination.** Gerwin *et Al.*[25] explain the plasma detachment as consequence of particle recombination after the plasma has been accelerated. As the gas becomes neutral, the particles are no longer influenced by the EN and the detachment is achieved. However, Martinez[40] estimates that recombination happens in more than 10 m for a plasma density in the order of $10^{19}\,\mathrm{m}^{-3}$. Therefore this mechanism is not responsible for plasma detachment since the recombination takes place in larger scale with respect to the EN dimensions.

- **Plasma resistivity.** The theory of Gerwin *et Al.*[25] suggests that the collisional process could allow the inward plasma diffusion which eventually lead to plasma detachment.

- **Electron inertia effects.** Hooper[28] suggests that electron inertia is sufficient for particle pairs of electron-ion to detached from the magnetic field lines.

- **Magnetic stretching of the EN**. This theory, proposed by Arefiev *et Al.*[2], claims that the fields produced by plasma can modify the EN field itself in a way to decrease the electromagnetic nozzle divergence downstream without the need of any detachment.

- **Ion demagnetization.** Martinez[40] proposes that ions gradually demagnetize as they move downstream. When the magnetic field strength becomes so low that is not able to deflect the ion trajectories anymore, the ions detaches from the EN dragging electrons to maintain the quasineutrality.

However, despite these possible explanations, a clear theory supported by most of the researchers has not been established yet.

6.2.2 Thrust Model

The thrust exerted by an electromagnetic nozzle has the same magnitude of the total momentum flux produced but opposite direction. The thrust is sum of the static and dynamic pressure integrated over the cross section A. An analytic expression is shown in Equation (6.13) where p_e is the electron static pressure proportional to the electron temperature and $m_i n_0 u_z^2$ is the ion dynamic pressure. The ion static pressure has been neglected since ion temperature is much less than electron one. The same has been done with the electron dynamic pressure since electrons are lighter than ions.

$$T = \int_A \left(p_e + m_i n_0 u_z^2\right) dA \tag{6.13}$$

The momentum equation in a steady state collision-less plasma is:

$$m_j n_j \left(\vec{v}_j \cdot \nabla\right) \vec{v}_j = q_j n_j \left(\vec{E} + \vec{v}_j \times \vec{B}\right) - \nabla p_j \tag{6.14}$$

where j indicates the particle species. In an axis-symmetric system ($\partial/\partial\theta = 0$) with a quasineutral plasma ($n_j = n_0$), a negligible ion temperature and therefore ion pressure, the radial and azimuthal components of Equation (6.14) become:

$$-en_0(E_r + v_\theta B_z) = \frac{\partial p_e}{\partial r} \tag{6.15}$$

$$-en_0\left(E_z - v_\theta B_r\right) = \frac{\partial p_e}{\partial z} \tag{6.16}$$

$$-en_0(E_r + u_\theta B_z) = 0 \tag{6.17}$$

$$en_0\left(E_z - u_\theta B_r\right) = \frac{1}{r}\frac{\partial}{\partial r}(r m_i n_0 u_r u_z) + \frac{\partial}{\partial z}(m_i n_0 u_z^2) \tag{6.18}$$

where u is the ion velocity while v is the electron velocity. Moreover, the radial ion inertia has not been considered for simplicity and $B_\theta = 0$ because the electromagnetic nozzle field lines are not twisted. The continuity equation, as shown in (6.19), has been used in order to find Equation (6.18).

$$\frac{1}{r}\frac{\partial}{\partial r}(r u_r) = -\frac{\partial u_z}{\partial z} \tag{6.19}$$

Substituting E_z from Equation (6.16) into (6.18), the following relation is obtained.

$$en_o(v_\theta - u_\theta)B_r = \frac{1}{r}\frac{\partial}{\partial r}(r m_i n_0 u_r u_z) + \frac{\partial}{\partial z}(p_e + m_i n_0 u_z^2) \tag{6.20}$$

Instead, equations (6.15) and (6.17) gives

$$en_0(u_\theta - v_\theta) = \frac{1}{B_z}\frac{\partial p_e}{\partial r} \tag{6.21}$$

that is the azimuthal current created by the radial electron pressure. The RHS of this equation does not present a term that depends on ions characteristics because it has been neglected in the model hypothesis.

Inserting Equation (6.21) into (6.20), the following relation is obtained.

$$\frac{\partial}{\partial z}(p_e + m_i n_0 u_z^2) = -\frac{\partial p_e}{\partial r}\frac{B_r}{B_z} - \frac{1}{r}\frac{\partial}{\partial r}(r m_i n_0 u_r u_z) \tag{6.22}$$

Assuming the radius of the plasma expanding through the electromagnetic nozzle as $r_p(z)$ and the plasma source radius as r_s, the following thrust equations can be obtained inserting Equation (6.22) into (6.13):

$$T = T_S + T_B + T_W \tag{6.23}$$

$$T_S = 2\pi \int_{r_s} p_{e0} r dr \tag{6.24}$$

$$T_B = -2\pi \int_z \int_{r_p} \frac{B_r}{B_z} \frac{\partial p_e}{\partial r} r dr dz \tag{6.25}$$

$$T_W = -2\pi \int_z \int_{r_p} \frac{\partial}{\partial r}(r m_i n_0 u_r u_z) dr dz = 0 \tag{6.26}$$

T_W is zero[20] due to integration of ion velocity across the plasma radial cross section.

T_S is the thrust produced by the static electron pressure, p_{e0}, acting on the thruster back plate. It corresponds to the constant of integration when the thrust is integrated along z. Near the back plate a sheath is formed when electrons recombine into the plate and ions are accelerated by the potential difference of the sheath.

T_B is the magnetic thrust created by the electromagnetic nozzle. It is opposite to the Lorentz force produced by the radial component of the magnetic field and the diamagnetic azimuthal current $j_\theta = B_z^{-1} \partial p_e / \partial r$.

The thrust components in an EN are represented in Figure 6.5.

Fruchtman *et Al.*[20] derived a one-dimensional thrust model for T_B. Integrating by parts Equation (6.25) the magnetic thrust becomes:

$$T_B = -2\pi \int_z \int_{r_p} \frac{B_r}{B_z} p_e r dr dz + 2\pi \int_z \int_{r_p} \frac{\partial}{\partial r}\left(\frac{B_r}{B_z} r\right) p_e dr dz \tag{6.27}$$

in which the first term on the right hand side is equal to zero since $B_r = 0$ on the axis and $p_e = 0$ on the EN external surface. Instead, the derivative in the second term on the RHS can be written as:

$$\frac{\partial}{\partial r}\left(\frac{B_r}{B_z} r\right) = \frac{\partial B_r}{\partial r} \frac{1}{B_z} r + B_r \frac{\partial (1/B_z)}{\partial r} r + \frac{B_r}{B_z} \tag{6.28}$$

The magnetic field is divergence-free, $\nabla \cdot \vec{B} = 0$, therefore:

$$\frac{\partial B_z}{\partial z} = -\frac{1}{r} \frac{(r B_r)}{\partial r} = -\frac{\partial B_r}{\partial r} - \frac{B_r}{r} \tag{6.29}$$

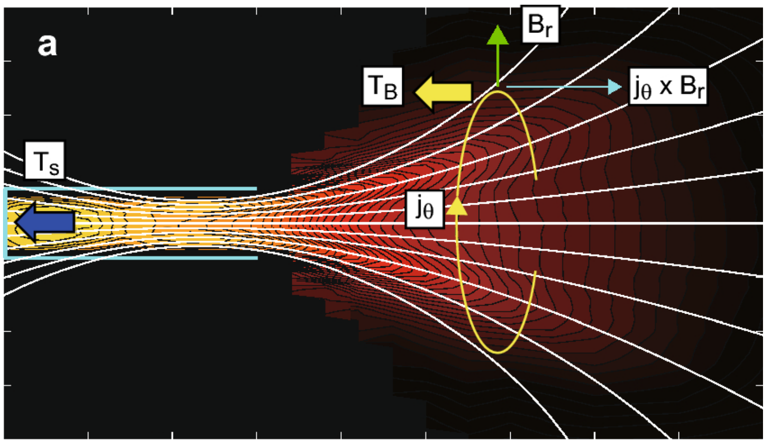

Figure 6.5: Electromagnetic nozzle geometry where the two thrust components, T_B and T_S, are indicated. T_S is created by pressure on the back plate while T_B is originated from the net azimuthal current and the radial component of the magnetic field. Figure adapted from [60].

Now with adequate substitutions, T_B becomes:

$$T_B = -2\pi \int_z \int_{r_p} \frac{1}{B_z} \frac{\partial B_z}{\partial z} p_e r dr dz + 2\pi \int_z \int_{r_p} B_r \frac{(1/B_z)}{\partial r} p_e r dr dz \qquad (6.30)$$

Adding the one-dimensional hypothesis $B_z(r, z) \simeq B_z(0, z)$, the one-dimensional thrust produced by the EN is

$$T_B = -\int_z \langle p_e(z) \rangle A(z) \frac{1}{B_z} \frac{\partial B_z}{\partial z} dz \qquad (6.31)$$

where $A(z)$ is the cross section of the plasma and $\langle p_e(z) \rangle$ is the radially-averaged plasma pressure. Takahashi[60] reports that the one-dimensional thrust in Equation (6.31) underestimates the thrust given by the two-dimensional model in Equation (6.25) by 15–25 %.

6.2.3 Performance

The theory in section 6.2.2 is in agreement with the laboratory experiments conducted by Takahashi *et Al.*[62] The thruster used in their experiments is composed by: a Pyrex tube 25 cm long with a 9 cm diameter, a two turns antenna of 11 cm diameter driven with RF voltage at 13.56 MHz and two electromagnets positioned around the discharge chamber. Two cases have been analyzed:

- **case A**: both electromagnets are turned on;
- **case B**: only the electromagnet close to the discharge tube end is active.

The magnetic field topology in these two cases is shown in Figure 6.6.

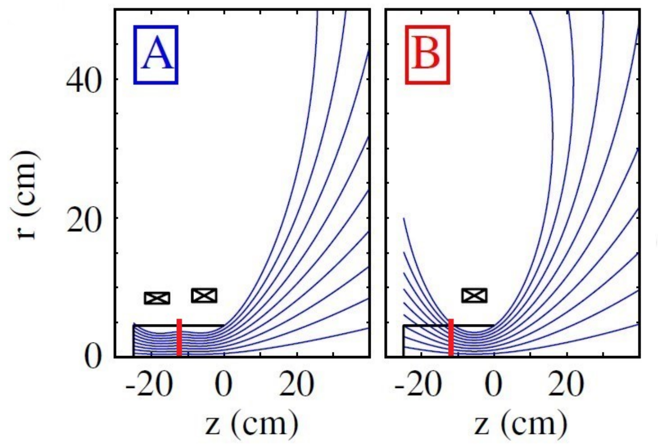

Figure 6.6: Two different electromagnetic nozzle topologies used by Takahashi *et Al.* The red rectangle in the source tube represents the antenna. Figure adapted from [62].

The authors have acquired data of the total and magnetic thrust. This have been done mounting the electromagnets onto a thrust balance and fixing the rest of the thruster to the vacuum chamber. Electron temperature and plasma density are shown in Figure 6.7. Temperatures and densities in the discharge tube are approximately equal in both cases for the same effective rf power.

The electron pressure is found with $p_e = n_0 k_B T_e$ and its normalize value with respect to plasma density and electron temperature at each axial position is shown in Figure 6.8. In case A the pressure drops fast near the thruster exit while in case B this drop is more gradual. The electron pressure drop is mainly due to the density decrease since the electron temperature remains approximately constant.[61]

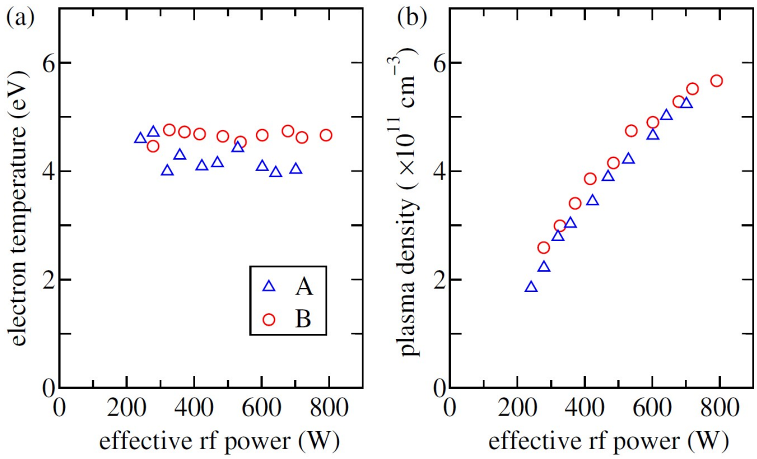

Figure 6.7: (a) Electron temperature and (b) plasma density in the source tube over the measured RF power absorbed. [61]

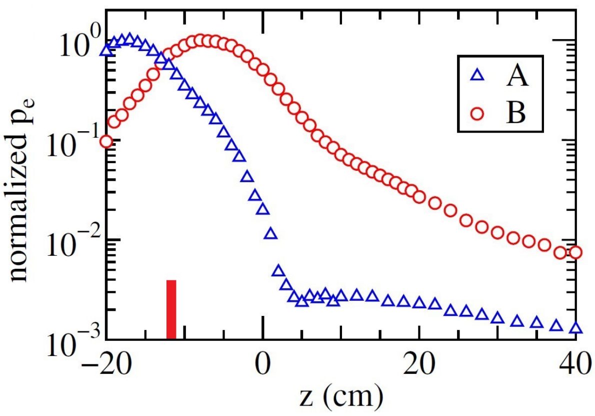

Figure 6.8: Axial profile of the normalized electron pressure with 470 W of RF power absorbed in case A and 540 W in case B. The red rectangle represents the antenna. [61]

The thrust results are shown in Figure 6.9. Case B produces more than the double of the thrust of case A; the maximum is 6.2 mN with respect to 2.5 mN of case A.

The experimental results are mostly in agreement with the theory. Case B has the worst accuracy probably due to the model hypothesis. In case B the thrust produced is higher because the electron pressure reduction is slower.

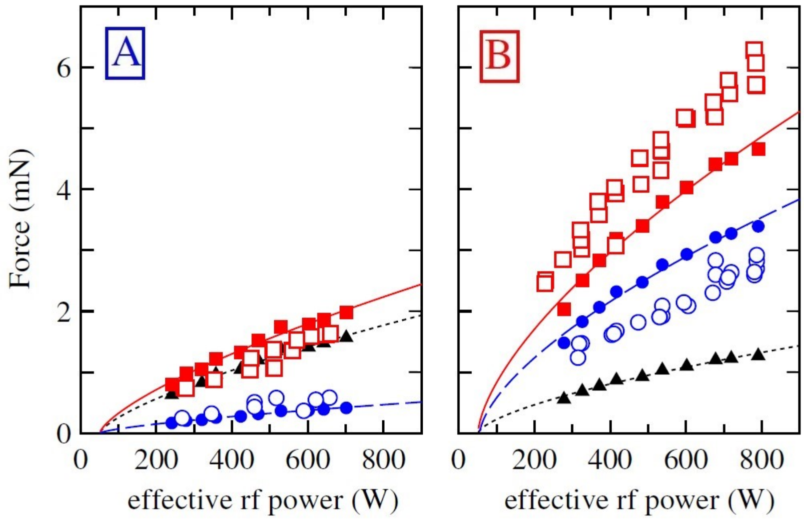

Figure 6.9: Results from Takahashi *et Al.* experiments. The filled geometrical figures represent the theoretical values while the empty one indicates the experimental data. The total thrust is indicated by squares, the magnetic thrust (T_B) by circles and the pressure on the thruster back plate (T_S) by triangles. [61]

6.3 Rotating Magnetic Field

The rotating magnetic field (RMF) acceleration stage is based on the Lorentz force. A rotating magnetic field, created by four antennae, induces an azimuthal current j_θ into the plasma. An external electromagnet establishes a divergent magnetic field into the acceleration stage. The cross product between the azimuthal current density and the radial component of the externally applied magnetic field produces an axial Lorentz force that accelerates the plasma.

This acceleration stage can be seen like an electromagnetic nozzle where the electron azimuthal current is enhanced by antennae in order to improve its thrust performance.

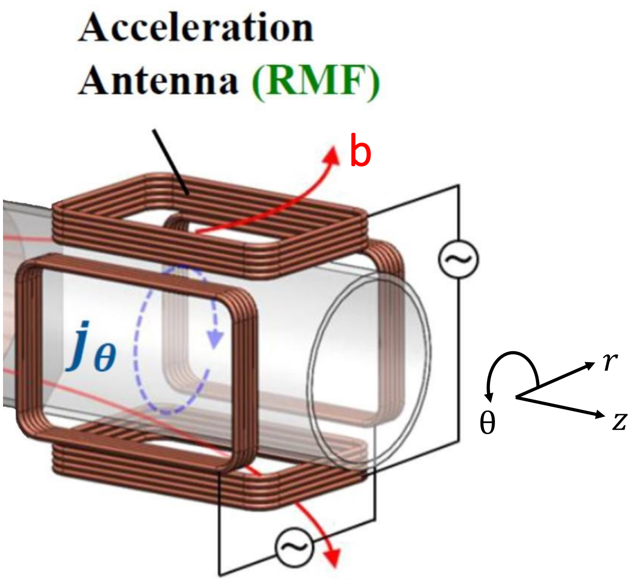

Figure 6.10: RMF scheme showing four coils, driven with sinusoidal voltage, that produce a rotating magnetic field inside the discharge tube. This rotation induces an azimuthal current that, with the radial component of the external magnetic field, accelerates the plasma. Figure adapted from [55].

The RMF acceleration stage can be composed, for example, by four coils, called acceleration antennae, arranged like in Figure 6.10. The opposite antennae are connected together. These two pairs are driven with two sinusoidal voltages with frequency f and 90° out of phase. This system creates a magnetic field $\vec{B}_\omega$ that rotates in the cross section of the discharge tube with angular frequency ω as shown in Figure 6.11.

From now on to the end of this chapter, the upper case B is used to indicate the rotating magnetic field while the lower case indicates the static magnetic field produced by the electromagnetic nozzle.

Equation (6.32) is the Faraday's law of induction and it is used to find the electric field induced by the rotating magnetic field.[22]

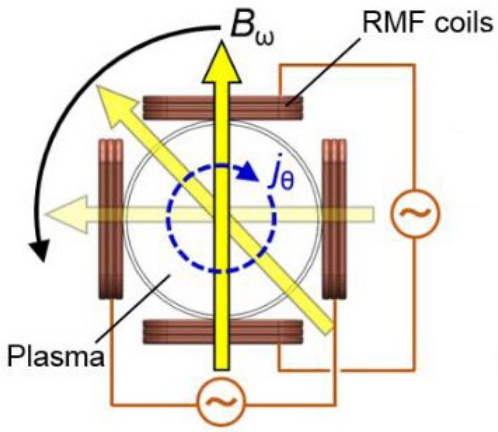

Figure 6.11: Radial view of RMF stage. Two pairs of opposite coils create a rotating magnetic field $\vec{B}_\omega$ that induces an azimuthal current j_θ in the plasma. [22]

$$\nabla \times \vec{E} = -\frac{\partial \vec{B}_\omega}{\partial t} \tag{6.32}$$

$\vec{B}_\omega$ and its time derivate are written in cylindrical coordinates as follow.

$$\vec{B}_\omega = \begin{Bmatrix} B_\omega \cos(\omega t - \theta) \\ B_\omega \sin(\omega t - \theta) \\ 0 \end{Bmatrix}, \qquad -\frac{\partial \vec{B}_\omega}{\partial t} = \begin{Bmatrix} B_\omega \omega \sin(\omega t - \theta) \\ -B_\omega \omega \cos(\omega t - \theta) \\ 0 \end{Bmatrix} \tag{6.33}$$

Substituting Equation (6.33) into (6.32), the following relation is obtained:

$$\begin{Bmatrix} \frac{1}{r}\frac{\partial E_z}{\partial \theta} - \frac{\partial E_\theta}{\partial z} \\ \frac{\partial E_r}{\partial z} - \frac{\partial E_z}{\partial r} \\ \frac{1}{r}\left[\frac{\partial (rE_\theta)}{\partial r} - \frac{\partial E_r}{\partial \theta}\right] \end{Bmatrix} = \begin{Bmatrix} B_\omega \omega \sin(\omega t - \theta) \\ -B_\omega \omega \cos(\omega t - \theta) \\ 0 \end{Bmatrix} \tag{6.34}$$

An analytic expression can be found if $\partial E_\theta / \partial z = 0$. This hypothesis is true if the position along z-axis is sufficiently away from the antennae edge. Integration of the first line of Equation (6.34) gives the following relation.[64]

$$E_z = B_\omega r \omega \cos(\omega t - \theta) \tag{6.35}$$

Therefore, a magnetic field that rotates in the (r, θ) plane creates an alternating electric field along z.

If the angular frequency is taken to be $\omega_{ce} \ll \omega \ll \omega_{ci}$, where these cyclotron frequencies are referred to the rotating magnetic field strength, ions can be considered fixed while electrons are free to move.

The generalized Ohm's law can be written as:[34]

$$\vec{E} - \frac{1}{n_e e}(\vec{j} \times \vec{B}) = \eta \vec{j} \tag{6.36}$$

where the second term on the LHS is called Hall's term while the one on the RHS is called resistive term. The cylindrical components of this equation are

$$\begin{Bmatrix} E_r \\ E_\theta \\ E_z \end{Bmatrix} - \frac{1}{n_e e} \begin{Bmatrix} j_\theta B_z - j_z B_\theta \\ j_z B_r - j_r B_z \\ j_r B_\theta - j_\theta B_r \end{Bmatrix} = \eta \begin{Bmatrix} j_r \\ j_\theta \\ j_z \end{Bmatrix} \tag{6.37}$$

If there is a radial current in the plasma, the electrons tends to move toward the center while ions are too heavy to move from their position. This motion creates a charge separation and an electrostatic field that moves back electrons to their original position. The radial motion of electrons can be neglected and so $j_r = 0$.[34] With this hypothesis, the Ohm's law can be simplified and Equation (6.38) is obtained.

$$\begin{Bmatrix} E_r \\ E_\theta \\ E_z \end{Bmatrix} - \frac{1}{n_e e} \begin{Bmatrix} j_\theta B_z - j_z B_\theta \\ j_z B_r \\ -j_\theta B_r \end{Bmatrix} = \eta \begin{Bmatrix} 0 \\ j_\theta \\ j_z \end{Bmatrix} \tag{6.38}$$

If the resistive term on the RHS dominates, the presence of an alternating electric field E_z creates a time-varying current j_z that is delayed with respect to the electric field as much as the resistivity value increases. Thus, the Hall's term has only a radial and azimuthal component $j_z B_\theta$ and $j_z B_r$, respectively. These two components are:

$$\begin{aligned} j_z B_\theta &\propto \cos(\omega t - \theta)\sin(\omega t - \theta) \\ j_z B_r &\propto \cos^2(\omega t - \theta) \end{aligned} \tag{6.39}$$

These are oscillations with frequency $2f$ around zero for the radial component and around $\frac{B_\omega^2 r\omega}{2n_e e\eta^2}$ for the azimuthal component. Taking the mean over one period, only the constant part (even called "dc part") of the azimuthal component remains. This creates a net azimuthal electron motion and then a current described by:

$$j_\theta(r) = -n_e e v_{e\theta}(r) \tag{6.40}$$

Otherwise, if the Hall's term dominates, the current delay decreases and the electron velocity approaches its maximum value:[22,34,47]

$$v_{e\theta\, max} = r\omega \tag{6.41}$$

Finally, the azimuthal electron motion is transformed into thrust in the electromagnetic nozzle. The thrust produced can be found with the axial component of Lorentz force described by Equation (6.42).

$$F_z = -j_\theta b_r \tag{6.42}$$

The radial component has not been considered since it is equal to zero when integrated over the cross section. The thrust can be estimated with integration of the Lorentz force along z over concentric circumferences with radius $[0, r]$ and multiplied by the length of the acceleration stage L_z.

$$T = L_z \int_0^r j_\theta b_r (2\pi r') dr' \tag{6.43}$$

Since $j_\theta \propto \omega r$ and $b_r \propto b_z(r/2R)$[54] with R the position of coils that creates the static magnetic field, the thrust is:

$$T \propto \frac{\pi L_z b_z \omega r^4}{4R} \tag{6.44}$$

6.3.1 RMF Penetration

In the RMF penetration topic is handy to define two dimensionless parameters:

$$\lambda = \frac{R}{\delta} = R\left(\frac{\mu_0\omega}{2\eta}\right)^{1/2} \qquad \gamma = \frac{\omega_{ce}}{\nu_{ei+en}} = \frac{1}{e}\left(\frac{B_\omega}{n\eta}\right) \tag{6.45}$$

where λ is the inverse of the skin depth normalized with the quartz tube radius and γ is the Hall's parameter with ν_{ei+en} the collision rate of electron-ion and electron-neutral. This phenomenon has been studied by *Milroy*[44] with numerical solution of MHD equations. It has been found that γ has a critical value, γ_c, above which the magnetic field penetrates completely the plasma.

The magnetic field penetration is described by the empirical formula in Equation (6.46). If λ is less than 6.5, γ_c to achieve penetration of magnetic field lines is the same for expulsion, while for $\lambda > 6.5$ it is required an higher magnetic field magnitude to completely penetrate the plasma than for the field line expulsion. In this case, it is possible to reduce the applied magnetic field intensity after achieving the complete penetration.

$$\gamma_c = \begin{cases} 1.12\lambda & \text{if } \lambda \leq 6.5 \\ 1.12\lambda \left[1.0 + 0.12(\lambda - 6.5)^{0.4}\right] & \text{otherwise} \end{cases} \tag{6.46}$$

Furukawa *et al.*[22] plotted the results of Milroy's equation for four RMF frequencies in the range 0.7–5 MHz and five radial positions. As shown in Figure 6.12, full penetration is obtained with 0.7 MHz while the other frequencies have at least the central part of the plasma discharge where the magnetic field is not able to penetrate.

In the IRS case, if the RMF acceleration stage is driven with the same generator used to feed the birdcage antenna, then the frequency of the RMF would be 40.68 MHz, therefore higher than the one used by Furukawa *et al.*[22] This causes the increase of λ and so the critical value of the Hall's parameter. The resistivity has to be calculated experimentally to have a realistic value of $\frac{\gamma}{\lambda}$ and to check if, even with a frequency of 40.68 MHz, the condition of the magnetic field penetration is met at least in the peripheral region. Despite this problem, an high value of f_{RMF} is preferable since it increases the azimuthal current and then the thrust produced.

However, Shinohara *et al.*[55] report that the incomplete penetration of the magnetic field may not produce a substantial decrease of the thrust performance since the azimuthal current, being proportional to the radius, is dominant in the plasma edge region.

6.3.2 Current Verification and Performance

Shinohara *et Al.*[23] have estimated the dc part of the azimuthal current and they have verified its frequency as $2f_{RMF}$ with the use of a B-dot probe.

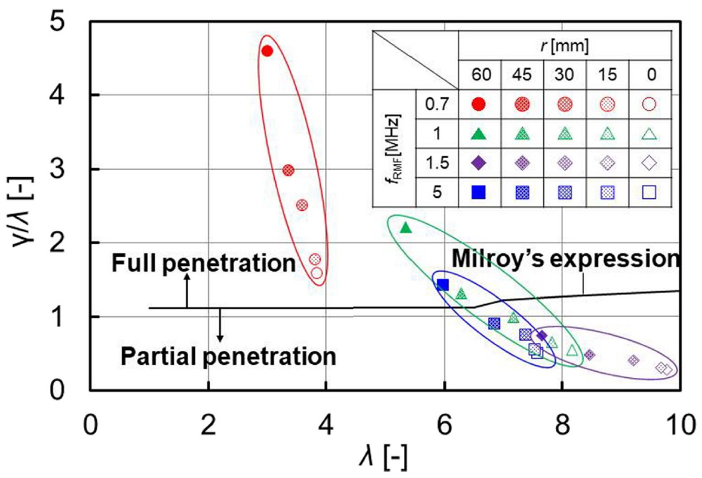

Figure 6.12: Experimental data of $\frac{\gamma}{\lambda}$ versus λ for difference frequency and radial positions. The values are compared with the Mirloy's expression indicated by the black line. [22]

The azimuthal current, proportional to $\cos^2(\omega t - \theta)$, can be decomposed as:

$$j_\theta = j_{\theta dc} + \tilde{j_\theta} \tag{6.47}$$

where $j_{\theta dc}$ is the constant part and $\tilde{j_\theta}$ is the oscillation around the dc part, sometimes referred as "ac". $\tilde{j_\theta}$ can be found measuring changes in the magnetic field components through the Maxwell-Ampere law in Equation (6.48) written in a cartesian reference frame.

$$\tilde{j_y} = \frac{1}{\mu_0}\left(\frac{\partial B_x}{\partial z} - \frac{\partial B_z}{\partial x}\right) \tag{6.48}$$

The ac azimuthal current density calculated by Shinohara *et Al.*[23] has a period of $T_{RMF}/2$ that is in agreement with the theory and it oscillates with an amplitude of $\sim$60 A/m^2 around zero. The B-dot probe is able to measure only the current variations produced by magnetic field changes and therefore any dc azimuthal current cannot be measured directly. For this reason, the ac azimuthal current curve is an oscillation around zero. However, the theory explains that the azimuthal current has a dc part and j_θ should resemble the $\cos^2(\omega t - \theta)$ function. Therefore, the oscillation around zero calculated by the B-dot probe has to be moved up of $\sim$60 A/m^2 obtaining a graph similar to $\cos^2(\omega t - \theta)$ in order to take into account event the dc azimuthal current that the probe is not able to measure. In this way, the constant value of the azimuthal current corresponds to half of the peak-to-peak value of this new curve. The current produced by the RMF in the experimental conditions of Ref. [23] is ∼0.8 A, far from the theoretical value of 40 A. The authors explain this inconsistency with tree observations. First, the antenna has a finite axial length and this creates a non uniform axial distribution in contrast with the theoretical model hypothesis, second, the external magnetic field is not uniform and third, the axial plasma flow may lower the acceleration efficiency. Thus, the axial thrust produced with $f = 0.7\,\text{MHz}$ and $I_{RMF} = 40\,\text{A}_{\text{pp}}$ is $F_z \sim 4.3\,\text{mN}$.

6.4 Rotating Electric Field

The rotating electric field (REF) technique is similar to the previous one but, instead of a rotating magnetic field, there is a spinning electric field that induces an electrons rotation. Once again, this motion creates an azimuthal current density that, with the radial component of an externally applied magnetic field, is converted into thrust.

The particles motion can be found solving the Lorentz equation:[46]

$$m\frac{d\vec{v}}{dt} = q(\vec{E} + \vec{v} \times \vec{B}) \tag{6.49}$$

with the fields shown in Equation (6.50) where ω is the angular frequency of the REF.

$$\vec{E} = \begin{Bmatrix} E_0\cos(\omega t + \alpha) \\ E_0\sin(\omega t + \alpha) \\ 0 \end{Bmatrix} \qquad \vec{B} = \begin{Bmatrix} 0 \\ 0 \\ b_z \end{Bmatrix} \tag{6.50}$$

The induced magnetic field and the radial component of the static magnetic field are not taken into account for simplicity.

Writing the components of Equation (6.49) and applying the separation of variables, the following non-homogeneous differential equations are obtained:

$$\begin{cases} v_x'' + \omega_c^2 v_x = \frac{E_0\omega_c^2}{B_z}\left(1 - \frac{\omega}{\omega_c}\right)\sin(\omega t + \alpha) \\ v_y'' + \omega_c^2 v_y = -\frac{E_0\omega_c^2}{B_z}\left(1 - \frac{\omega}{\omega_c}\right)\cos(\omega t + \alpha) \end{cases} \tag{6.51}$$

Solutions of Equation (6.51) with adequate boundary conditions are:

$$\begin{cases} v_x = v_0 \cos(\omega_c t + \delta) + \frac{eE_0}{m\omega} \frac{1}{1+\omega_c/\omega} \sin(\omega t + \alpha) \\ v_y = -v_0 \sin(\omega_c t + \delta) - \frac{eE_0}{m\omega} \frac{1}{1+\omega_c/\omega} \cos(\omega t + \alpha) \end{cases} \tag{6.52}$$

Therefore, the particle trajectory is sum of a cyclotron motion around b_z on the RHS left part and a $\vec{E} \times \vec{B}$ drift on the right. The particle trajectory can be found integrating Equation (6.52) and it is shown in Figure 6.13.[46]

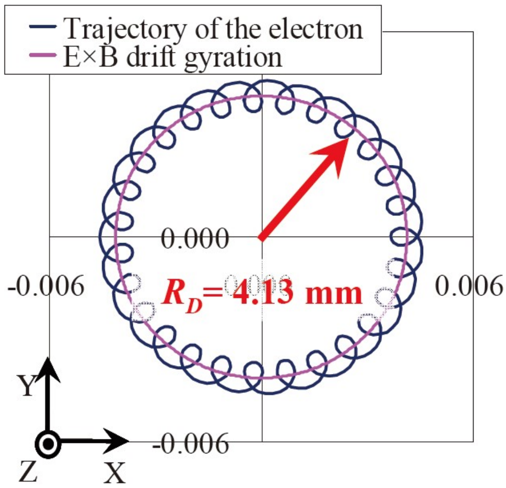

Figure 6.13: Particle trajectory due to rotating electric field. [45]

If the angular frequency is in the range $\omega_{ce} \ll \omega \ll \omega_{ci}$, ions can be considered stationary while electrons are free to move. Thus, Equation (6.52) can be simplify as follow:

$$\begin{cases} v_{x,e} = v_0 \cos(\omega_c t + \delta) + \frac{eE_0}{m\omega_{ce}} \sin(\omega t + \alpha) \\ v_{y,e} = -v_0 \sin(\omega_c t + \delta) - \frac{eE_0}{m\omega_{ce}} \cos(\omega t + \alpha) \end{cases} \tag{6.53}$$

The Larmour gyration is usually smaller than $\vec{E} \times \vec{B}$ drift and then the equations can be further simplified as follow.

$$\begin{cases} v_{x,e} = \frac{eE_0}{m\omega_{ce}} \sin(\omega t + \alpha) \\ v_{y,e} = -\frac{eE_0}{m\omega_{ce}} \cos(\omega t + \alpha) \end{cases} \tag{6.54}$$

The drift velocity called v_D is connected to the drift radius R_D through $v_D = \omega R_D$. Therefore, relations in (6.55) are obtained.

$$v_D \propto \frac{E_0}{b_z} \qquad R_D \propto \frac{E_0}{b_z \omega} \tag{6.55}$$

Every electron moves in a circumference of radius R_D and, since in a helicon thruster the electron density is higher in the center than in the boundary, there is a net movement of electrons that creates an azimuthal current as shown in Figure 6.14.

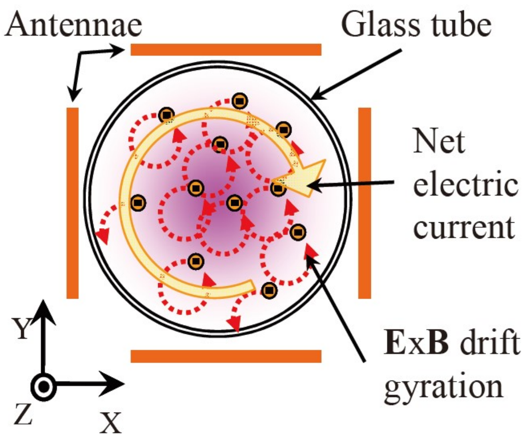

Figure 6.14: The electron trajectories are represented in red. The Larmor gyration is not drawn in this figure. The electron rotation creates an azimuthal current here represented with a yellow arrow. [45]

The azimuthal current in a point A (Figure 6.15) can be calculated integrating the θ-component of every electron velocity which drift passes through A. The mean over 2π is then:

$$j_{\theta D}(x_A, 0) = \frac{e v_D}{2\pi} \int_0^{2\pi} n(x_{Dc}, y_{Dc}) \cos\theta d\theta \tag{6.56}$$

with the density in the drift center $n(x_{Dc}, y_{Dc})$ given by:

$$n(x_{Dc}, y_{Dc}) \simeq n(x, y) + \frac{\partial n(x, y)}{\partial r} R_D \cos\theta \tag{6.57}$$

where the density is $n(r) = n_0(1 - \beta r^2 / r_0^2)$ with β the reduction rate of plasma density.

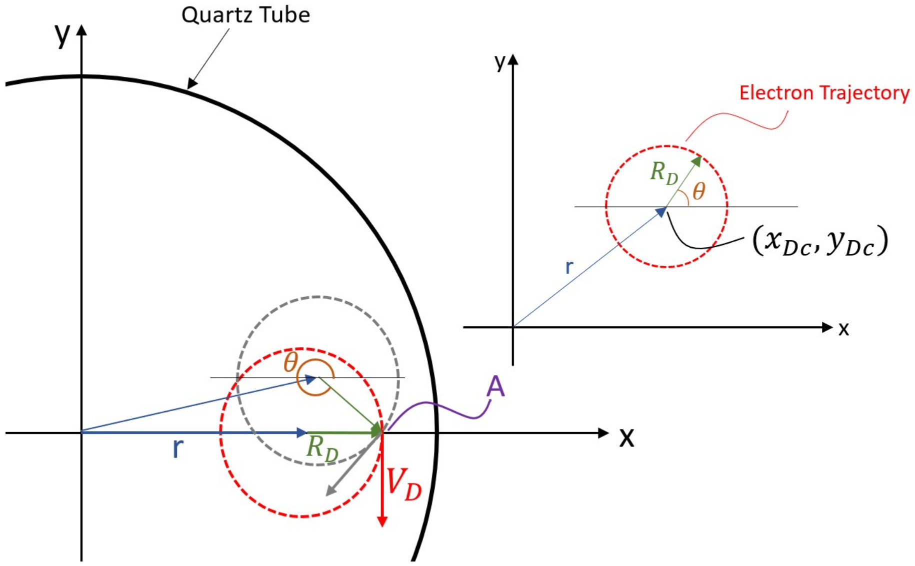

Figure 6.15: Geometrical description of electrons trajectories in a REF.

Substituting this formula into Equation (6.56), the azimuthal drift current is obtained:

$$j_{\theta D}(x_A, 0) = -en_0\beta\frac{v_D^2 r}{\omega r_0^2} \tag{6.58}$$

where r_0 is the radius of the quartz tube.

The azimuthal current given by the Larmour motion can be obtained with the same procedure and the result is shown in Equation (6.59).

$$j_{\theta L}(x_A, 0) = -en_0\beta\frac{v_e^2 r}{\omega_{ce} r_0^2} \tag{6.59}$$

The total azimuthal current in $(x_A, 0)$ is now integrated over the cross section obtaining:[46]

$$j_\theta = \int_0^{r_0}(j_{\theta D} + j_{\theta L})2\pi r dr = -\frac{2\pi}{3}en_0\beta r_0\left(\frac{v_D^2}{\omega} + \frac{v_e^2}{\omega_{ce}}\right) \tag{6.60}$$

Since the electron cyclotron frequency is much higher than the REF angular frequency, j_θ can be written as:

$$j_\theta \propto n_0\beta r_0\frac{v_D^2}{\omega} \propto n_0\beta r_0\frac{E_0^2}{b_z^2\omega} \tag{6.61}$$

So, increasing the electric field intensity and decreasing its frequency gives an higher azimuthal current. Differently, an increase of the axial magnetic field decreases this current. The thrust can be found in the same way as done in the RMF section.

Nishida *et Al.*[46] have simulated a collisionless plasma immersed in a rotating electric field and they have verified that this electric field is able to create an azimuthal current. Instead, Shinohara *et Al.*[56] conducted experiments with an helicon source. They have seen that with REF the particles velocity at the thruster center increases.

Chapter 7

Design and Simulations

This chapter is focused on the acceleration stage design process, conduced with software like Matlab, FEMM and SolidWorks. Since the acceleration stage design is dependent from the antenna one, the procedures used to create the birdcage are explained in the following section. The antenna electromagnetic field has been simulated with XFdtd 7.

7.1 Antenna Simulation

The birdcage antenna has been simulated with an electromagnetic simulation software called XFdtd 7 from Remcom[67] in order to verify if the required rotating electromagnetic field is produced inside the device. The software uses the finite-difference time-domain method to solve Maxwell's equations in the time domain.

The birdcage geometry without shield can be seen in Figure 7.1 while its dimensions are shown in Table 7.1.

The first task is to design a birdcage antenna that has a resonance frequency equal to the RF generator frequency, 40.68 MHz, in order to have the antenna reactance equal to zero. The antenna resonance frequencies, as shown in Equation (7.1), depend on L and M which are the inductance of end-rings and legs, respectively. The inductance cannot be chosen directly in the software because it depends on the magnetic field produced by the birdcage and on the antenna geometry. The only way to design correctly the

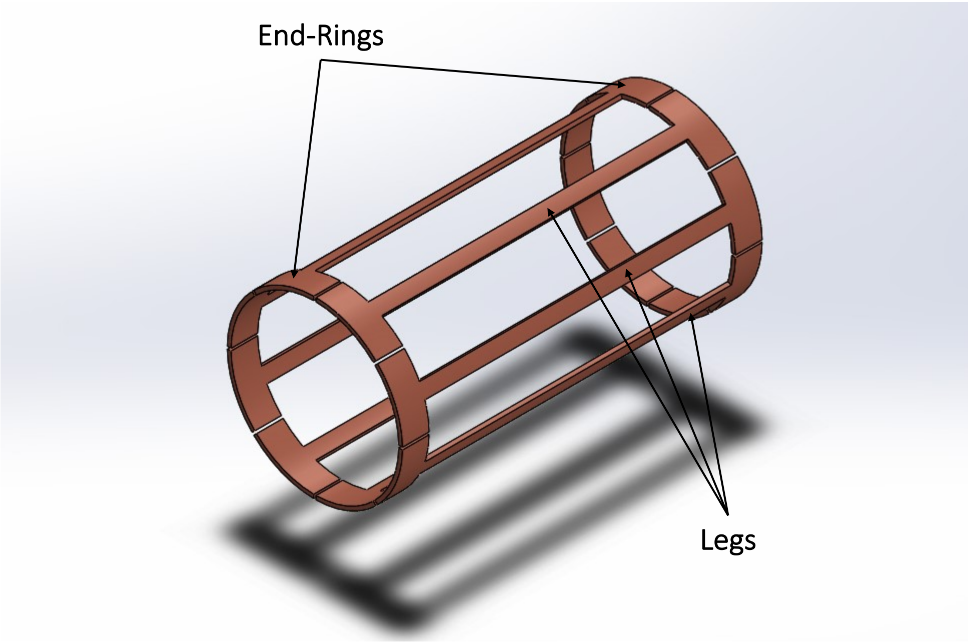

Figure 7.1: CAD image of the birdcage antenna studied. The shield is not shown here. Capacitors are soldered into the end-rigs empty spaces.

Table 7.1: Birdcage and shield dimensions.

Antenna Data			Shield Data		
h_{legs}	80.4	mm	h_{shield}	94.4	mm
$h_{end-rings}$	7	mm	$d_{inner,shield}$	80	mm
$h_{antenna}$	94.4	mm	$d_{outer,shield}$	90	mm
d_{inner}	44	mm			
d_{outer}	46	mm			

antenna is to find through simulations the right combination between capacitance and geometrical parameters in order to have one antenna resonance frequency equal to 40.68 MHz.

$$f_k = \frac{1}{2\pi\sqrt{C\left[L + 2Msin^2\left(\frac{\pi k}{N}\right)\right]}}, \qquad k = 0, 1, ..., N/2 \tag{7.1}$$

The birdcage has to be shielded in order to eliminate the electromagnetic waves presence in the laboratory environment. The shield is an hollow cylinder made with a conductive material which acts like a Faraday cage. Simulations have been conducted with a copper shield positioned around the antenna because, coupling with the antenna electromagnetic field, it alters the magnetic flux, ϕ. In this way, the shielded birdcage inductance, which formula is $L = \phi/I$, changes entailing a resonance frequency shift.[21]

With the geometrical parameters fixed as in Table 7.1, a capacitance of 240 pF has been found through the software in order to have the fourth antenna resonance frequency equal to 40.68 MHz. Three of the four expected resonance frequencies can be seen in Figure 7.2 where the reactance is zero and the impedance real part has a peak. The resonance missing is probably too close to the first one to be seen clearly. This problem could be related with the simulation inability to reach convergence caused by the computational power lack of the laptop used for simulations.

When the neutral gas is ionized by the birdcage, the plasma couples with the antenna changing especially its capacitance and inductance resulting in a resonance frequency shift. As consequence, the fourth antenna resonance is not more on 40.68 MHz, its reactance has a value different from zero and an impedance mismatch is created in the circuit reflecting back a fraction of the input power.[65] To solve this problem, the reactance can be taken again to zero with different techniques. Authors in [21] use a shield composed by two semi-cylindrical plates that can be moved closer or further from the birdcage. This motion, affecting the magnetic flux and thus the antenna inductance, can be used to maintain the reactance to zero as the plasma is produced by the birdcage. The same effect, but without movable parts, can be obtained changing the axial magnetic field strength applied inside the discharge tube to develop the helicon wave. When this happens, the plasma properties change,

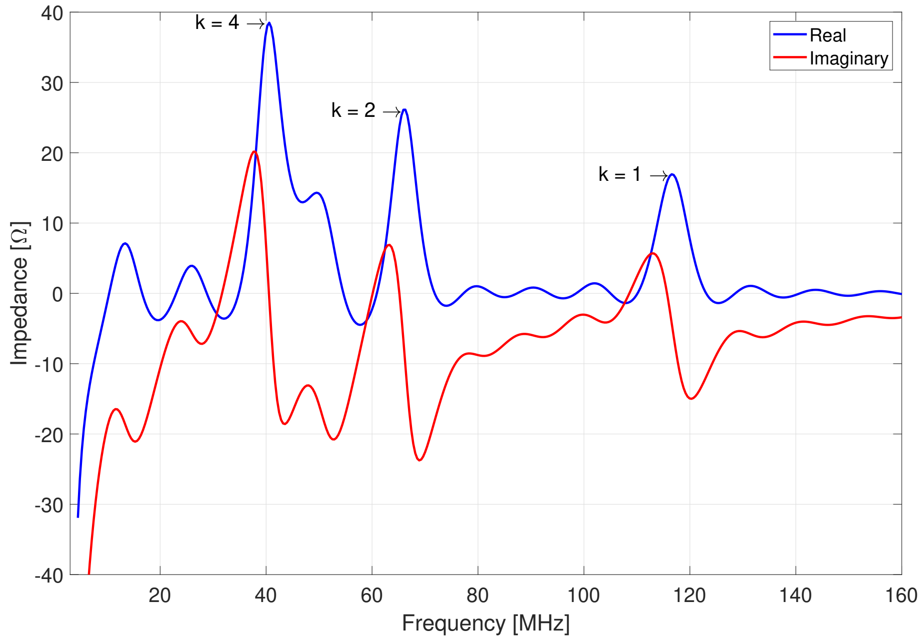

Figure 7.2: Real and imaginary impedance of a shielded birdcage antenna.

its inductance is modified and therefore the antenna resonance frequency shifts. With one of these two techniques, the reactance of the complete system composed by antenna, shield and plasma can be brought to zero as the gas is ionized inside the discharge tube, reducing the reflected power between antenna and matching network.

The last technique has been implemented in the IPT under development because it is the more reliable one since it does not require movable parts. However, this technique has not been used yet by other researchers and for this reason it has to be verified through the experiment.

When the plasma is created inside the discharge chamber, even the real impedance of the antenna changes contributing to the impedance mismatch if it is not exactly $50\,\Omega$.

Through simulations of a birdcage driven in quadrature, it as been verified that the electromagnetic field rotates on the plane perpendicular to the antenna axis. The magnetic and electric field are 90° out of phase as shown at the same time instance in Figure 7.3 and 7.4.

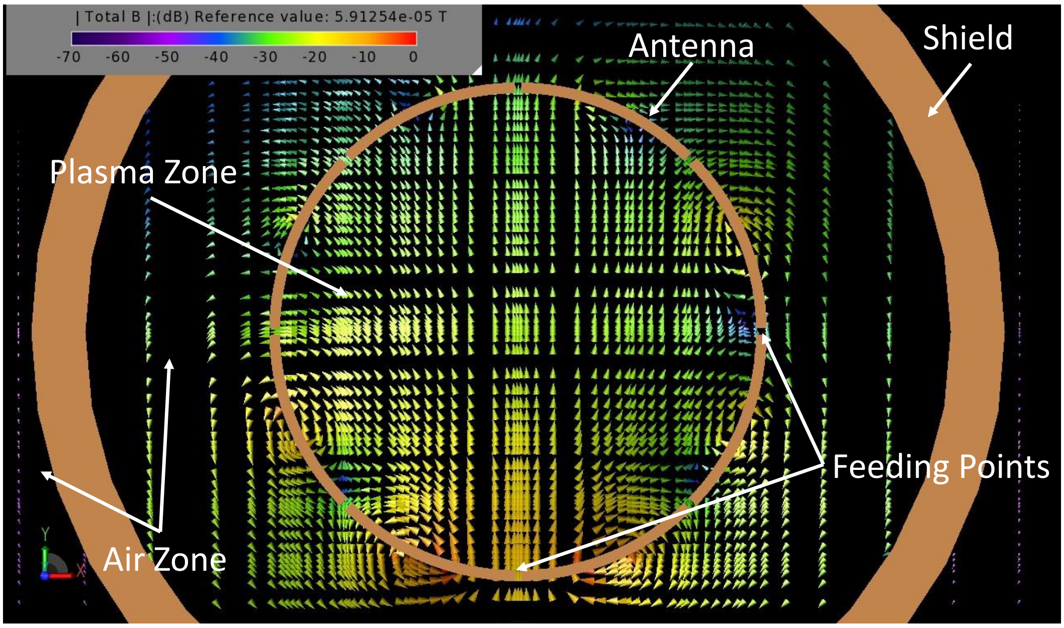

Figure 7.3: Birdcage magnetic field at a fixed time instance t_0.

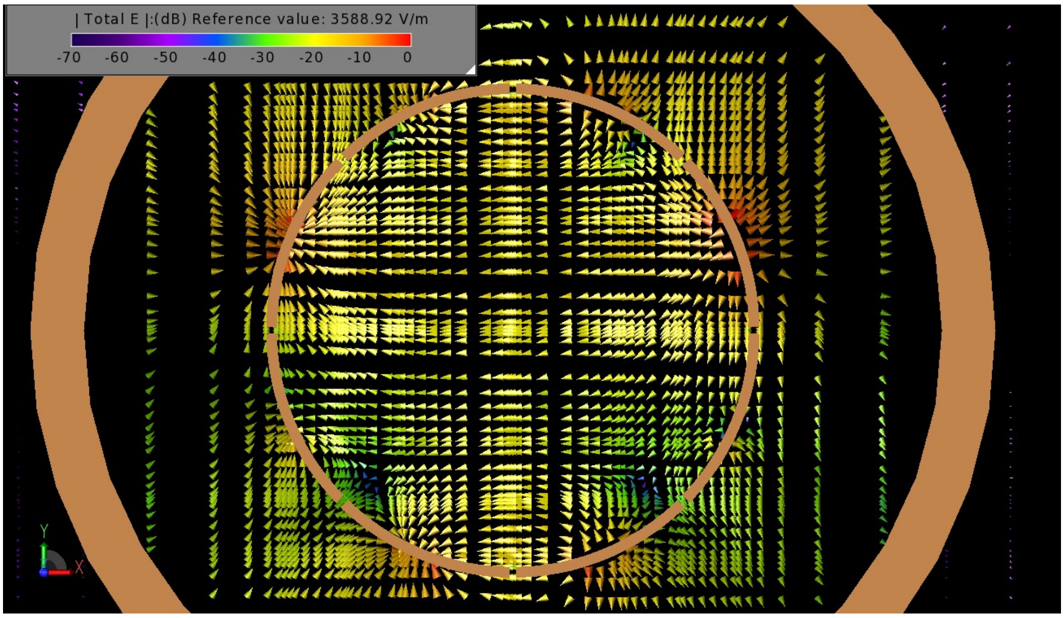

Figure 7.4: Birdcage electric field at a fixed time instance t_0.

7.2 Acceleration Stage Design

As explained in the previous chapters, the thruster uses an axial magnetic field to sustain the helicon wave and to tune the antenna. This axial magnetic field eventually diverges and this part can be used as electromagnetic nozzle to accelerate the plasma. This acceleration stage can be upgraded into a REF or RMF with the addition of conductive plates or antennae when the thrust performance of the only electromagnetic nozzle is not sufficient.

The static magnetic field for helicon wave production, antenna tuning and acceleration stage can be created by a permanent magnet or an electromagnet. Since the field strength has to be changed to maintain the birdcage in resonance, an electromagnet has been chosen because it can create an adjustable magnetic field strength.

A possible acceleration stage design consists on only one electromagnet. This choice creates a light and simple system but the magnetic field strength is constrained by maintaining the antenna in resonance. This design doesn't allow to test different magnetic field topologies and magnitudes which is required in this early stage of thruster development. The final acceleration stage design consists on two electromagnets that can be driven separately. The first electromagnet, positioned near the antenna, is tuned to produce the exact magnetic field to maintain the antenna in resonance while the second electromagnet modifies the magnetic lines of the first one in order to obtain the electromagnetic nozzle topology in the desired position.

The magnetic field strength required to sustain the helicon wave and achieve the desired density of $10^{19}\,\mathrm{m}^{-3}$ can be found using the helicon wave dispersion relation.[7] The result gives a minimum magnetic field value of $420\,\mathrm{mT}$. Instead, a value of $180\,\mathrm{mT}$ is required to reach a plasma density of at least $10^{18}\,\mathrm{m}^{-3}$.

7.2.1 Electromagnet Design

An electromagnet (EM) is composed by a magnet wire wound into a coil. The current flowing in it produces a magnetic field inside the device. The electromagnet is composed by an aluminum structure around which the magnet wire is wound. This structure has a circular aperture slightly larger than the thruster brass support in order to be slided over the IPT structure which simplified design is shown in Figure 7.5.

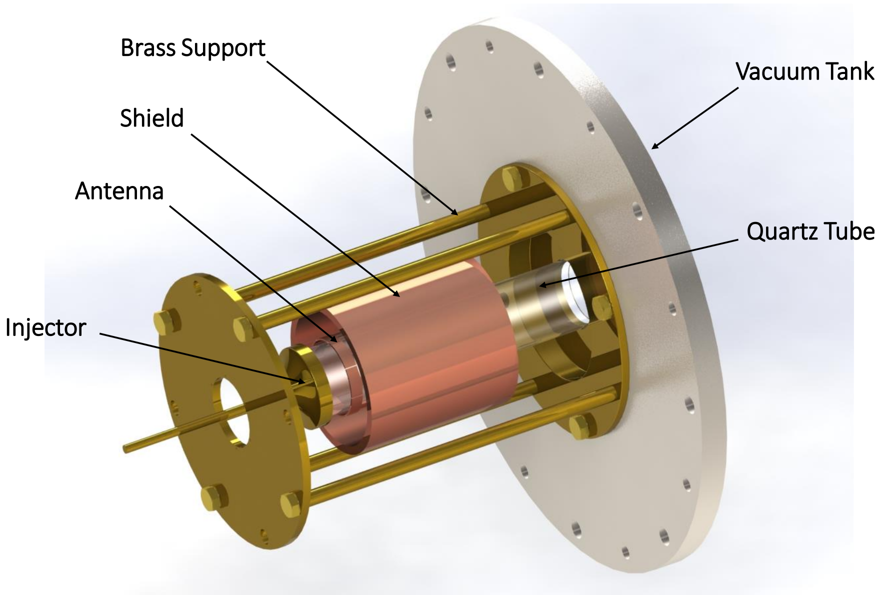

Figure 7.5: Preliminary IPT design image without electromagnets.

The EM is driven with a dc power supply. At the IRS there are two GENESYS™[24] dc generators that can supply 760 W, with a voltage and current up to 40 V and 19 A, respectively. The maximum current that the generator can supply is the first design constrain. With 19 A the EM must produce enough magnetic field to meet the helicon wave magnetic field requirement explained in the section before.

A copper magnet wire (POLIFLEX 200 from IRCE[29]) with 2 mm diameter without insulation and 2.107 mm with insulation has been chosen because it can sustain the maximum current of the dc generator used. The wire thermal class is H and it can withstand a temperature up to 200 °C. This is the second constrain. During the working period, the electromagnet temperature should remain below 200 °C otherwise the insulation fails and a short circuit is formed.

The wire must have the right resistance to allow the flow of a current minor or equal to the maximum one that the generator can supply. The minimum resistance of the wire is:

$$R_{wire,min} = \frac{V_{max}}{I_{max}} = 2.11\,\Omega \tag{7.2}$$

The wire length can be found from the resistance formula as:

$$l_{wire,min} = \frac{R_{wire,min}A_{wire}}{\rho_{Cu}} = 387\,\mathrm{m} \tag{7.3}$$

where ρ_{Cu} is the copper resistivity and A_{wire} is the cross section of the magnet wire without insulation. The result of Equation (7.3) is the magnet wire length that should be used to create the electromagnet winding.

The first electromagnet coil height is taken as 100 mm in order to have an axial magnetic field mostly constant along the discharge channel that can sustain the helicon wave. The aluminum structure that support the winding has a total height of 116 mm because two flanges of 8 mm thickness have been added to hold the winding into position. The internal radius of the aluminum support is 81 mm, slightly larger than the brass structure of the thruster while the external one is 90 mm in order to have an adequate aluminum thickness to support the winding weight. This last dimension corresponds to the internal winding radius. An exploded view of the electromagnet is shown in Figure 7.6.

With these support dimensions, the first electromagnet turns that can be made with 387 m of magnet wire are 611 and therefore, the final electromagnet external radius is 121 mm. Inputs and outputs of the first electromagnet design are shown in Table 7.2.

On the thruster structure there is no enough space for the second electromagnet and, for this reason, it has to be positioned inside the vacuum chamber. The second electromagnet task is to modify the magnetic field lines produced by the first one in order to ideally achieve a completely axial magnetic field in the discharge chamber and to let it diverge only after the quartz tube end. The electromagnet height should be smaller than the previous one in order to have a more pronounced magnetic field divergence that enhances the electromagnetic nozzle thrust. So, 40 mm has been taken for the second electromagnet height. This EM is driven with a dedicated GENESYS dc generator with the same characteristic of the previous one. In this way, the

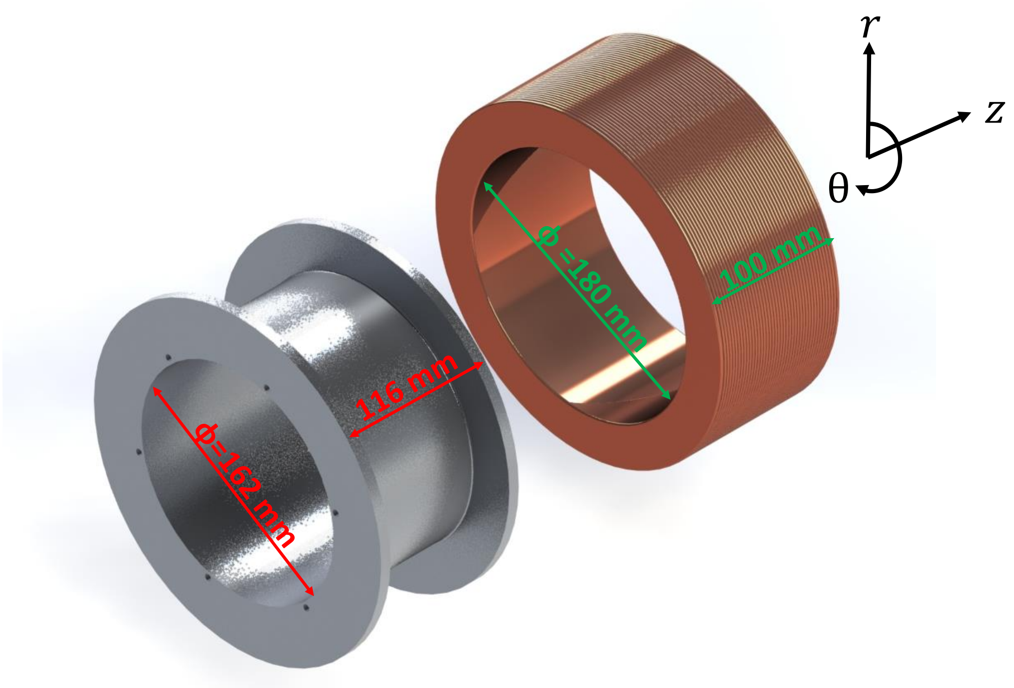

Figure 7.6: Exploded view of the first electromagnet with its relative dimensions.

Table 7.2: I/O values of the first electromagnet design. N_r and N_z are the numbers of complete windings in r and z direction, respectively. Extra wire is the length of the cable not able to complete all 47 turns in the z direction while r_{coil} is the winding radius.

Input Values 1^{st} EM			Output Values 1^{st} EM		
V_{max}	40	V	$R_{wire,min}$	2.11	Ω
I_{max}	19	A	$l_{wire,min}$	387	m
l_{coil}	100	mm	$r_{coil,ext}$	121	mm
d_{wire}	2	mm	N_z	47	-
$d_{insulated,wire}$	2.107	mm	N_r	13	-
ρ_{Cu}	1.71×10^{-8}	$\Omega \cdot$ m	Extra wire	23	m
$r_{coil,int}$	90	mm	Weight	10.9	kg

wire length is the same as before. However, since the electromagnet height has been reduced, the external coil radius increases exceeding the maximum radius of the vacuum chamber walls. Therefore, the sizing of this second electromagnet has the wire resistance as input instead of the supplied voltage. The wire length is reduced, the electromagnet external radius is smaller but the voltage of the dc generator shouldn't exceed 11.9 V to prevent a current higher than 19 A to flow into the circuit. Inputs and outputs for the second EM are shown in Table 7.3.

Table 7.3: I/O values of the second electromagnet design.

Input Values 2^{nd} EM			Output Values 2^{nd} EM		
R	0.63	Ω	V_{max}	11.9	V
I_{max}	19	A	P_{max}	225	W
l_{coil}	40	mm	l_{wire}	115	m
$r_{coil,int}$	72.5	mm	$r_{coil,ext}$	101	mm
$r_{supp,int}$	62.5	mm	N_z	18	-
d_{wire}	2	mm	N_r	12	-
$d_{insulatedwire}$	2.107	mm	Extra wire	10	m
ρ_{Cu}	1.71×10^{-8}	$\Omega \cdot$ m	Weight	3.3	kg

The section view of the IPT preliminary design with two electromagnets is shown in Figure 7.7. The first one has been called external because is positioned out of the vacuum chamber while the second is called internal.

7.2.2 Magnetic Field Topology and Strength

The magnetic field topology and strength produced by the two electromagnets has been simulated with FEMM 4.2[19]. The magnetic field produced by the only external electromagnet driven with the maximum current of 19 A is shown in Figure 7.8 and 7.10. In the so called "middle configuration" the EM is positioned around the antenna while in the "low configuration" the EM is set as close as possible to the quartz tube outlet. The maximum axial magnetic field in the discharge chamber that the external electromagnet can achieve is expected to be 65 mT. The middle configuration gives the maxi-

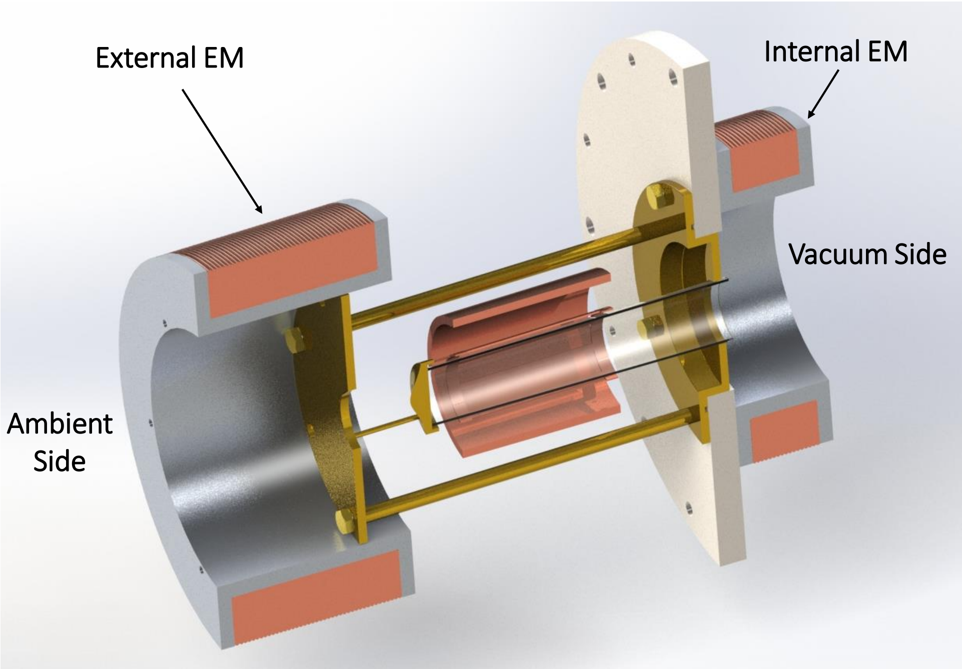

Figure 7.7: Section view of the IPT preliminary design with acceleration stage created by two electromagnets.

mum axial magnetic field in the antenna zone while the magnetic field divergence starts before the exit of the quartz tube that correspond to 180 mm in the following graphs. This divergence, as shown in Figure 7.9, starts in the middle of the electromagnet length and reaches the maximum of 4.7 mT at 115 mm. This radial magnetic field component could lead some of the electrons toward walls with a consequent increase of electron recombination and decrease of the thruster efficiency. Instead, when the electromagnet is in the low configuration, the magnetic field divergence reaches its maximum at 170 mm, as shown in Figure 7.11. In this way, the level of electrons that hit the walls should be lower than the previous case. In these two cases the radial component of the magnetic field near the wall right outside the discharge chamber is expected to be 2.6 mT and 4.5 mT, respectively.

The design with two electromagnets aims first, to increase the range in which the magnetic field is axial inside the discharge tube and second, to better investigate how different magnetic field topologies influence the thruster performance.

In Figure 7.12 and 7.14 the internal EM has been added to the previous simulations. The external EM is driven with 10.5 A while the internal one with 19 A. This proportion has been chosen in order to have a magnetic field of the same magnitude produced by both electromagnets. In the middle configuration, the axial magnetic field has a maximum value of 39 mT while the peak of the radial magnetic field is 3.2 mT after the internal EM as shown in Figure 7.13. The magnetic field magnitude is reduced with respect to the previous cases because the external electromagnet is driven with less current in order to start the divergence only after the discharge chamber.

In Figure 7.14 the external EM is placed in the low position. Since the two electromagnets are now closer, the resultant magnetic field strength increases as shown in Figure 7.15. The radial component reaches a peak of 3.6 mT outside the internal electromagnet and the axial field plateau is about 43 mT for a length of 100 mm, more uniform than the previous case. This last case is the most promising for helicon wave development and plasma confinement thanks to the mostly axial magnetic field in the discharge tube.

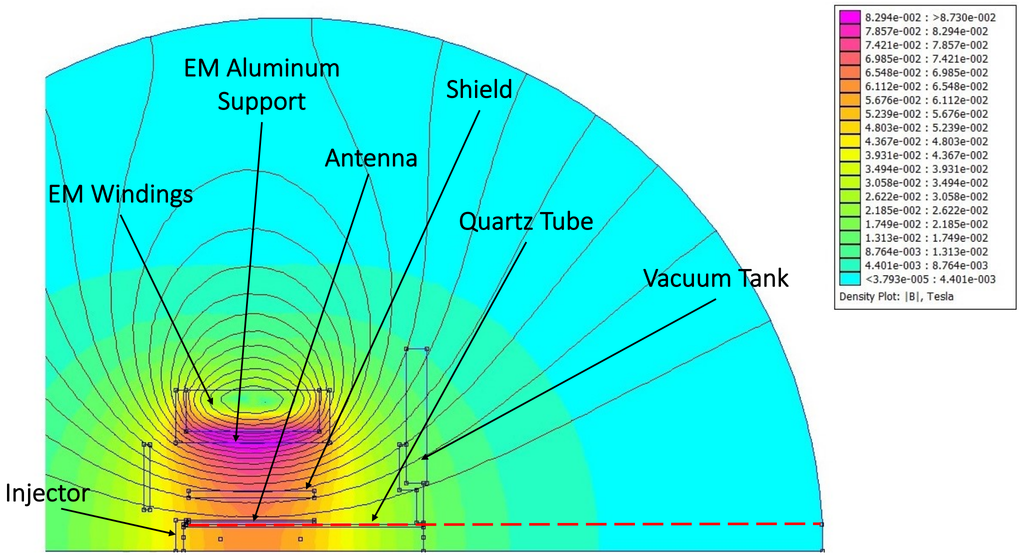

Figure 7.8: Simulation with external electromagnet in the middle position driven with 19 A.

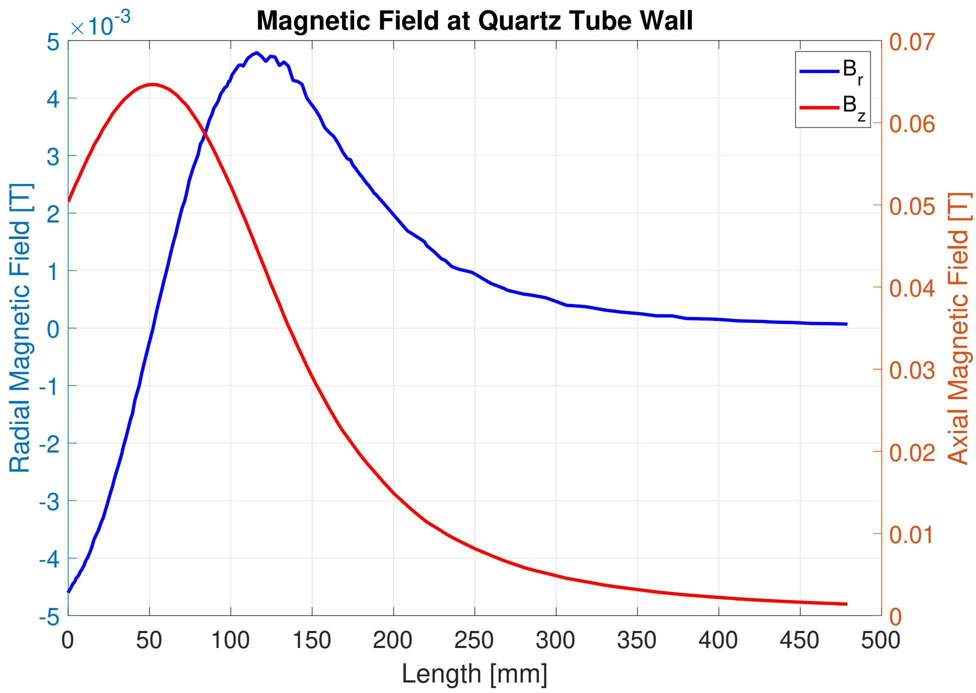

Figure 7.9: Axial and radial magnetic field strength with external EM in the middle position. Data are evaluated over the red dotted line shown in Figure 7.8. The x-axis starts right after the injector end.

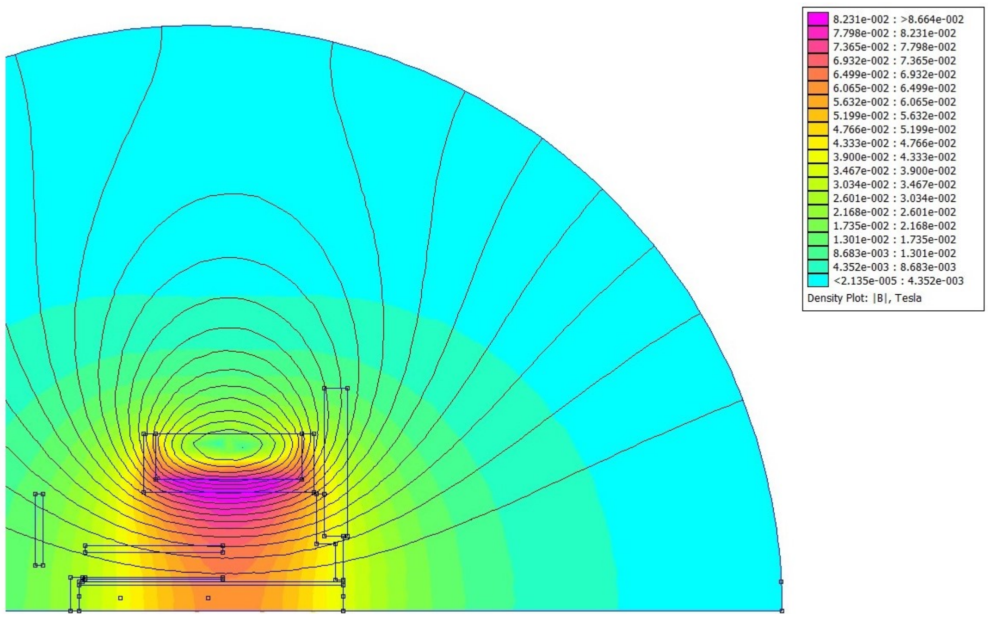

Figure 7.10: Simulation with external electromagnet in the low position.

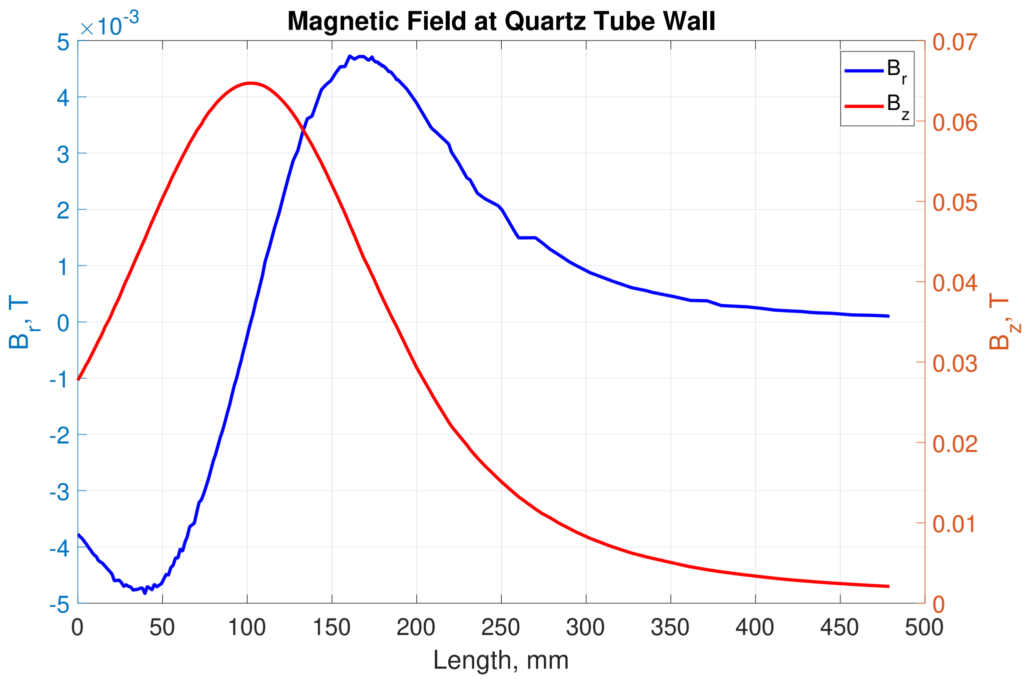

Figure 7.11: Axial and radial magnetic field strength with external EM in the low position. Data are evaluated over the red dotted line shown in Figure 7.8.

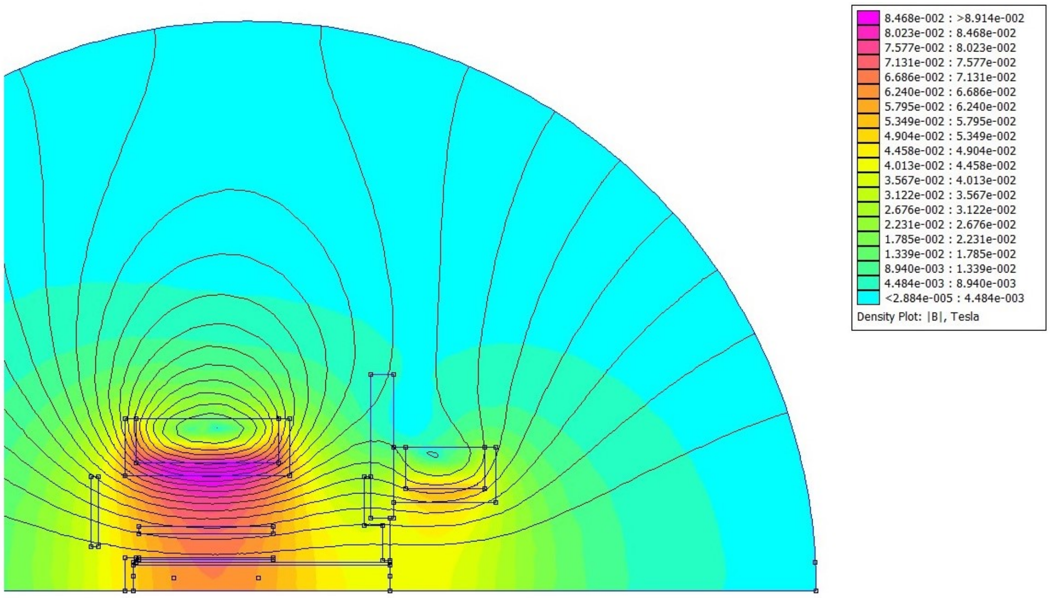

Figure 7.12: Simulation with external EM in the middle position driven with 10.5 A and internal EM with 19 A.

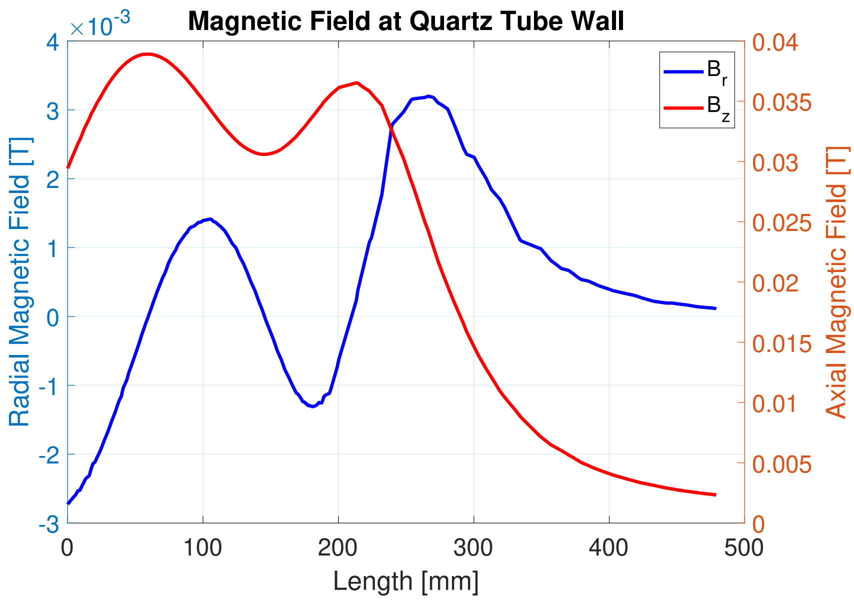

Figure 7.13: Axial and radial magnetic field strength with internal EM and external EM in the middle position. Data are evaluated over the red dotted line shown in Figure 7.8.

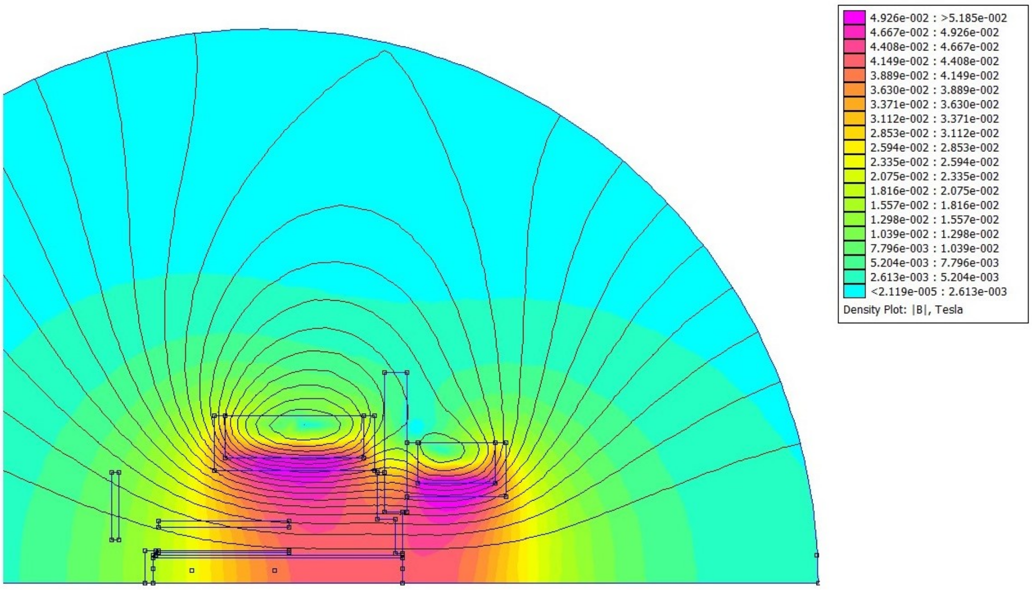

Figure 7.14: Simulation with external EM in the middle position driven with 10.5 A and internal EM with 19 A.

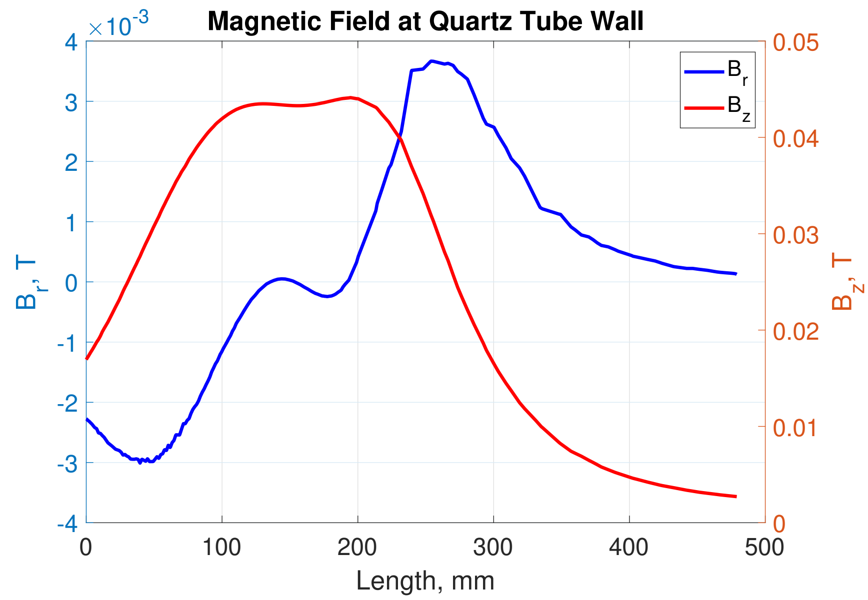

Figure 7.15: Axial and radial magnetic field strength with internal EM and external EM in the low position. Data are evaluated over the red dotted line shown in Figure 7.8.

7.3 Thermal Analysis

A thermal analysis has been conducted to verify if the electromagnets could reach temperatures that exceed the wire insulation limit during their working period. POLIFLEX 200 has a H thermal class insulating layer that can withstand a temperature up to 200 °C.

The software used for this analysis is SolidWorks. The initial temperature has been set to 300 K and the electrical resistance of the interfaces between winding and support is set as $2.5 \times 10^{-4}\,\mathrm{m^2KW^{-1}}$.[15] An heat exchange mechanism has been applied to the exposed surfaces: natural convection for the external EM and radiation for the internal one. Since the internal electromagnet is in a vacuum environment, the natural convection is not present and the radiation is the only mechanism possible.

The real winding cross section has been approximated in order to diminish the project complexity. An example of the real cross section is shown in Figure 7.16b while the approximated one is shown in Figure 7.16a. As result, the real winding cross section is about 21.5 % less than the one simulated. This choice influences the power level to be set into the software. Since the wire resistance, as shown in Equation (7.4), is inversely proportional to its own cross section, the approximated winding cross section has a lower resistance than the real one. So, in order to have a current of 19 A flowing into the magnet wire, the maximum power of the dc generator, 760 W, applied during the experiment has to be reduced to 596 W in simulations where the approximated cross section is used.

$$R_{wire} = \frac{\rho L}{A} \tag{7.4}$$

In order to verify this statement, a test simulation with a smaller electromagnet than the two designed has been conducted and results are shown in Figure 7.17. The test EM with approximated cross section is driven with 596 W while the one with the real cross section is fed with 760 W. The two simulations have similar results with a maximum difference of 4 % meaning that the approximation applied does not introduce errors in the thermal analysis if the power set in the software is reduced of 21.5 %.

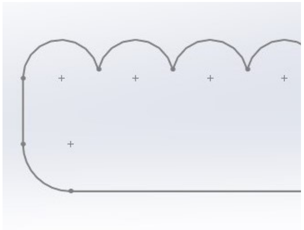

(a) Approximated

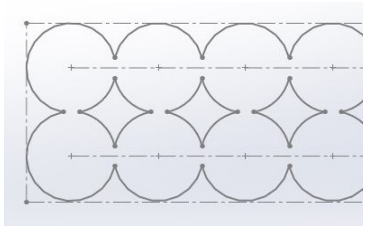

(b) Real

Figure 7.16: Comparison between "approximated" and "real" winding cross section

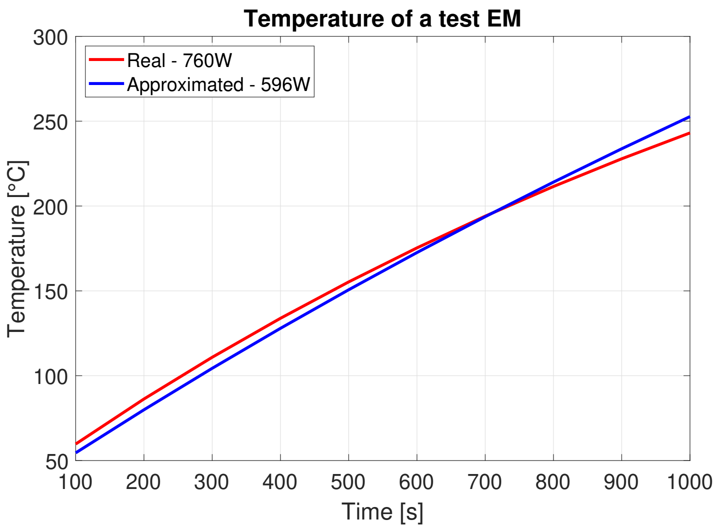

Figure 7.17: Temperature of a test electromagnet with real cross section driven with 760 W and approximated cross section with 596 W.

Two electromagnets thermal transients are simulated shown in Figure 7.18 and 7.19. The temperature is evaluated for different values of convection coefficient[63], h, and emissivity, ε. The total time of the thermal transient is set as 2000 s which is the period required for plasma diagnostic measurements. Even in the worst case scenario, $h = 5\,\mathrm{Wm^{-2}K^{-1}}$ and $\varepsilon = 0.1$, the two electromagnets temperature is below the magnet wire insulation maximum one. The thermal distribution at 2000 s in the two electromagnets is shown in Figure 7.20 and 7.21 where a mostly uniform temperature distribution can be observed. While in the internal electromagnet a radial temperature gradient is visible in the winding, in the external EM this is not present. This is due to the higher input power of the external electromagnet that reduces the temperature gradient between winding and aluminum support.

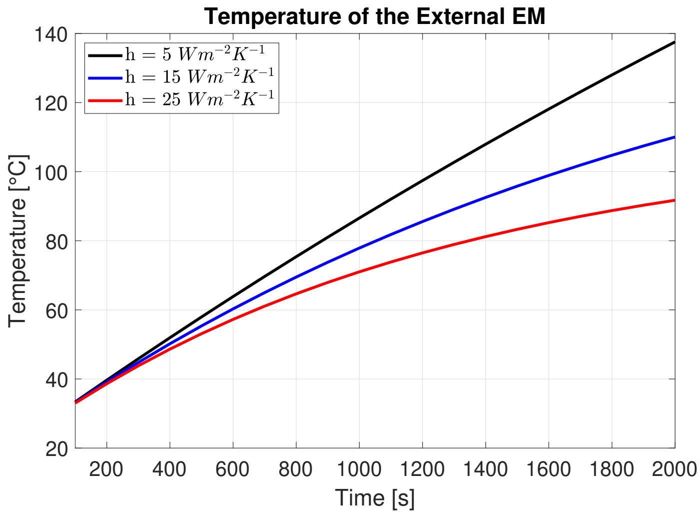

Figure 7.18: Thermal transient of the external electromagnet simulated for different values of natural convection. The EM is driven with $P = 760\,\mathrm{W}$ (596 W in the software).

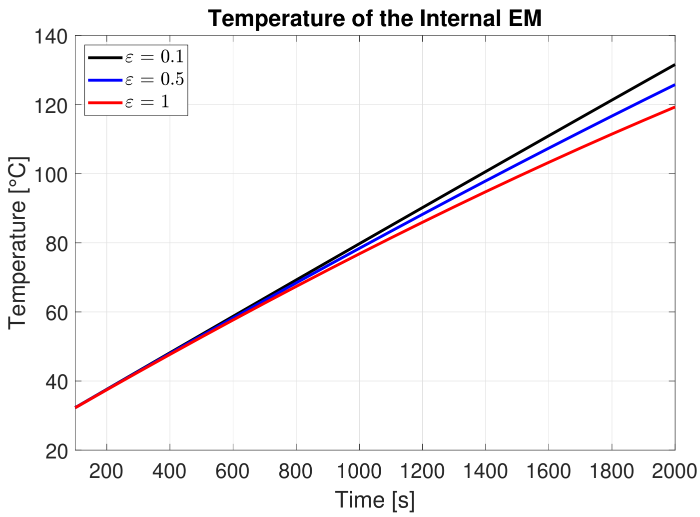

Figure 7.19: Thermal transient of the internal electromagnet simulated for different values of emissivity. The EM is driven with $P = 225\,\mathrm{W}$ (177 W in the software).

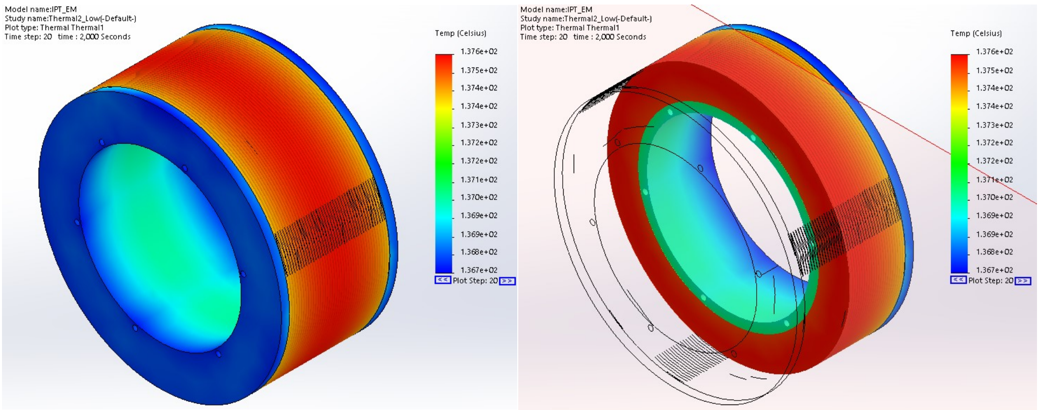

(a) (b)

Figure 7.20: Temperature distribution at 2000 s for the external electromagnet with $h = 5\,\mathrm{Wm^{-2}K^{-1}}$ and $P = 760\,\mathrm{W}$ ($P_{simulation} = 596\,\mathrm{W}$ in the software). a) is the exterior view while b) is the section view. The temperature range in the figure is 136.7–137.6 °C.

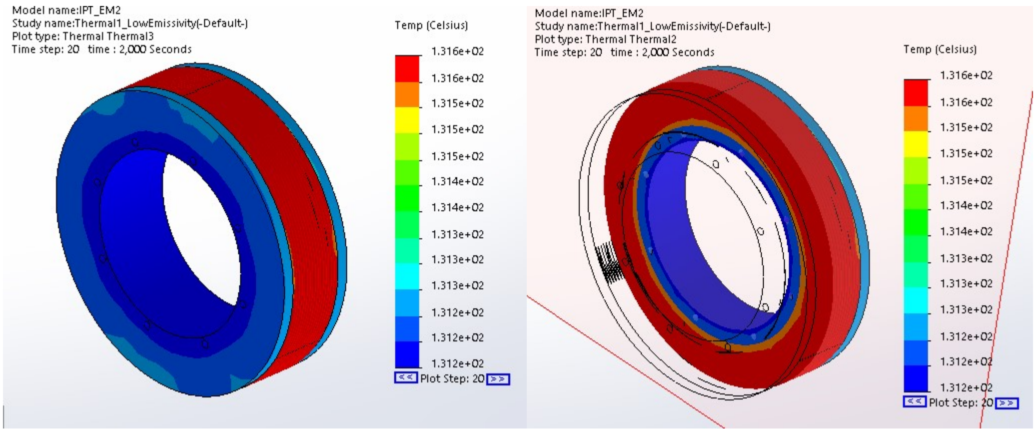

(a) (b)

Figure 7.21: Temperature distribution at 2000 s for the internal electromagnet with $\varepsilon = 0.1$ and $P = 225\,\mathrm{W}$ ($P_{simulation} = 177\,\mathrm{W}$ in the software). a) is the exterior view while b) is the internal view. The temperature range in the figure is 131.2–131.6 °C.

7.4 Acceleration Stage Improvement

The electromagnetic nozzle acceleration stage can be transformed into a RMF with the addition of an antenna able to create a rotating magnetic field in the discharge tube. The antenna can be composed by two pairs of coils positioned around the quartz tube 90° apart. Instead of using this configuration, the same magnetic field rotation can be achieved with a birdcage antenna when fed at two ports in quadrature.

The birdcage rotating magnetic field should create an azimuthal electric field proportional to $cos^2(2\pi ft)$ in the hypothesis that $\omega_{ce} \ll \omega \ll \omega_{ci}$ as previously explained in Section 6.3. This azimuthal electric field oscillates around the value of $E_{\theta,0,Hall} = B_\omega^2 r\omega/2n_e e\eta$ with frequency $2f$. This value can be estimated with the following process.

Taken $f = 40.68\,\text{MHz}$ and a static magnetic field value of $B = 0.01\,\text{T}$ that can be easily supplied by the electromagnets designed, the angular frequencies are:

$$\omega = 2\pi f = 2.556 \times 10^8\,\text{rads}^{-1} \tag{7.5}$$

$$\omega_{ce} = \frac{qB}{m_e} = 1.763 \times 10^9\,\text{rads}^{-1} \tag{7.6}$$

$$\omega_{ci} = \frac{qB}{m_i} = 9.603 \times 10^5\,\text{rads}^{-1} \tag{7.7}$$

If the electron temperature is $T_e = 3\,\text{eV}$, which is a typical value for the plasma considered, the Debye length is:

$$\lambda_D = \left(\frac{\varepsilon_0 k_B T_e[K]}{n_0 e^2}\right)^{0.5} = 1.2621 \times 10^{-5}\,\text{m} \tag{7.8}$$

Therefore, the plasma parameter is:

$$\Lambda = 12\pi n_0 \lambda_D^3 = 7.5793 \times 10^4\,\text{m}^3 \tag{7.9}$$

The resistivity can be estimated with:

$$\eta = 5.2 \times 10^{-5} \frac{\ln \Lambda}{T_e^{3/2}[\text{eV}]} = 1.1244 \times 10^{-4}\,\Omega \cdot \text{m} \tag{7.10}$$

The rotating magnetic field magnitude can be estimated as $B_\omega = 1 \times 10^{-5}\,\mathrm{T}$ from Figure 7.3. With a plasma density expected about $10^{18}\,\mathrm{m^{-3}}$, the magnitude of $E_{\theta,0,Hall}$ created by the rotating magnetic field at $r = 0.1\,\mathrm{m}$ is:

$$E_{\theta,0,Hall} = \frac{B_\omega^2 r\omega}{2n_e e\eta} = 63.6868\,\mathrm{Vm^{-1}} \tag{7.11}$$

The azimuthal current can be found with the θ-component of the generalized Ohm's law as shown in Equation (7.12).

$$E_\theta - \underbrace{\frac{1}{n_0 e} j_z B_r}_{E_{\theta,0,Hall}} = \eta j_\theta \tag{7.12}$$

The first term on the LHS can only be estimated through direct calculation during an experiment because it depends of the plasma particles movement. A representation of Equation (7.12) main components is shown in Figure 7.22.

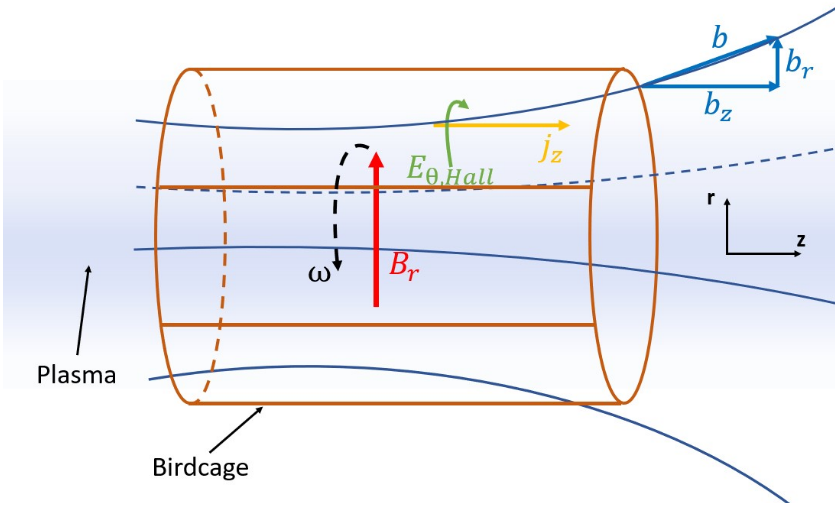

Figure 7.22: Ohm's law main components produced by an high-pass birdcage used as RMF acceleration stage. Quartz tube, capacitors and plasma generation system are not represented here.

The birdcage used as RMF antenna must be positioned after the birdcage for gas ionization and in a zone where the magnetic field divergence is maximum in order to start converting the azimuthal particles motion produced into net axial momentum in the electromagnetic nozzle.

Therefore, the birdcage can be placed inside the vacuum chamber in the center of the internal electromagnet. In the current design there is no enough quartz tube to protect the second birdcage from charged particles. For this reason, the quartz tube has been lengthened from 180 mm to 240 mm and lowered into the discharge chamber. The result is shown in Figure 7.23. The antenna is covered with an additional shield made from ceramic to prevent electrical discharge that can be activated easily in the vacuum environment.

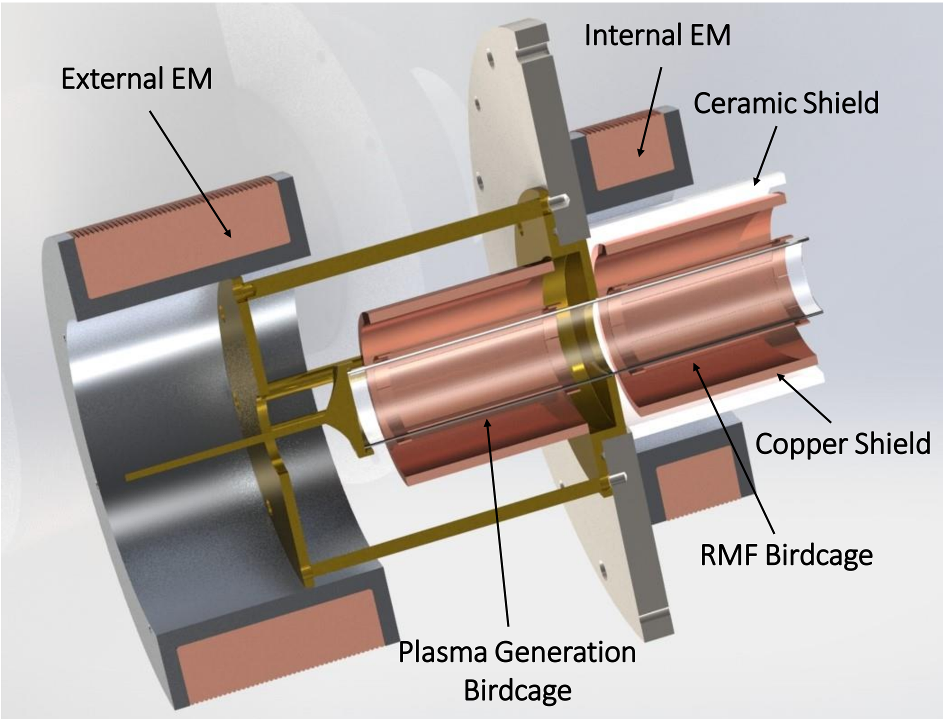

Figure 7.23: Section view of the IPT with RMF acceleration stage.

This new configuration has been simulated with FEMM and the results are shown in Figure 7.24 and 7.25. The maximum magnetic field in the plasma generation antenna is 43 mT while the radial magnetic field peak is 3.7 mT right over the RMF antenna.

A second configuration can be achieved without lowering the 240 mm quartz tube into the vacuum chamber. In this way, the antenna can be positioned right after the one for plasma generation therefore in the laboratory side. This configuration is shown in Figure 7.26. The internal electromagnet has been removed in order to move the electromagnetic nozzle start over the RMF stage. This allow the azimuthal particles motion to be converted into thrust as soon as it is produced by the RMF. The magnetic field simulation of this case is shown in Figure 7.27 and 7.28. The axial magnetic field constance is not achieved since only one electromagnet is used and this can be worse first, for helicon wave development which could lead to a lower plasma density and second, for the plasma confinement.

A constant axial magnetic field is achieved with the addition of a second external electromagnet that is identical to the first one. The FEMM simulation results are shown in Figure 7.29 and 7.30. The addition of this second electromagnet increased the axial magnetic field magnitude to 93 mT and created a plateau of about 100 mm. With respect to the previous configuration, the presence of an axial magnetic field zone should improve the helicon waves development and plasma confinement better guiding particles outside the thruster. In this case, the radial magnetic field reach 6 mT 40 mm before the quartz tube exit.

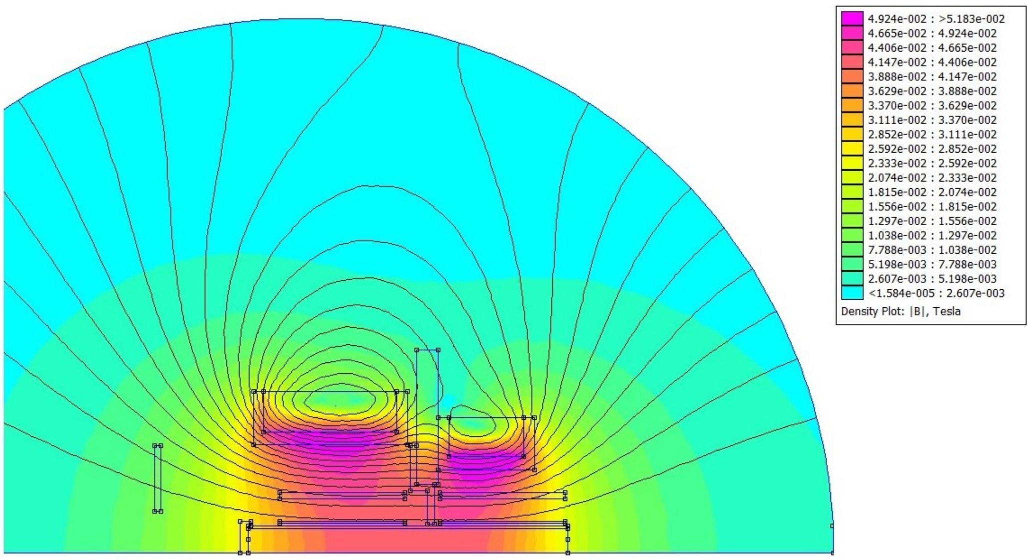

Figure 7.24: FEMM simulation with a RMF acceleration stage inside the vacuum chamber. The internal electromagnet is driven with 19 A while external one is driven with 10.5 A.

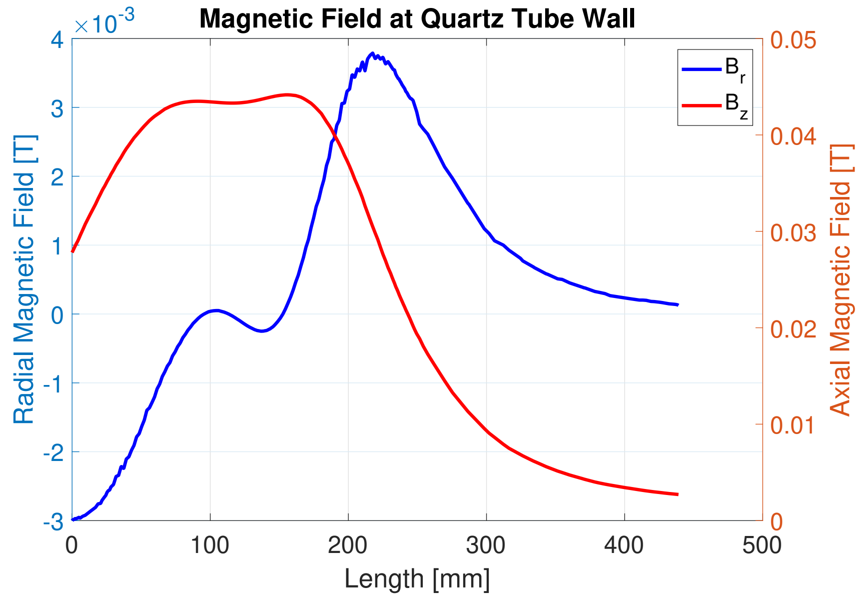

Figure 7.25: Axial and radial magnetic field strength. Data are evaluated over the red dotted line shown in Figure 7.8.

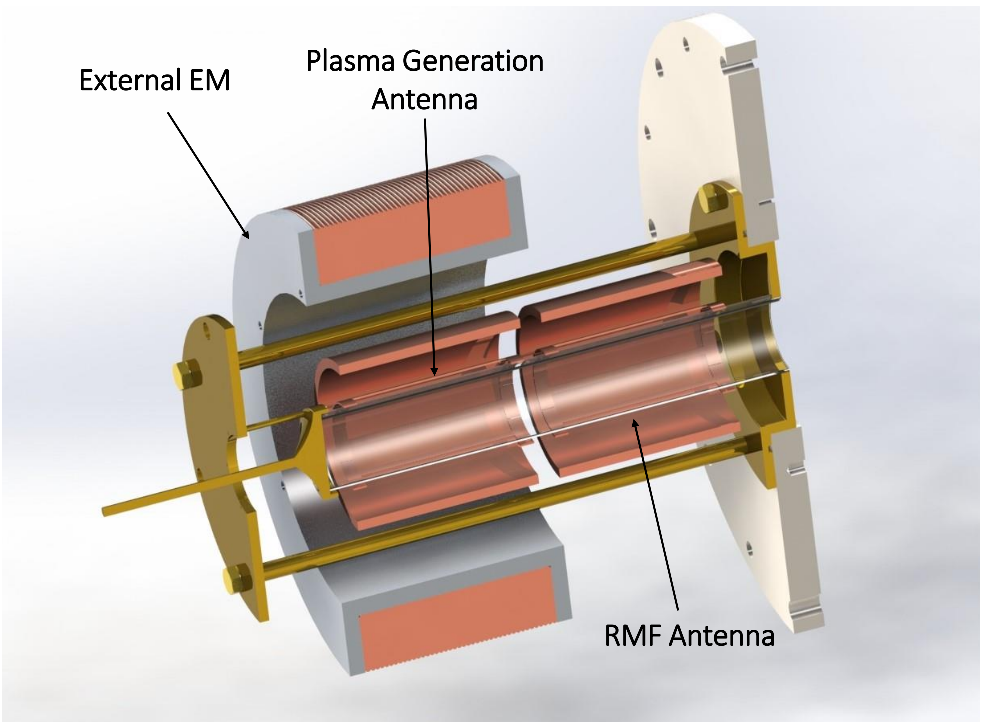

Figure 7.26: Section view of the IPT with external RMF and only one electromagnet.

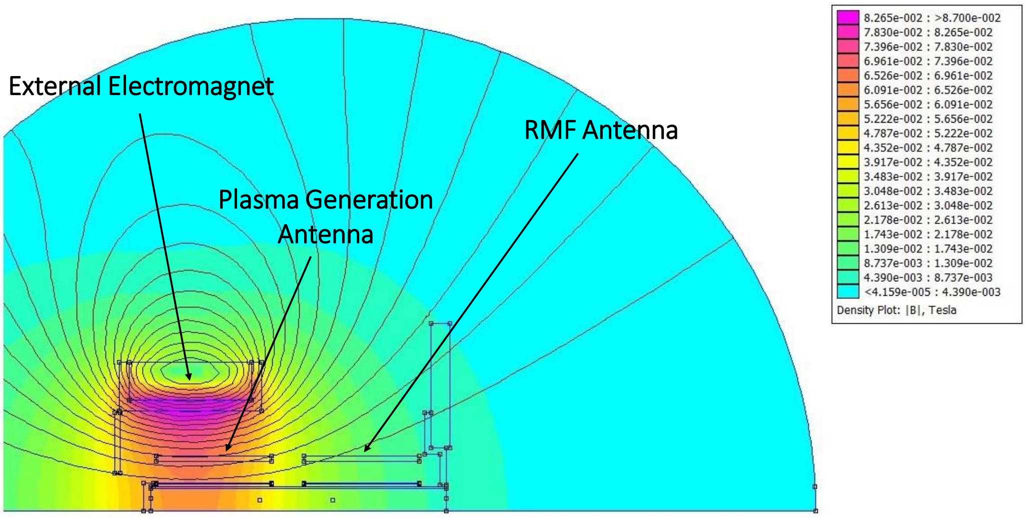

Figure 7.27: Simulation with an external RMF and EM driven with 19 A.

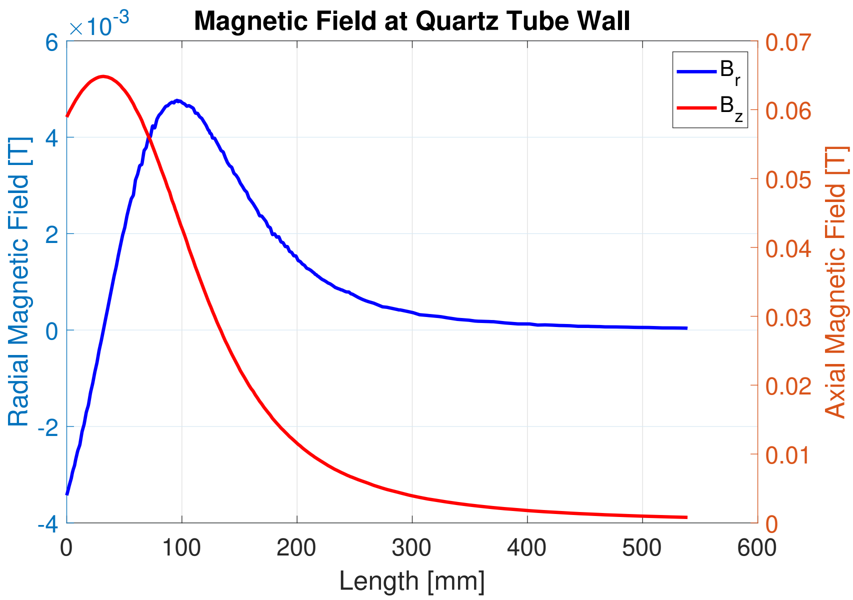

Figure 7.28: Axial and radial magnetic field strength with an external RMF and EM driven with 19 A. Data are evaluated over the red dotted line shown in Figure 7.8.

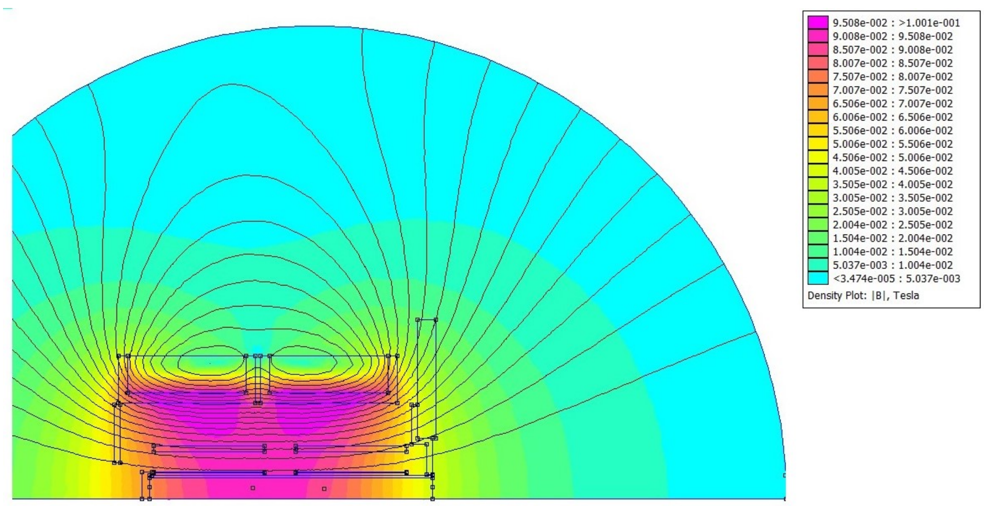

Figure 7.29: Simulation with the external RMF and two external electromagnets driven with 19 A.

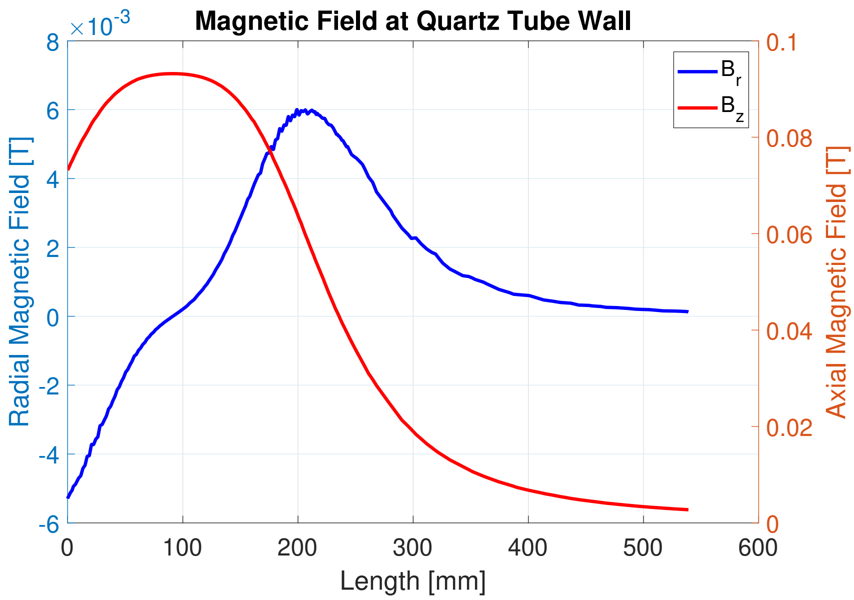

Figure 7.30: Axial and radial magnetic field strength with the external RMF and two external electromagnets driven with 19 A each. Data are evaluated over the red dotted line shown in Figure 7.8.

7.5 Acceleration Stage Conclusions

An electromagnetic nozzle has been designed with two electromagnets driven separately. Four of the most significant magnetic field topologies have been analyzed in this chapter.

The configuration composed by an internal EM and an external one in low position has been chosen as the most promising because it creates a mostly axial magnetic field after the birdcage which should be optimal for helicon wave development and plasma confinement.

A second birdcage antenna has been added over the EN to create a RMF acceleration stage. Three configurations have been studied in this case: one with the RMF inside the vacuum chamber and two with RMF outside it. The option with RMF inside the vacuum chamber is the best configuration when the thrust produced by the only electromagnetic nozzle is not enough. Instead, the configuration with RMF outside should be used in case that plasma density does not reach the desired level since the magnetic field produced is nearly double than the previous case. However, this configuration can introduce interferences between the two birdcage antennae which should be adequately shielded.

Chapter 8

Conclusion and Outlook

Within the European project DISCOVERER the Institute of Space Systems is developing an inductive plasma thruster to be used in an ABEP system flying in a very low Earth orbit. The system employs an intake to collect the residual atmosphere which is then ionized by an antenna. A new antenna design, called birdcage, has been developed aiming to increase the plasma density. After the neutral gas ionization, the plasma has to be accelerated outside to create the thrust. This can be done with an acceleration stage. The plasma, especially because it is created from the residual atmosphere rich of O_2 and N_2, quickly erodes every metal component that gets in contact with it. For this reason, the acceleration stage technology must be electrode-less to allow an adequate lifetime for an ABEP mission to be economically feasible.

In particular, this thesis is focused on the study of birdcage antenna and electromagnetic acceleration stage.

The birdcage antenna is composed by copper legs equally spaced and connected with two end-rings. The antenna has capacitors soldered into the end-rings that, with the resistance and the inductance given by the antenna structure, creates a resonant circuit. When the birdcage is driven with one of its resonance frequencies, the reactance becomes zero while the resistance peaks. As result, the antenna is able to reduce the fraction of power reflected back into the circuit.

The RF current, flowing into the birdcage legs with the correct frequency, creates a magnetic field that is linearly or circularly polarized, depending on the way in which the antenna is fed. Especially if the magnetic field is circularly polarized, the birdcage is expected to enhance the helicon waves development since its magnetic field matches the helicon wave one. On the theoretical point of view, this wave should be very effective on the plasma density enhancement.

An antenna preliminary design has been simulated with XFdtd. As result, the resonance frequencies and the circularly polarized magnetic field have been verified.

A literary review has been conducted on different types of electrode-less acceleration stages. Two of the most promising are: electromagnetic nozzle and rotating magnetic field. The first is composed by divergent magnetic field lines in which, for the magnetic momentum conservation, the azimuthal particles motion is converted into thrust. Instead, the second is an electromagnetic nozzle enhancement method. In particular, over the EN is placed an antenna able to create a rotating magnetic field. This motion has been verified to increase the natural azimuthal motion of electron which is then converted into thrust by the electromagnetic nozzle.

Therefore, an electromagnetic nozzle has been developed trough the design of two electromagnets. One electromagnet is placed outside the vacuum chamber while the other is screwed into the vacuum chamber. Both electromagnets are driven by a dc generator able to supply up to 40 V and 19 A. The magnetic field produced has been tested with FEMM to verify if the minimum axial magnetic field for helicon wave development can be achieved. A thermal analysis has been done with electromagnets to verify that the temperature during their working period does not exceed the maximum one of the wire insulation.

Finally, an acceleration stage improvement has been proposed. The addition of a birdcage as RMF antenna can create an azimuthal particles motion enhancement which improves the electromagnetic nozzle thrust. Different configuration has been proposed, both with the RMF antenna inside and outside the vacuum chamber.

Outlook

The antenna design conducted here is a preliminary one. An accurate design must use a powerful calculator because some changes in the simulation parameters increase the simulation time drastically. In the antenna impedance graph should appear 6 resonance frequencies: $k = 0 - 4$ and the CR mode. The first antenna resonance frequency, f_1, should be the one to match the generator frequency because it is the resonance that creates an homogeneous electromagnetic pattern inside the birdcage volume.[27]

Once assembled, the electromagnets must be tested both to verify the magnetic field and the thermal analysis results. Moreover, the external electromagnet should be tested to verify if it is able to maintain the antenna in resonance as the plasma is created inside the discharge chamber.

The current flowing into the external EM should be adjusted during the experiment to tune the birdcage and, as consequence, the internal EM current should be adequate to maintain the magnetic field lines axial in the quartz tube. All of the magnetic field topologies presented in this master thesis should be tested to verify how the plasma density varies through the use of Langmuir probe or Faraday cup. In the configuration with only the external electromagnet, the plasma confinement and helicon wave development should be less effective leading to a lower plasma density with respect to the thruster configuration with a mostly axial magnetic field in the discharge chamber.

After the experimental calculation of plasma resistivity, the RMF penetration can be estimated. Finally, the RMF birdcage could be added to the thruster in order to calculate the level of thrust improvement. This could be done fixing the thruster to the vacuum chamber and mounting both electromagnets on the same thrust balance in order to have as output only the magnetic thrust of the electromagnetic nozzle.

Bibliography

[1] Richard Ansorge and Martin Graves. *The physics and mathematics of MRI*. IOP Publishing, 2016. ISBN: 978-1-6817-4068-3.

[2] Alexey V. Arefiev and Boris N. Breizman. "Magnetohydrodynamic scenario of plasma detachment in a magnetic nozzle". In: *Physics of Plasmas* 12.4 (2005), p. 043504. DOI: 10.1063/1.1875632.

[3] Constantine A. Balanis. *Modern Antenna Handbook*. p. 1409. ISBN: 978-0-470-03634-1.

[4] S. N. Bathgate, M. M. M. Bilek, and D. R. Mckenzie. "Electrodeless plasma thrusters for spacecraft: a review". In: *Plasma Science and Technology* 19.8 (2017), p. 083001. DOI: 10.1088/2058-6272/aa71fe.

[5] Boris N. Breizman and Alexey V. Arefiev. "Radially localized helicon modes in nonuniform plasma". In: *Physical Review Lett.ers* 84 (17 2000), pp. 3863–3866. DOI: 10.1103/PhysRevLett.84.3863.

[6] David Burton et al. "Observations on the ponderomotive force". In: *SPIE.* (2017). DOI: 10.1117/12.2270542.

[7] Christian Butz. "Plasma characteristics assessment of an inductive plasma thruster". MA thesis. University of Stuttgart, 2019.

[8] Kenneth V. Cartwrigh. "Non-Calculus Derivation of the Maximum Power Transfer Theorem". In: *The Technology Interface* (Spring 2008).

[9] Pascal Chambert and Nicholas Braithwaite. *Physics of radio-frequency plasmas*. Cambridge, 2011. ISBN: 978-0-521-76300-4.

[10] Francis Chen. "Helicon discharges and sources: a review". In: *Plasma Sources Science and Technology* 24 (Feb. 2015). DOI: 10.1088/0963-0252/24/1/014001.

[11] Francis F. Chen. *Introduction to plasma physics and controlled fusion*. Third edition. Springer, 2016. ISBN: ISBN 978-3-319-22308-7.

[12] Francis F. Chen. *Low temperature plasma technology laboratory*. Tech. rep. University of California, Dec. 2012. URL: http://www.seas.ucla.edu/~ffchen/Publs/chen235R.pdf.

[13] Francis F. Chen and Donald Arnush. "Generalized theory of helicon waves. I. Normal modes". In: *Physics of Plasmas* 4.9 (1997), pp. 3411–3421. DOI: 10.1063/1.872483.

[14] Edgar Choueiri. *Ion acceleration by beating electrostatic waves*. Seminar at the Michigan Insitute for Plasma Science and Engineering. Nov. 2010. URL: http://leccap.engin.umich.edu/leccap/viewer/r/zHxzFf.

[15] *Contact Thermal Resistance Value*. URL: http://help.solidworks.com/2019/english/solidworks/cworks/c_thermal_contact_resistance.htm.

[16] Matt Domonkos. "Evaluation of low-current orificed hollow cathodes." PhD thesis. University of Michigan, Jan. 1999.

[17] European cooperation for space standardization (ECSS). *Space engineering - space environment*. ESA Requirements and Standards Division, 2008.

[18] M. Fauri et al. *Lezioni di elettrotecnica - elettrotecnica generale*. Written in Italian. Progetto Leonardo, 2002.

[19] *FEMM webpage*. URL: http://www.femm.info/wiki/HomePage.

[20] A. Fruchtman et al. "A magnetic nozzle calculation of the force on a plasma". In: *Physics of Plasmas* 19.3 (2012), p. 033507. DOI: 10.1063/1.3691650.

[21] I. Furno et al. "Helicon wave-generated plasmas for negative ion beams for fusion". In: *EPJ Web of Conferences* 157 (Jan. 2017), p. 03014. DOI: 10.1051/epjconf/201715703014.

[22] T. Furukawa et al. "Electrodeless plasma acceleration system using rotating magnetic field method". In: *AIP Advances* 7.11 (2017), p. 115204. DOI: 10.1063/1.4998248.

[23] T. Furukawa et al. "Verification of azimuthal current generation employing a rotating magnetic field plasma acceleration method in an open magnetic field configuration". In: *Physics of Plasmas* 26.3 (2019), p. 033505. DOI: 10.1063/1.5064392.

[24] *Genesys 750W/1500W - Programmable DC Power Supplies*. TDK-Lambda Americas Inc. URL: https://us.tdk-lambda.com/hp/pdfs/data%20sheets/93507100.pdf.

[25] R. A. Gerwin et al. *Characterization of plasma flow through magnetic nozzles*. Tech. rep. 1990. DOI: 10.2172/763033.

[26] Ph. Guittienne, E. Chevalier, and Ch. Hollenstein. "Towards an optimal antenna for helicon waves excitation". In: *Journal of Applied Physics* 98.8 (2005), p. 083304. DOI: 10.1063/1.2081107.

[27] Necip Gurler and Yusuf Ziya Ider. "Numerical methods and software tools for simulation, design, and resonant mode analysis of radio frequency birdcage coils used in MRI". In: *Concepts in Magnetic Resonance Part B: Magnetic Resonance Engineering* 45.1 (2015), pp. 13–32. DOI: 10.1002/cmr.b.21279.

[28] E. B. Hooper. "Plasma detachment from a magnetic nozzle". In: *Journal of Propulsion and Power* 9.5 (1993), pp. 757–763. DOI: 10.2514/3.23686.

[29] *IRCE Website*. URL: http://www.irce.it/eng/.

[30] Rémy Jacquier et al. "First B-dot measurements in the RAID device, an alternative negative ion source for DEMO neutral beams". In: *Fusion Engineering and Design* (2019). ISSN: 0920-3796. URL: http://www.sciencedirect.com/science/article/pii/S0920379619301991.

[31] Robert G. Jahn. *Physics of electric propulsion*. McGraw-Hill, 1968.

[32] Robert G. Jahn and Edgar Y. Choueiri. "Electric propulsion". In: *Encyclopedia of Physical Science and Technology*. Elsevier, 2003, pp. 125–141. DOI: 10.1016/b0-12-227410-5/00201-5.

[33] Jian-Ming Jin. "Electromagnetics in Magnetic Resonance Imaging". In: *IEEE Antennas and Propagation Magazine* 40.6 (Dec. 1998).

[34] Ieuan R. Jones. "A review of rotating magnetic field current drive and the operation of the rotamak as a field-reversed configuration (Rotamak-FRC) and a spherical tokamak (Rotamak-ST)". In: *Physics of Plasmas* 6.5 (1999), pp. 1950–1957. DOI: 10.1063/1.873452.

[35] Benjamin Jorns and Edgar Y. Choueiri. "Experiment for plasma energization with beating electrostatic waves". In: *The 31st International Electric Propulsion Conference*. 2009.

[36] Alexander W. Kieckhafer and Mitchell L. R. Walker. "rf power system for thrust measurements of a helicon plasma source". In: *Review of Scientific Instruments 81, 075106* (2010).

[37] David Knight. *The self-resonance and self-capacitance of solenoid coils: applicable theory, models and calculation methods.* May 2016. DOI: 10.13140/RG.2.1.1472.0887.

[38] Michael Lang. "Building a Birdcage Resonator for Magnetic Resonance Imaging Studies of CNS Disorders". MA thesis. University of Winnipeg, 2011.

[39] Mark C. Leifer. "Resonant modes of the birdcage coil". In: *Journal of magnetic resonance* 124 (1997), pp. 51–60.

[40] Mario Merino Martinez. "Analysis of magnetic nozzles for space plasma thrusters". PhD thesis. Universidad Politecnica de Madrid, 2013.

[41] Stephane Mazouffre. "Electric propulsion for satellites and spacecraft: established technologies and novel approaches". In: *Plasma Sources Science and Technology* 25.3 (2016), p. 033002. DOI: 10.1088/0963-0252/25/3/033002.

[42] Mario Merino and Eduardo Ahedo. "Space plasma thrusters: magnetic nozzles for". In: *Encyclopedia of Plasma Technology*. Taylor & Francis, 2016, pp. 1329–1351. URL: https://www.taylorfrancis.com/books/9781351204958.

[43] David G Miljak and Francis F Chen. "Helicon wave excitation with rotating antenna fields". In: *Plasma Sources Science and Technology* 7.1 (Feb. 1998), pp. 61–74. DOI: 10.1088/0963-0252/7/1/009.

[44] Richard D. Milroy. "A numerical study of rotating magnetic fields as a current drive for field reversed configurations". In: *Physics of Plasmas* 6.7 (1999), pp. 2771–2780. DOI: 10.1063/1.873234.

[45] Takahiro Nakamura et al. "Study on helicon plasma lissajous acceleration for electrodeless electric propulsion". In: *J-STAGE* 10.28 (2012). DOI: 10.2322/tastj.10.Tb_17.

[46] Hiroyuki Nishida et al. "Preliminary study on electrodeless magneto-plasma- dynamic thruster using a helicon plasma source". In: *46th AIAA/ASME/SAE/ASEE Joint Propulsion Conference & Exhibit*. AIAA, July 2010.

[47] Shuhei Otsuka et al. "Study on plasma acceleration in completely electrodeless electric propulsion system". In: *Plasma and Fusion Research* 10.0 (2015), pp. 3401026–3401026. DOI: 10.1585/pfr.10.3401026.

[48] Francesco Romano et al. "Advances on the inductive plasma thruster design for an atmosphere-breathing ep system". In: *69th International Astronautical Congress (IAC)*. 2018.

[49] Francesco Romano et al. "System analysis and test-bed for and an atmosphere-breathing". In: *67^{th} International Astronautical Congress (IAC)*. 2017.

[50] Jarbas Sampaio et al. "Resonant Orbital Dynamics in LEO Region: Space Debris in Focus". In: *Mathematical Problems in Engineering* 2014 (Jan. 2014), pp. 1–12. DOI: 10.1155/2014/929810.

[51] S. W. Samwel. "Low earth orbital atomic oxygen erosion effect on spacecraft materials". In: *Space Research Journal* 7.1 (2014), pp. 1–13. DOI: 10.3923/srj.2014.1.13.

[52] Tony Schonherr, Kimiya Komurasaki, and Georg Herdrich. "Analysis of atmosphere-breathing electric propulsion". In: *The 33rd International Electric Propulsion Conference*. George Washington University. Oct. 2013.

[53] Shunjiro Shinohara. "Helicon high-density plasma sources: physics and applications". In: *Advances in Physics: X* (2018). DOI: 10.1080/23746149.2017.1420424.

[54] Shunjiro Shinohara et al. "Development of electrodeless plasma thrusters with high-density helicon plasma sources". In: *IEEE Transactions on Plasma Science* 42.5 (2014), pp. 1245–1254. DOI: 10.1109/tps.2014.2313633.

[55] Shunjiro Shinohara et al. "Development of featured high-density helicon sources and their application to electrodeless plasma thruster". In: *Plasma Physics and Controlled Fusion* 61.1 (2018), p. 014017. DOI: 10.1088/1361-6587/aadd67.

[56] Shunjiro Shinohara et al. "Research and development of electrodeless plasma thrusters using high-density helicon sources: the heat project". In: *IEPC*. Jan. 2011.

[57] R. Spektor and E. Y. Choueiri. "Ion acceleration by beating electrostatic waves: domain of allowed acceleration". In: *Phys. Rev. E* 69 (4 2004), p. 046402. DOI: 10.1103/PhysRevE.69.046402.

[58] *System critical design review gravity field and steady-state ocean circulation explorer*. Tech. rep. Alenia spazio, 2005.

[59] Martin Tajmar. *Advanced space propulsion systems*. Springer, 2003. ISBN: 978-3-211-83862-4.

[60] Kazunori Takahashi. "Helicon-type radiofrequency plasma thrusters and magnetic plasma nozzles". In: *Reviews of Modern Plasma Physics* 3.1 (2019), p. 3. ISSN: 2367-3192. DOI: 10.1007/s41614-019-0024-2.

[61] Kazunori Takahashi et al. "Axial force imparted by a current-free magnetically expanding plasma". In: *Physics of Plasmas* 19.8 (2012), p. 083509. DOI: 10.1063/1.4747701.

[62] Kazunori Takahashi et al. "Electron diamagnetic effect on axial force in an expanding plasma: experiments and theory". In: *Physical Review Letters* 107 (23 2011), p. 235001. DOI: `10.1103/PhysRevLett.107.235001`.

[63] *Thermal Analysis - Solidworks.* 2010. URL: `https://www.solidworks.com/sw/docs/thermal_2010_eng_final.pdf`.

[64] Dai Uchigasaki and Naofumi Ohnishi. "Particle simulation of electrodeless plasma thruster with rotating magnetic field". In: *55th AIAA Aerospace Sciences Meeting.* American Institute of Aeronautics and Astronautics, 2017. DOI: `10.2514/6.2017-1343`.

[65] Niraj Vaghela. *Application note RF (13.56MHz) impedance matching.* URL: `www.if.ufrgs.br/~ckrug/pvd/rf-1.pdf`.

[66] Josep Virgili-Llop et al. "Very low Earth orbit mission concepts for earth observation. benefits and challenges". In: *Reinventing Space Conference, 18-21 November 2014, London, UK.* Nov. 2014.

[67] *XFdtd electromagnetic simulation software from Remcom.* URL: `https://www.remcom.com/xfdtd-3d-em-simulation-software`.